

ADVANCED METHODS OF NONDESTRUCTIVE INSPECTION
OF COMPOSITE STRUCTURES BASED ON
LIMITED ANGLE X-RAY COMPUTED
TOMOGRAPHY

by

EKATERINA BOSTAPH

DISSERTATION

Submitted in partial fulfillment of the requirements

for the degree of Doctor of Philosophy at

The University of Texas at Arlington

Arlington, Texas

Supervising Committee:

Andrew Makeev, Committee Chair and Supervising Professor

Yuri Nikishkov

Seiichi Nomura

Ashfaq Adnan

Albert Montillo

ABSTRACT

Advanced Methods of Nondestructive Inspection of Composite Structures Based on Limited Angle X-Ray Computed Tomography

Ekaterina Bostaph

The University of Texas at Arlington, 2017

Supervising Professor: Dr. Andrew Makeev

This research aimed to study the potential for breaking through object size limitations of current X-ray computed tomography (CT) systems by implementing a limited angle scanning technique. CT stands out among other industrial nondestructive inspection (NDI) methods due to its unique ability to perform 3D volumetric inspection, unmatched micro-focus resolution, and objectivity that allows for automated result interpretation. This work attempts to advance NDI technique to enable microstructural material characterization and structural diagnostics of composite structures, where object sizes often prohibit the application of full 360° CT. Even in situations where the objects can be accommodated within existing micro-CT configuration, achieving sufficient magnification along with full rotation may not be viable.

An effort was therefore made to achieve high-resolution scans from projection datasets with limited angular coverage (less than 180°) by developing effective reconstruction

algorithms in conjunction with robust scan acquisition procedures. Internal features of inspected objects barely distinguishable in a 2D X-ray radiograph can be enhanced by additional projections that are reconstructed to a stack of slices, dramatically improving depth perception, a technique referred to as digital tomosynthesis. Building on the success of state-of-the-art medical tomosynthesis systems, this work sought to explore the feasibility of this technique for composite structures in aerospace applications. The challenge lies in the fact that the slices generated in medical tomosynthesis are too thick for relevant industrial applications.

In order to adapt this concept to composite structures, reconstruction algorithms were expanded by implementation of optimized iterative stochastic methods (capable of reducing noise and refining scan quality) which resulted in better depth perception. The optimal scan acquisition procedure paired with the improved reconstruction algorithm facilitated higher in-plane and depth resolution compared to the clinical application. The developed limited angle tomography technique was demonstrated to be able to detect practically significant manufacturing defects (voids) and structural damage (delaminations) critical to structural integrity of composite parts. Keeping in mind the intended real-world aerospace applications where objects often have virtually unlimited in-plane dimensions, the developed technique of partial scanning could potentially extend the versatility of CT-based inspection and enable game changing NDI systems.

Copyright by
Ekaterina Bostaph
2017

ACKNOWLEDGEMENTS

I would like to express my sincere gratitude to my advisor Professor Andrew Makeev. The expertise I have gained on computed tomography equipment that is typically unavailable to academic researchers, has helped me develop a now much sought-after skillset. I am extremely thankful for him directing me to cutting-edge research that uniquely spoke to my aptitude and personality. None of this would have been possible without Dr. Makeev's foresight and vision.

Special thanks to Dr. Yuri Nikishkov for the enormous amount of technical support he provided. My Ph.D. research would have been inconceivable without the complex computational tools he developed and advanced with his tireless effort. The time and valuable feedback Dr. Makeev and Dr. Nikishkov so generously provided has been instrumental in the successful completion of my work.

I would like to acknowledge all my committee members: Dr. Andrew Makeev, Dr. Yuri Nikishkov, Dr. Seiichi Nomura, Dr. Albert Montillo, and Dr. Ashfaq Adnan for their time and inputs.

I must thank all my former and current colleagues in the Advanced Materials and Structures Lab – Brian Shonkwiler, Dr. Paige Carpentier, Dr. Julia Cline, Sarvenaz Ghaffari, Bastiaan van der Vossen, Dr. Michael Tadros, Dr. Guillaume Seon – for their support and encouragement over the years. Our lunches were the highlight of every day in

the lab. You are like family to me.

I would be remiss if I did not thank Dr. Erian Armanios. The knowledge that I could always count on him and his support provided a sense of security that made UTA feel like home. To dear Debi, Lanie, Flora, Ayesha, Janet, Sally, Kathy, Catherine- thank you all for everything you do to make life easy for us grad students.

Thanks to all my friends: Misha, Danila, Alok, Ghass, Ali Reza, Anirudh, Behzad, Alena, Lena who provided me with the fun to balance out the tough and long hours of work. Especially during holidays and weekends, the knowledge that some of them were alongside working in neighboring labs kept me going.

My dearest friend, Anna, thank you for always being present for me, listening to me, motivating me through the lowest lows, and pushing me to aim higher.

Lastly, I would like to express my endless love and gratitude to my mother for everything she has done for me. I cannot imagine having accomplished this had it not been for her unwavering love and belief in me.

TABLE OF CONTENTS

CHAPTER 1	10
1. Introduction.....	11
1.1 Background and Motivation.....	11
1.2 X-ray CT of Defects in Composites.....	12
1.3 Principles of CT	19
1.4 Limitations of CT.....	23
1.5 Motivation for Partial scanning techniques	29
2. Partial Scanning Techniques	33
2.1 X-Ray CT Reconstruction Methods.....	34
2.1.1 Analytical Reconstruction Methods.....	35
2.1.2 Iterative Reconstruction Methods	36
2.2 Limited Angle Tomography.....	37
2.3 Tomosynthesis	39
3. Reconstruction Methods	47
3.1 Idealized System	47
3.2 Physical Model.....	52
3.3 Solution Methods	54

3.3.1 FDK (Feldkamp, Davis and Kress) Algorithm	54
3.3.2 Penalized Weighted Least Square Method (PWLS)	55
3.3.3 Least Squares Method (LSQR)	57
3.3.4 Tomosynthesis Solution Method	57
3.3.5 Solution Implementation	60
4. Experimental Setup	63
4.1 Scanner Description	63
4.2 Tomosynthesis Procedure	65
4.3 Acquisition technique	77
4.3.1 Influence of Scan Acquisition Parameters	77
4.3.2 Development of Experimental Technique	83
5. Results	87
5.1 Limited Angle Tomography (LAT)	87
5.2 Impact Damage in Laminated Composite	95
5.2.1 Case Study 1: Impact Damage in 12-Ply Carbon/Epoxy Plate	95
5.2.2 Case Study 2: Impact Damage in 24 ply IM7/PMT-F3GHT Carbon/Epoxy Plate	100
5.3 Void Defect in Glass/Epoxy Composite	113
5.4 Comparison of LAT and TS for Void Analysis	123

5.5 Reconstruction of Void Using Iterative Methods130

5.6 Proposed Void Depth Estimation Technique.....133

6. Conclusions..... 139

7. References..... 142

APPENDIX A..... 147

APPENDIX B..... 148

B.1 High-Performance Implementation148

APPENDIX C..... 150

CHAPTER 1

INTRODUCTION

1. Introduction

1.1 Background and Motivation

Composite aircraft structures are much more susceptible to manufacturing irregularities than metal parts.¹⁻³ Furthermore, the presence of small individual flaws at critical locations can significantly affect structural integrity of composites.⁴⁻⁵ A variety of factors may include operator skill, tooling setup, environmental variations and equipment control.⁶⁻⁷ The combination of these factors during part fabrication can significantly affect the part quality, inducing differences in the resin content, bulk factor and fiber alignment.⁴ By the very nature of their structure, the laminated composites possess high strength in the in-plane direction and are weak through the thickness, where they are only bonded by the resin.⁸ During fabrication process, the air or bulk trapped in the composite material oftentimes results in voids. It has been determined that the presence of small individual voids at critical locations can significantly reduce the interlaminar strength and durability of composite structures.^{5, 9} Delamination has been a major failure mode of flight-critical composite structures.¹⁰ The structural integrity issue comes to the forefront, placing a high emphasis on accurate inspection and assessment of the structural health of composite parts both during production and operation stages of their life cycle.

Delamination is one of the most prevalent failure mechanisms for laminated composite structures.^{9, 11} The initiation of delamination, caused by the rise in interlaminar stresses at sites can significantly reduce interlaminar strength and fatigue material properties.⁹ Prediction of the initiation and progression of delamination failure has been a standing

challenge that unequivocally emphasizes the importance of accurate structural diagnostics based on high-fidelity NDI.¹⁰⁻¹¹

X-ray Computed Tomography (CT) can enable accurate measurements of manufacturing defects such as voids and structural damage such as delamination present in composite structure.^{6-7, 11} The entire internal map of the defects captured by the CT can be transferred into a three-dimensional finite element model to further study their effect on the ILT strength and fatigue behavior.^{6, 11-13} This enables accurate prediction of interlaminar strength and fatigue structural behavior.⁶ Due to geometric limitations, most CT scanners fail to accommodate large structures, pertinent to aerospace industry. Therefore in this work, it was attempted to use different techniques including digital tomosynthesis by using cone-beam CT system. By manipulating the scan acquisition techniques and improving the 3D reconstruction with both analytical and iterative algorithms, the attempt was to develop a reliable method of CT inspection for composite structures based on a limited (<180°) range of projection angles. This research aims at a better understanding of the effects of limited angle scanning and their feasibility in implementation to composite structures. The remainder of this chapter will provide a roadmap of the dissertation document with brief descriptions of each chapter provided toward the end.

1.2 X-ray CT of Defects in Composites

Modern industrial X-ray CT systems are capable of high-resolution scans of composite specimens;⁶ however achieving high magnification factors limits their cross-sections in size.⁷ Industrial systems typically use cone-beam configuration that includes X-ray point

source, flat panel detector, and rotational stage for the inspected object. New generation micro-focus X-ray tubes and amorphous silicon flat panel area detectors offer micron-scale resolutions, which cannot be matched by other available NDE methods.¹³ A CT scan typically includes series of 2D X-ray images of the object rotating 360°. A 12 x 16 inch flat panel detector with 0.1 - 0.2 mm-sized acquisition pixel can acquire a number of 10 megapixel radiographs (digital X-ray images) per angular degree. The finer angular increment of acquired projections leads to improved scan quality. Once the scan is complete, CT reconstruction algorithms are used to generate 3D volume of intensity values that correspond to the scanned object density distribution. Given the CT reconstruction, it is possible to manipulate 3D volume in real-time, slice anywhere inside the object, and manipulate the reconstruction histogram to view selected object densities in high contrast. A North Star Imaging X5000 industrial CT system with a 225 kV micro-focus X-ray tube and Varian 4030E series flat panel detector was used to obtain CT scans demonstrated in this work. This CT system could accommodate articles up to 5 feet long.

X-ray CT was shown to accurately measure manufacturing and structural defect locations and sizes in three dimensions.⁶ Prompted by the critical interest in the rotorcraft industry,⁴ a number of validation examples of the CT-based NDE techniques were accomplished for Glass-fiber and Carbon-fiber reinforced Epoxy-matrix prepreg composites. **Figure 1.2.1** demonstrates CT scans of composite details ranging from coupon to component sizes: (A) 30-ply 6-mm thick fiberglass composite laminate; (B) one-inch thick composite tail rotor flex beam structure; (C) a composite rotor blade spar structure.

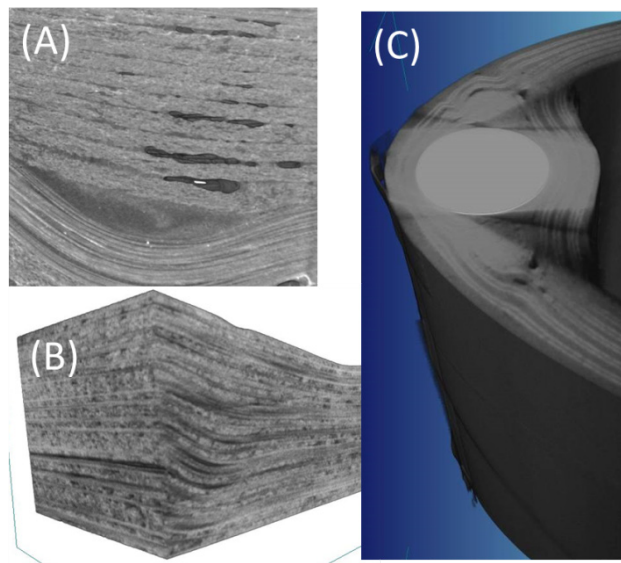


Figure 1.2.1 Examples of defects in aircraft composites detected by X-ray CT.⁶

Figure 1.2.1 shows examples of manufacturing defects such as ply waviness (all views), ply drops (C), resin pockets (A), voids and porosity (all). Defects are easily identifiable using volumetric visualization software. The software allows measuring the defects with precision determined by the scan resolution that typically ranges from 10 to 100 μm . Moreover, good definition of the features and relatively low noise enables development of automatic feature analysis,^{6, 11} avoiding time consuming and error prone human assessment⁷ and transfer of defect information into structural models.

The rest of the section presents the summary of manufacturing and structural defects identified using X-ray CT to provide examples of defects that need to be detected by a successful NDE application for composites. **Figure 1.2.2** demonstrates CT scan volume sections of unidirectional Carbon/Epoxy flat and curved specimens that show voids due to manufacturing imperfections and also a delamination resulting from applied loads (Figure

1.3.2B). Voids can be clearly identified as noodle-like dark areas that are 10-50 μm in cross-section and up to 2 mm in length. Although similar in appearance, voids in Figure 1.2.2A did not lead to significant degradation of the specimen interlaminar shear strength; while a single void in Figure 1.2.2B resulted in more than 50% degradation of the interlaminar tensile strength. Refer to Nikishkov et al¹² for more details on the specimen tests and scan parameters.

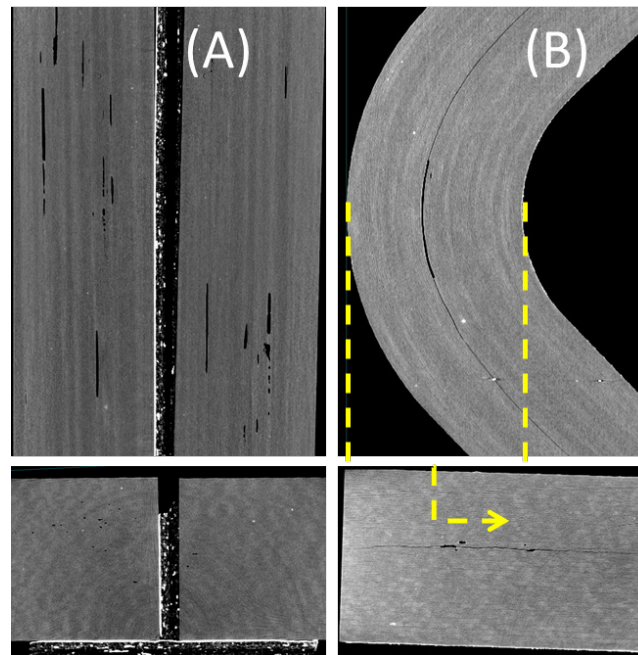


Figure 1.2.2 X-ray CT scans of flat (A) and curved (B) Carbon/Epoxy unidirectional laminates show voids and delaminations.¹²

Accuracy of porosity / voids detection by X-ray CT depends mostly on the resolution of the scan. Typically, voids that are less than $3 \times 3 \times 3$ volume of voxels are not discernable from the noise. However, for long voids or delaminations, the longer dimension can be used for identification of the defect; in this case the cross-section of identifiable defect can

be less than a pixel. Measurements can be affected by other scan parameters, such as sharpness. Nikishkov et al¹⁴ presented a method for accurate measurement of voids based on the sub-pixel contouring for the average of the air/material CT gray values; and discussed robustness and accuracy of the X-ray CT void measurements in comparison to microscopic measurements in the cut sections.

Fiber waviness is another type of manufacturing defects that can lead to significant degradation of composite part performance. Detection of waviness strongly depends on the available contrast in the CT scan, which in turn depends on density difference between fibers and resin (see Nikishkov et al¹⁴ for an example study of X-ray CT density contrasts for different materials). For Glass/Epoxy composites (**Fig. 1.2.3A**) this difference is large enough to typically produce clear definition of waviness that can be automatically transferred to structural models.¹⁵ In Carbon/Epoxy composites, on the other hand, smaller density variation between the phases makes waviness detection more challenging, especially when both in-plane and out-of-plane waviness are present (Fig. 1.2.2B).

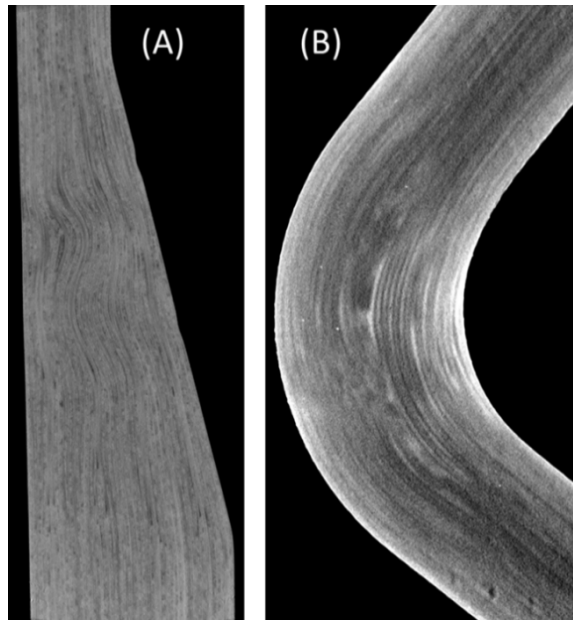


Figure 1.2.3 X-ray CT scans of ply waviness in Glass/Epoxy tapered (A) and Carbon/Epoxy curved (B) composite laminates.¹⁵

Figure 1.2.4 shows defects due seeded voids in a Glass/Epoxy rotor yoke specimen that was used to investigate the effects of voids on the strength and fatigue of composite laminate structure. Due to high contrast between fibers and resin, the Figure clearly shows in-plane and out-of-plane waviness and resin pockets that formed due to introduction of a seeded void. Modeling of the material and geometric structure due to defects has been essential for accurate prognosis of strength and fatigue performance of composite laminate.¹¹

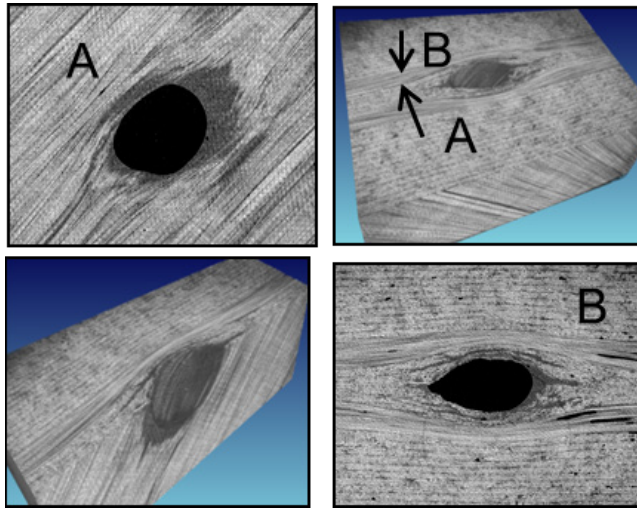


Figure 1.2.4 X-ray CT scans of defects in Glass/Epoxy Rotor Yoke specimen. Letters denote section views.

Structural defects, such as matrix cracks and delaminations, are typically well detectable in X-ray CT scans although the detection relies on the density contrast resulting from an opening between the crack surfaces. **Figure 1.2.5** shows examples of matrix cracks and delaminations for a fatigued Carbon/Epoxy Open-Hole specimen.⁶

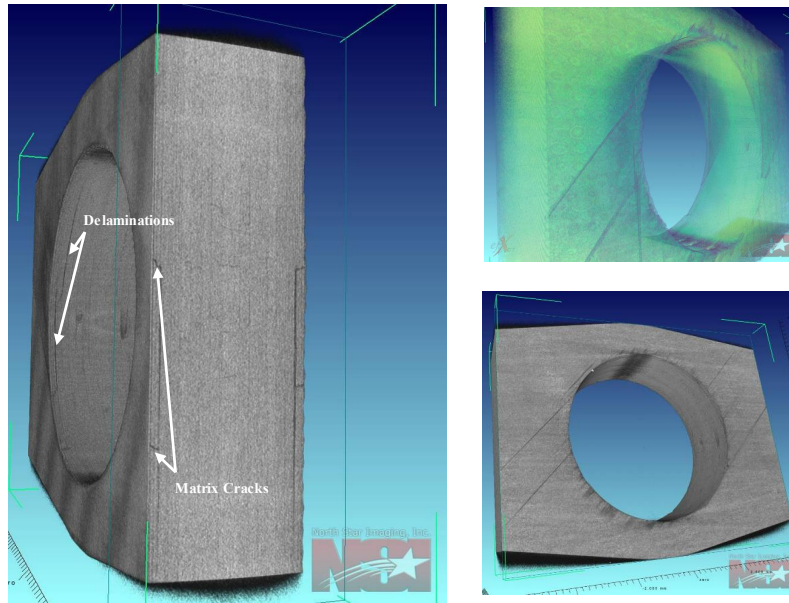


Figure 1.2.5 X-ray CT scans of structural defects in fatigued Carbon/Epoxy Open-Hole specimen.

X-ray detection of defects in composite structures that cannot undergo full rotation in X-ray CT presents a number of challenges. X-ray detectable tracer fibers of higher density are oftentimes placed in composite structures to identify waviness defects in planar radiographs. Planar radiographs are also capable of detecting large voids provided they are sufficiently thick, and matrix cracks provided they are well aligned with the projection plane; but delaminations are typically not detectable due to lack of contrast. Detection of multiple defects, and their sizes and depths proves to be a challenging task when full angular range CT of the specimen is not possible.

1.3 Principles of CT

Most industrial CT systems contain three main components: the X-ray source, the rotation stage and the digital detector.^{6, 13} As opposed to clinical imaging systems, where X-ray

source and detector are connected by a C-shaped arm and rotate around a human subject,⁶ in the industrial CT installations it is usually the object that rotates around its axis, while the source and detector remain stationary during the scan. The scans in this work were obtained using an industrial cabinet CT system, operated in the latter configuration.

The term ‘X-ray tube’ refers to a complex X-ray generating device, and is usually described by the maximum power of the beam it can produce, the beam shape (fan, cone, parallel) and the size of the target focal spot, which essentially determines the resolution of the scan. New generation micro-focus X-ray tubes offer micron-scale resolution.¹³ Most CT systems use flat panel detectors, although linear and curved linear diode array detectors also find their use in some industrial applications. The rotary stage is a precision controlled manipulator that ensures the accurate positioning of the sample during the scan. **Figure 1.3.1** shows the three main CT system components.

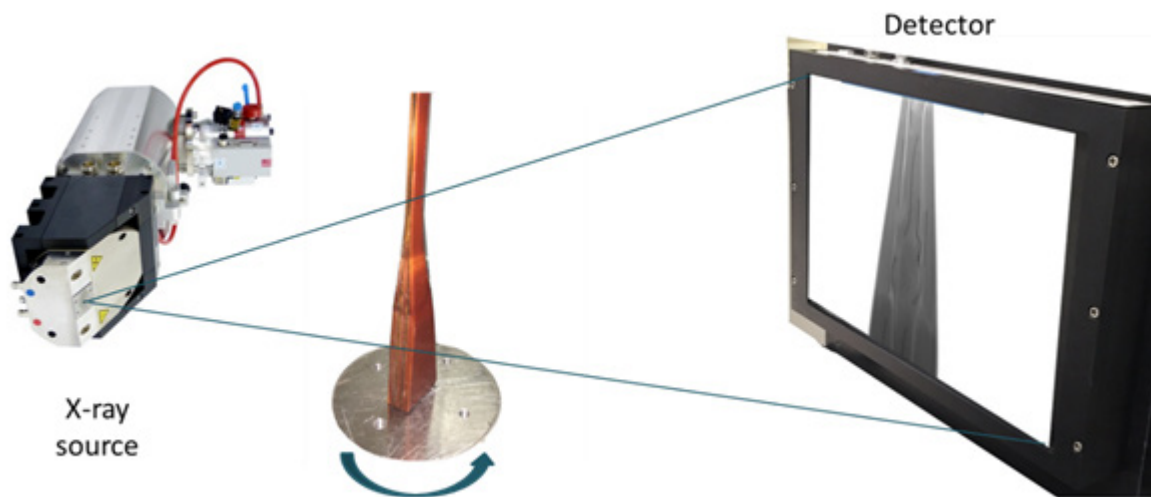


Figure 1.3.1 Three main components of CT system: X-ray source, rotary stage and the detector

The scan acquisition is usually performed using the following procedure. Firstly, the inspected object, secured to the rotary stage. Then as the stage starts undergoing rotation around its axis, a series of 2D X-ray projections are collected as the object gets illuminated by the beam. This continues at every angular step, defined by the user, till it completes a 360° range.¹³ As mentioned before, the X-ray source and detector remain stationary and fixed relative to each other as the object rotates for the duration of the scan. This setup is very common for the industrial CT scanners.

The detector records a superimposed digital projection (radiograph) of the inspected object at a certain angle. On account of this, it is challenging to interpret a single radiograph. A simplistic example is provided in **Figure 1.3.2**, where two objects of the same geometry are placed adjacent to each other. At a particular angular position (Figure 1.3.2a), it is readily apparent that two distinct objects are present. You can measure their width and the gap between them. On the contrary, consider the radiograph in Figure 1.3.2b. The objects were positioned in such a way that they overlap each other in the projection, making it impossible to determine how many of them were scanned. Given the vastly more complex task of examining and interpreting the internal features of real structures, it is conceivable that a 2D radiograph collected at an unfavorable angle, can provide a misleading information about the object.

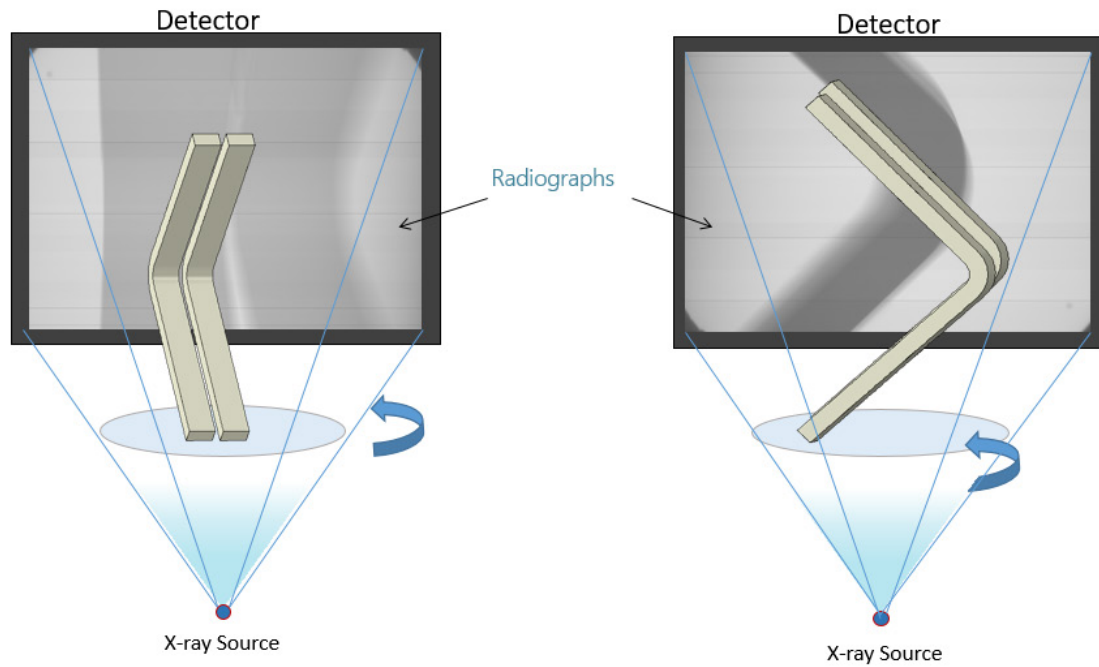


Figure 1.3.2 Projection views of the two objects taken at different angles

In order to get the full information about the object, it is necessary to acquire the radiographs all around the object. The size of indications that need to be detected and their distance away from the axis of rotation determine the number of projections of the scan. It is not unusual to collect six and even ten radiographs per 1° angle, which results in a total of thousands of projections. Once the scan is complete, CT reconstruction algorithms are used to generate 3D volume of intensity values that correspond to the scanned object density distribution. Given the CT reconstruction, it is possible to manipulate 3D volume in real time, slice anywhere inside the object, and manipulate the reconstruction histogram to view selected object densities in high contrast.

1.4 Limitations of CT

To provide a micron level resolution, modern CT scanners need to ensure a highly accurate positioning of all three components. Any deviation from the actual geometric distances will result in artifacts in reconstructed 3D volume. The distance from X-ray source to the detector is the first parameter that needs to be precisely known. This distance should not be confused with the distance from the tube to the detector, which can be measured with a tape. Since the source is encapsulated inside the tube and usually is located at some distance to the output window, its reading should be calibrated individually for every system.

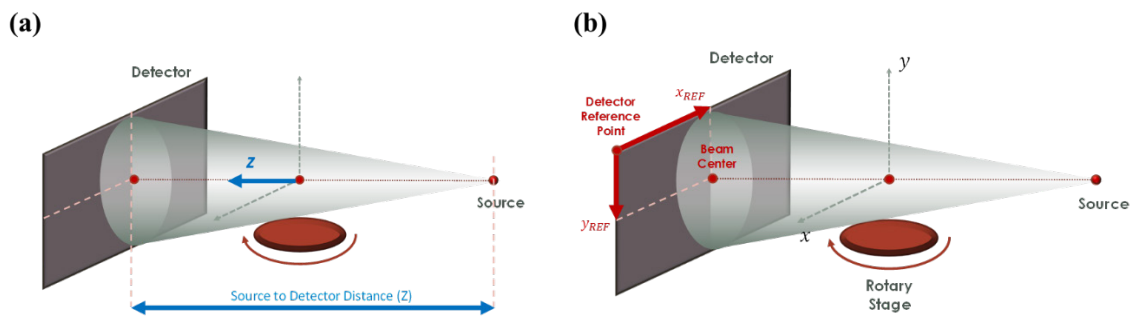


Figure 1.4.1 Sketch illustrates the configuration of the CT components.

Moreover, some parameters inside the tube, like centering coils and target anode shape may contribute to some variation to the focal spot position (z-coordinate in Figure 1.4.1a) and the output angle of the effective X-ray beam. The center of the beam is projected to the detector (x and y coordinates in Figure 1.4.1b) and does not coincide with the center of the detector. It can be determined through the detector calibration procedure. The center of the

beam will have the highest intensity and the beam will fade away towards the edges of the detector as the rays have to travel a longer distance. The detector calibration (or correction) takes this into account and averages all the values across the detector.

Lastly, for successful reconstruction of the data, it is essential to know the accurate position of the rotary stage with respect to the source and detector (x, y, z – coordinates), its tilt (if used), offset (in rare cases) as well as its angular position at each step of the rotation. Inconsistency or lack of precision of motion control hardware is very difficult to correct for and can lead to scrubbing of the entire scan. The level of positioning precision required for the CT system components is extremely challenging to achieve in the field inspection. The development of industrial solution would enable the inspections of airplane fuselages and helicopter panels while ‘on the wing’. Meanwhile, in order to perform a high-resolution X-ray CT, it is imperative that the structure fits inside the scanner. Among the most popular industrial CT systems are cabinet scanners and large envelope CT systems, which are typically installed in shielded vaults. Nevertheless, even the most advanced systems have geometric limitations when it comes to scanning very large aerospace parts.

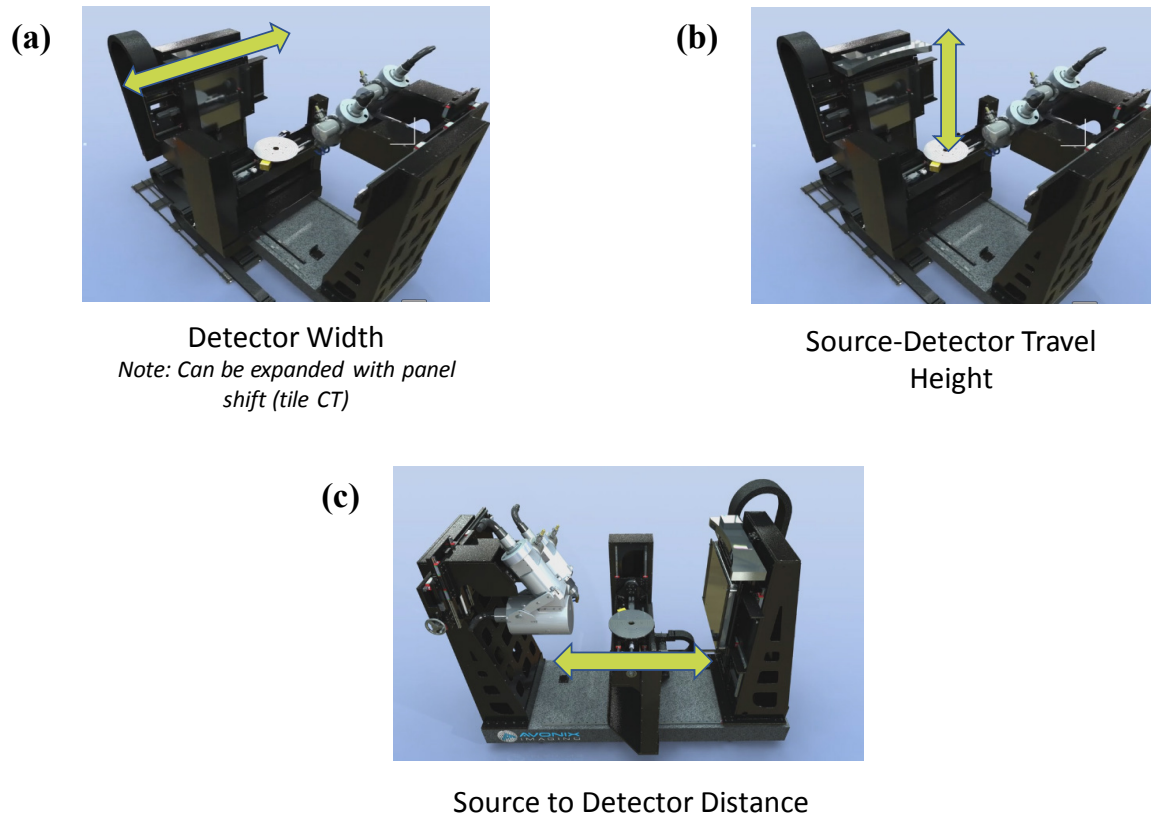


Figure 1.4.2 Geometric limitations of industrial CT scanner [Used with permission from <http://www.avoniximaging.com>]

Figure 1.4.2 illustrates the various limitations encountered in the industrial CT scanner on account of various geometric limitations. Even if the larger sized objects could be accommodated, the fundamental limitation remains the size of the detector. In order to alleviate this problem, a few commercial CT systems are built with a detector that is capable of in-plane (left-to-right) translation during scan acquisition, the technique commonly known as panel shifted or tiled CT.¹⁶ In the latter modality, by means of translating the detector, the entire field-of-view can be covered. The maximum height of

the object that can be scanned is defined by the height the source and the detector mounting towers can rise to. Beyond merely physically fitting inside the scanner, the entire area of interest of the structure should fall within the illuminated volume of the X-ray cone beam. The source to detector distance is the main parameter of object's geometric magnification. However, the maximum distance is specific and predefined to the scanner model, thus limiting the resolution quality that can be achieved.

The rotary stages are designed to hold objects weighing hundreds of kilograms. In some cases, the objects are required to be placed away from the center of rotation to accommodate for the area of interest within the field of view of the beam. Securing a heavy object off-center can present a challenge. Typically, only the bottom of the inspected structure is secured to the stage. Since its top end is relatively free to move, the part may experience imbalance during the angular rotation. This shift is very difficult to predict and correct for in volume reconstruction algorithms.

Even though radiation dose of the sample is not a concern in industrial CT, still the acquisition time of the scan might be of importance in a fast-paced production environment. High-fidelity CT inspection requires the collection of thousands of radiographs which can take from an hour to as long as ten hours or more, depending on the equipment and the scanning technique. For lengthy scans, there is a higher risk of receiving incomplete dataset, due to accidental operational errors like power tripping and outage, cooling problems, or the source unexpectedly turning off.

When presented with a situation of scan time constraint, the common solution would be to acquire fewer numbers of projections. However, the low angular sampling of the projections can lead to a potential loss of high spatial frequency information. Therefore, the operator might be faced with a dilemma of either setting an increased angular step to cover the entire 360° rotation, or rather getting a limited angle range of the critical area but with a higher angular step, producing an intentional limited angle scan.

As for the physical aspect, the flux of the X-ray beam changes with time. The warming up of the tube, in particular the focal spot, results in production of more energetic photons and generation of heat that can get convected into the room air. The response of the detector is also subject to slight change¹⁶ - it is known to ‘wake up’ after a certain time of continuous exposure to the X-ray photons. Both of these factors may contribute to the change in intensities recorded by the detector from the beginning towards the end of the scan acquisition.

It is common for image reconstruction algorithms to compare the first and last projections in order to correct for any changes during the course of the scan. As the scan proceeds, the beam flux as well as the response of the detector are subject to slight change.¹⁶ This variance during scan acquisition could induce the disparity between the recorded intensities of the images. In addition to poor fixture to the rotary stage, object movement could also be caused by the heat generated by the tube during X-ray production. In the event of any of the aforementioned phenomena, the algorithm might struggle to compensate for the changes and consequently generate image artifacts in the resultant 3D volume or even lead to a complete scrubbing of the entire scan. Sometimes, it is possible to

track when the changes initiated and reconstruct the portion of the dataset without the affected projections. Although this may lead to the loss of certain information due to the now truncated angular range, this allows for a significant retrieval of data, especially in the case when rescanning is not an option.

1.5 Motivation for Partial scanning techniques

The fidelity of the NDE methods for aircraft structures is not adequate at the present time. For example, it has been determined that the presence of small individual voids at critical locations rather than their total volume can drive reduction in the interlaminar strength and durability of composite structure.^{5, 10} Computed tomography can capture such defects; however it is currently limited to small cross-sections making X-ray CT impractical for aircraft structures. Since accurate NDE methods needed to quantify the smallest voids in the structure are necessary to determine the effects of defects on structural performance, such NDE methods for large structures must be developed.

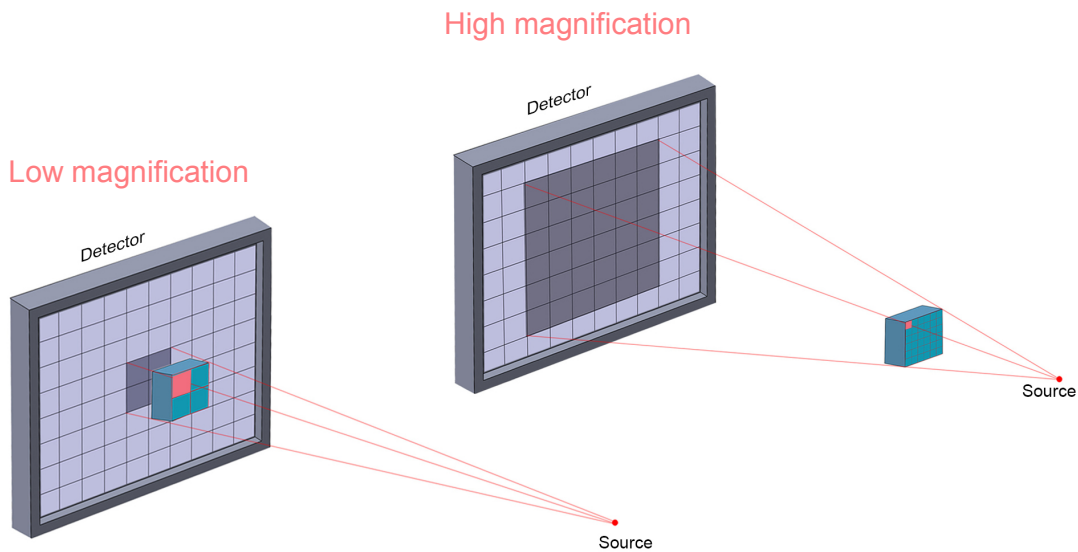


Figure 1.5.1 Geometric magnification in CT scanning.

The objective of this work is to assess the possibility for breaking through the current limits of X-ray Computed Tomography (CT) in order to enable high-fidelity nondestructive inspection of large aircraft structures. Currently, strict limitations related to

generating X-ray projections all around the inspected object in a full CT scan, prohibit CT application to large structures. The commercial industrial CT systems utilize full 360° projection angle range for high-quality 3D reconstruction of the inspected objects. The ability of the software methods used in such systems to reconstruct the details of the inspected object often becomes unacceptable as the range of projection angles decreases below 180°. In order to increase resolution, it is necessary to achieve a higher geometric magnification (**Figure 1.5.1**). The resolution in case of CT refers to effective pixel size. Smaller effective pixel size means improved accuracy, i.e. higher the ability to resolve features. Even if the flaws under investigation are small and located in the known areas of the inspected structure, the overall large size of the part can prevent the ability to generate the full range of X-ray projections. The same problem arises when high magnification (zoom-in) of the test specimen is required to detect smaller defects (**Figure 1.5.2**).

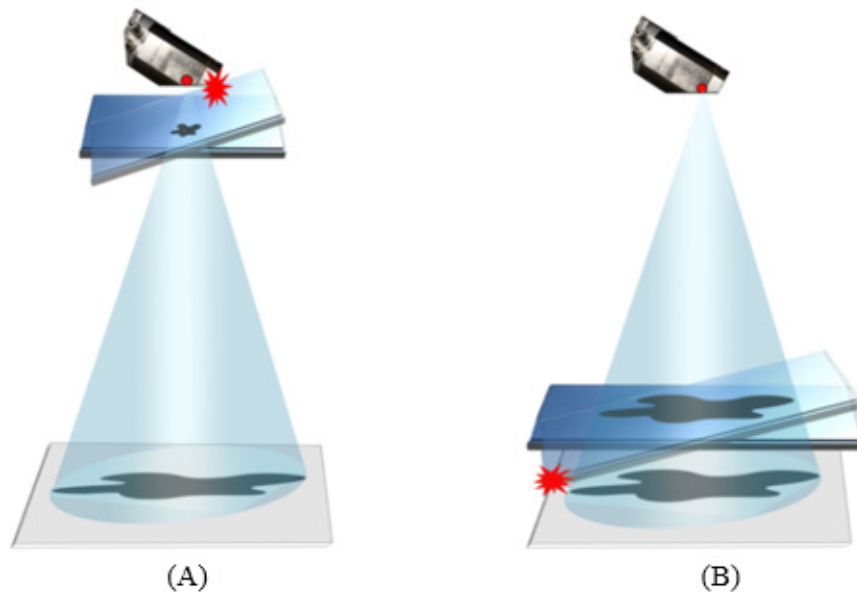


Figure 1.5.2 *The inspected object can be too large to make a full scan (A) or smaller object cannot make a full scan for the selected magnification (B).*

The most common composite structural elements in aerospace applications can be generalized as objects with large in-plane dimensions compared to thickness. In addition to the risk of collision with X-ray source at high magnification these parts suffer from poor penetrability in the in-plane direction. That makes it challenging to detect the defects and damage typical for aircraft composite structures. Thorough research on the suitable technique for scanning planar composite structures was performed in this work and is discussed in further detail later in this dissertation. The author's contribution to this dissertation was in the setup and acquisition of the scans shown in this work, implementation of Dr. Yuri Nikishkov's codes to reconstruct corresponding scan volumes, and the subsequent analysis and interpretation of their results.

Portions of text from Chapters 1, 2, 3, and 5 have been borrowed from previously co-authored publications cited below for reference:

1. Nikishkov, Y.; Bostaph, E.; Makeev, A. Nondestructive Inspection of Composite Structures Based on Limited Angle X-Ray Computed Tomography. **2015**

CHAPTER 2

PARTIAL SCANNING TECHNIQUES

2. Partial Scanning Techniques

Although in principle medical CT arrangement could potentially be applied for successful defect detection within long and slender aerospace components, several other challenges arise due to the demands posed on NDI of such composite parts. In the widely used clinical applications of X-ray CT, research efforts concentrate heavily around reduction of radiation dosage received by the patient. The amount of radiation is far less relevant in industrial applications. Among them, the higher resolution required during composite part analysis due to the dimensions of the expected flaws. Additionally, the flat nature of composite defects make them harder to detect as opposed to features within the human body that tend to have more detectable volume. The typical medical CT volume slices are too thick for adequate composite analysis.

As described previously, scanning of large-scale aerospace objects in particular limits the applicability of full 360° CT, which would be ideal for comprehensive part examination. The lack of portability of the CT system prevents use of the system on the field. Correspondingly, compromises have to be made to accommodate various practical geometric limitations encountered on-site. This leads to the problem of limited available scan angle ranges (less than 180°). Further, owing to penetrability limitations through the wider dimensions¹⁷ or malfunctioning of various CT components such as the source and/or detector (that tends to occur during lengthy scans),¹⁶ often some amount of the projection dataset can be ‘missing’.¹⁸ In a scenario where rescanning is not a feasible option, it is essential to be able to recover meaningful results that can allow for reasonable

interpretation from the limited datasets available. It is important to develop some rationale in order to anticipate the shortcomings in reconstructions resulting from insufficient datasets.

Tomosynthesis (TS) is an advanced method of inspection that uses X-ray imaging in conjunction with digital reconstruction to create volumetric renderings of scanned objects.¹⁶ Based on object's partial rotation, tomosynthesis scanning technique represents a middle ground between radiography and full-angle CT. It significantly enhances the resolution capability of single 2D X-ray systems, which still remains one of the most used imaging nondestructive inspection techniques in the industry. In some instances, two-dimensional radiography is the only viable option of inspection for variety of reasons, and mainly due to part accessibility restriction.

The following sections will further explore LAT and TS as pertains to composite structural analysis and the software challenges limiting current application. It is the aim of this work to extend the applicability of the CT systems to high-fidelity inspection of large aerospace composite structures by developing robust computational and scan acquisition protocol to enable efficient and reliable reconstruction of limited angle datasets.⁷ Section 2.1 will explore specifically the difficulties and progress made with regard to the algorithms seeking to reconstruct image volumes from insufficient datasets.

2.1 X-Ray CT Reconstruction Methods

Reconstruction from X-ray CT radiographs represents a photon transmission tomography problem that has been extensively studied since 1970s. A historical review on the

research in the field can be found in this reference.¹⁹ Typically CT reconstruction methods are divided in two categories: analytical and iterative methods. Analytical methods are superior in terms of performance and are used in the majority of commercial X-ray CT systems, both medical and industrial. Iterative methods are capable of higher quality reconstructions due to their flexibility to include detailed modeling of the tomography problem. Although this flexibility results in significant performance penalty, recent improvements in both computer hardware and reconstruction methods led to increased applications of iterative and stochastic methods. These reconstruction methods are now marketed in X-ray Computed Tomography systems by GE Medical and Siemens.²⁰

2.1.1 Analytical Reconstruction Methods

Most of the analytical reconstruction methods are based on the projection slice theorem²¹ that links Fourier transform of a projection at particular angle to a central slice at the same angle of the Fourier transform of the scanned object densities. The typical algorithms used in medical devices use convolution-backprojection: first, Fourier transforms of projections are convolved with the filtering kernel and second, the inverse Fourier transforms of filtered slices are backprojected in the object space. An algorithm of this type that uses a ramp filter is usually referred to as filtered backprojection (FBP)²¹ and often serves as a benchmark for the newly proposed reconstruction algorithms.

Industrial X-ray CT systems that use flat-panel detectors implement a variation of the FBP algorithm proposed in **Feldkamp et al** called Feldkamp or FDK algorithm.²² In the Feldkamp algorithm, the convolution step is applied to one-dimensional rows of the flat panel detector and the backprojection step is carried out in the three-dimensional object

space. Although this solution is approximate, especially for the slices away from the center of the beam, it is favored by industrial implementations due to its computational efficiency and ability to be executed on highly parallel vector processors available in modern computer hardware.

Tomographic reconstruction from limited projection angles was recognized as important problem since 1980s. In principle, perfect reconstruction from an infinite set of limited angle tomographic data is possible.²³ In practice, due to being extremely ill-posed, LAT reconstructions are very sensitive to noise in measurements. Increased detector resolutions of modern X-ray detectors help improving LAT reconstructions by providing more data in higher number of projections.

Analytical reconstruction methods show quick deterioration of reconstruction quality when smaller number of viewing angles is used due to idealized assumptions on the tomography system such as point source, uniform detector response, and white (unspecific) noise in projections. Improved projection system definition as well as particular solution properties are difficult to incorporate in the analytical reconstructions as most of this prior knowledge cannot be expressed as filters in Fourier space.

2.1.2 Iterative Reconstruction Methods

Iterative reconstruction methods have an important advantage of being extremely flexible in specifying more accurate projection system models, material attenuation and X-ray energy spectrum models, allowing for explicit modeling of the projection system. Historically, iterative methods based on the algebraic formulation were the first reconstruction methods proposed (ART and later SART).^{21, 23} These methods introduced large variety of system

formulations but had few practical implementations due to computational cost. Another noteworthy implementation is the Gerchberg-Papoulis²⁴⁻²⁵ family of algorithms.²⁶ The latter address the problem of missing data in band-limited signals by alternating a low-pass filter in space and frequency domains. Later, stochastic formulations renewed the interest in iterative methods due to their improved handling of noisy problems.

The first stochastic reconstruction proposals²⁷ considered photon statistics and formulated the reconstruction problem as maximum likelihood estimation. The formulation was especially beneficial for the photon emission problem (PET/SPECT scanners) as the emission scans exhibit much lower photon counts compared to the transmission tomography.

2.2 Limited Angle Tomography

The first practical LAT proposals²³ have shown the ability to reconstruct only a low frequency content of solution but not the sharp boundaries between the phases. The Radon transform that integrates functions over lines is the basis of reconstruction. It maps the object space into a set of projections. The problem arises when data is missing, such as in practical applications where only a finite number of lines are provided. The exterior problem presents a large sub-class of the limited angle problem that frequently arises when scanning objects (usually with circular cross-sections), where X-rays do not penetrate through their center due to high density or large measurement in the respective direction. This issue is important especially in aerospace and other industrial applications where penetrability is limited due to the large sizes of the involved objects. The critical need to

detect defects in such large structures in critical applications has led to a large amount of work trying to address this issue.

Quinto²⁸ provides an excellent background regarding the development in this regard given the failure of the classical filtered backprojection (FBP) to provide satisfactory reconstruction results from incomplete and noise affected datasets.²⁹⁻³⁰ Notably, the work of Cormack³¹ and Helgason,³² provided Quinto³³⁻³⁵ with the basis to develop a reconstruction algorithm based on singular value decomposition, commonly known as SVD algorithm. Quinto has shown that sharp discontinuity is reliably recoverable only if available projections contain rays tangent to the curve that represents a discontinuity,³⁴ otherwise the discontinuity cannot be reconstructed by any algorithm based on projection data only. Note that this statement refers to reconstruction of sharp discontinuities (high frequency content); edges unobserved by Quinto are still partially visible and often visually detectable. Beyond SVD method, other notable factorization methods include wavelet decomposition³⁶ and projection onto convex sets (POCS).³⁷⁻³⁸

Stochastic reconstruction methods brought new interest to LAT as they are well suited for the ill-conditioned problems with missing or inconsistent projections. They have the advantage of being extremely flexible in specifying more elaborate tomography system models as well using the ad-hoc knowledge about scanned object structure. For example, potential improvements in modeling forward-projection operator include: using photon statistics; modeling non-point X-ray source and discrete detector points (or, alternatively, a point spread function); modeling multi-energetic X-ray spectrum and material X-ray attenuation energy dependency.³⁹⁻⁴⁰ Stochastic methods naturally allow explicit modeling of noise in the system

based on the analysis of experimental measurements. Finally, an iterative solution can be started from the solution by the analytical method and then improve until a quality criterion is reached.

At this time test specimens are essentially reconstructed using fewer projection angles. Both analytical and iterative methods have no algorithmic limitations as far as the amount of radiographs or angular range. When projection data becomes insufficient for reconstruction, inherent noise in projections dominates actual density data and prevents recognition of features. Typically, LAT reconstructions demonstrate highest quality in the plane perpendicular to the line bisecting the angular projection region (parallel to detector); and capable of significantly smaller resolution through the thickness of this plane. Artifacts due to insufficient data become more apparent away from the focus point of the scan. Although no specific changes for LAT are required, a successful LAT reconstruction algorithm have to rely on using as much prior knowledge on the reconstructed data as possible; and include data and system modeling that is targeted for scanned object geometric and material structure.

2.3 Tomosynthesis

The concept of tomosynthesis has been around for a long time. It was developed in 1930s, long before the widespread practical application of CT.¹⁶ There has been renewed interest for hardware implementation of tomosynthesis in the medical field due to reduced radiation dose it has compared to full CT. Advanced digital radiography systems have already been built and extensively used in clinical applications to examine areas of human body that have previously been uncertain in conventional 2D radiographic imaging. This technique is commonly referred to as Digital Tomosynthesis⁴¹ with a more specialized

application called Digital Breast Tomosynthesis (DBT)⁴² or mammography tomosynthesis. Preliminary studies suggests that the DBT offers higher sensitivity and has approximately 15% reduction of false negative of detecting breast cancer when compared to conventional mammography.⁴³ This is achieved due to improved grey scale contrast, reduced background noise level and ability to analyze separate individual slices of morphological elements which were previously superimposed in two-dimensional images.

Although the system configurations differ between manufacturers, the principle of tomosynthesis remains the same. As an example, the GE XR656 system has a flat detector fixed in place under the table where the object is placed and the X-ray tube undergoes linear translation and rotation over the area of interest. There is an option of having the human subject stand vertically and with the detector being placed behind the area that needs to be scanned. The source is subsequently translated and rotated simultaneously while constantly keeping the examined area in the field of view (as seen in Figure 2.3.1). In the case of some DBT systems, the source moves along an arc path illuminating a fixed flat panel detector.

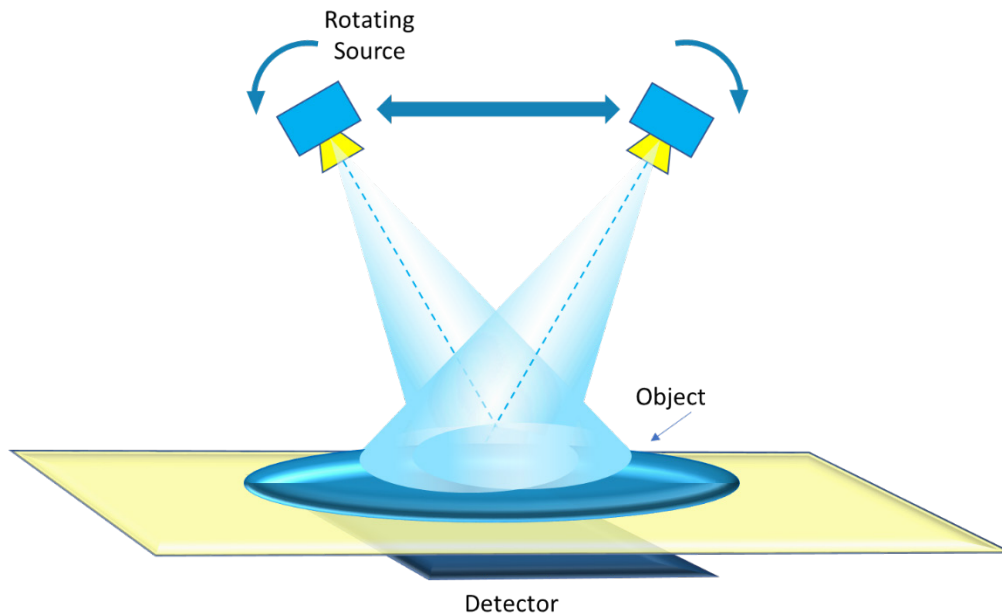


Figure 2.3.1 Basic schematics of medical digital tomosynthesis modality (adapted from GE XR656).

It is worth noting that the X-ray tube commonly used in medical applications is relatively lightweight making it feasible to maneuver in different trajectories. The concept of tomosynthesis has also been commercially applied for inspection of printed circuit boards (PCB), commonly termed computed laminography.⁴⁴ In contrast to the previously described configuration of medical DTS systems, the computed laminography system typically incorporates a fixed source located under the table upon which the object is placed and has a tilted detector that moves along a circular path around the user defined area of inspection during scan acquisition. Figure 2.3.2 illustrates the schematics of the operating configuration of CL.

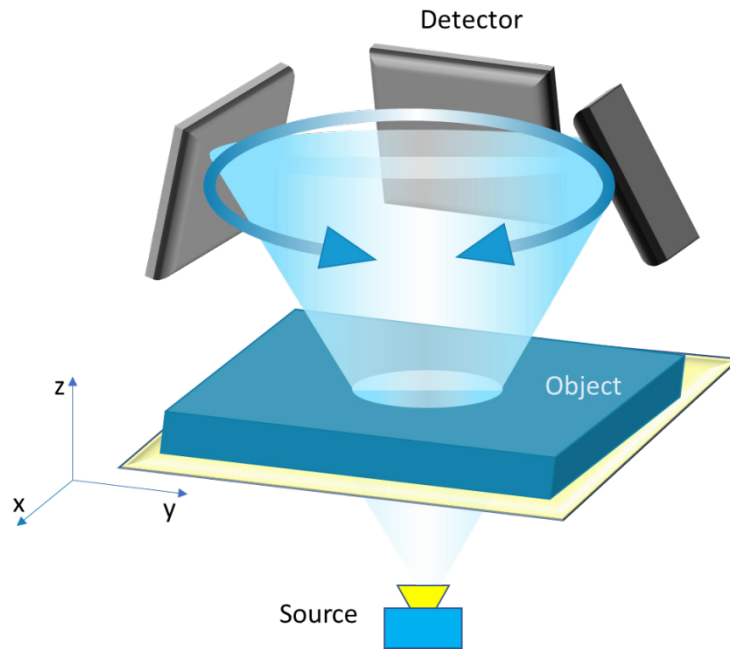


Figure 2.3.2 Schematic configuration of computed laminography system (adapted from Shimadzu Xslicer model).

There are two fundamental parameters that govern the quality of tomosynthesis scan: the source-to-object distance and the angular range of the scan. “Source-to-object” (SOD) and source-to-detector distances define geometric magnification of the inspected object and essentially dictate the spatial resolution obtained by the scan. Since in most commercial tomosynthesis configurations the inspected object is placed practically on the detector itself, the terms for above mentioned distances are interchangeable. In practice, SOD in TS defines the ultimate resolution the scan can achieve.

When the object is placed close to the source, i.e. SOD is minimal – the in-plane spatial resolution is the highest. Therefore, the recorded level of detail is maximum, which allows

for the best probability to distinguish smallest features within the respective projection. As the object moves away from the source, the SOD increases, consequently negatively affecting the spatial resolution and the sharpness of the resolvable features.

Angular range is the scanning parameter that adds the depth information to the volume of the scanned object. By obtaining projections from the extreme viewpoints of the acquisition angle range, it is possible to get the location of the features within the thickness of the object. While a 2D radiograph represents a summed image of all the features of the object superimposed in one plane, it makes interpretation of the image complicated. Additional projections from different angular views help separate that image to slices through the volume adding more depth and therefore help reduce the confusion over examination of the inspected object. The depth information acquired through a narrow angular range would be limited as compared to the one from a wider range.

Nevertheless, in tomosynthesis setup the tilting angle of the source becomes the conflicting parameter that defines the tradeoff between the depth perception and the in-plane spatial resolution. In order to expand the angular range, the source has to move further away from the object, thus lowering the resolution. As a result, tomosynthesis technique combines the benefits of the high resolution close-up views with significant depth information from the acquisition angular range.

The original medical DTS system incorporates a lightweight X-ray tube that uses linear translation and rotation during the acquisition of the scan. By moving it transversely it progressively acquires a series of projections at different magnifications. The area of

interest is being continuously exposed to X-ray beam by means of rotation of the tube. The resulting projections are being processed by reconstruction software to recreate a 3D volume of the object. Figure 2.3.3 demonstrates the relative X-ray source and object positions during the tomosynthesis scan.

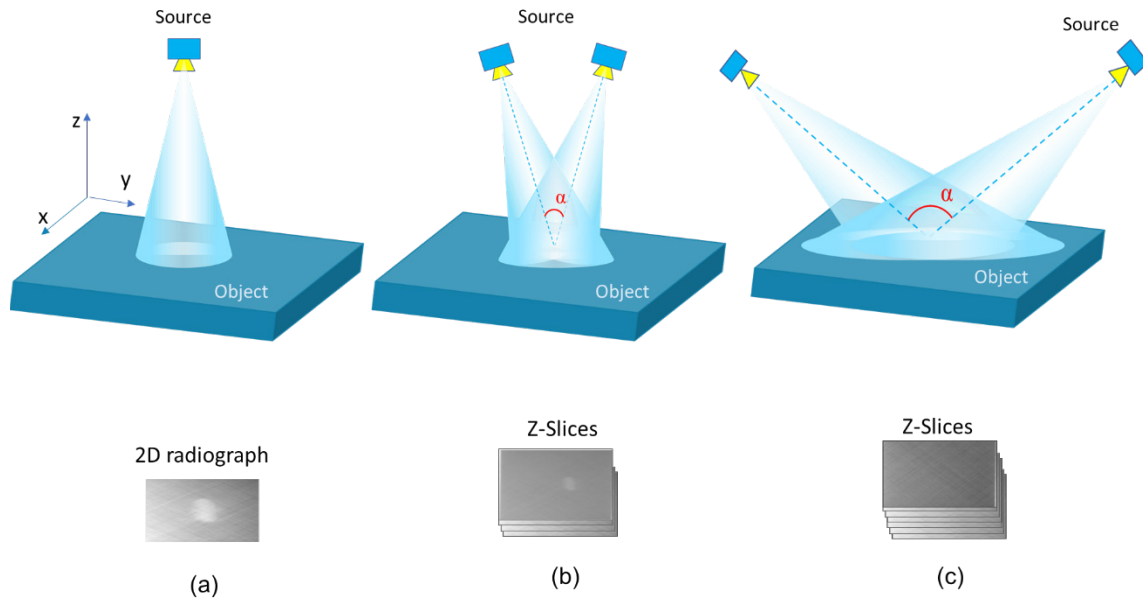


Figure 2.3.3 X-ray source and object positions for tomosynthesis - (a) single 2D radiograph, (b) narrow and (c) wide acquisition angular ranges.

Figure 2.3.3a shows the position of the source during the acquisition of a single 2D radiograph at the smallest SOD. This projection provides information about the in-plane dimensions of the features in the area of focus, but no depth information. Therefore, it is impossible to say with fidelity number of features that got superimposed in the radiograph and their precise location in the volume. The depth information can be retrieved by adding another radiograph from a different angular viewpoint, like shown in Figures 1.7.3b and

1.7.3c, which illustrate the two extreme cases of a small and large angular range that the tube undergoes during the scan acquisition.

Figure 2.3.3b shows a narrow angular range. As can be observed, the source is placed directly above the object and SOD is maintained relatively constant throughout the scan but provides advantages of giving some depth perception as opposed to a single radiograph, acquired at the same distance. Figure 2.3.3c shows a wide angular range that provides maximized information regarding the depth, however, with decreased resolution. To reiterate, in order to simultaneously achieve both high depth resolution as well as optimal reconstruction quality, the choice of angular range becomes a critical criterion.⁴⁴

CHAPTER 3

RECONSTRUCTION METHODS

3. Reconstruction Methods

3.1 Idealized System

For simplicity, let's consider a 2D problem, with the object spatial domain and projection domain. The transition between the two is described by operations called 'projection' and 'backprojection'. The concept of the two operations is very similar: the forward-projection facilitates the transition from the object to the projection domain, and the backprojection superimposes the projection data into the object space domain at an angle of acquisition.

In mathematical notation, the object domain and its geometry can be described by linear projection operator A and its transpose A^T denotes operation backprojection. The discretized object space and its projected values can be represented by column vectors x and y respectively. The projections represent a summed value of all the density values along the line of the incident ray. Therefore, for the idealized problem in the absence of noise and even X-ray beam itself, the projection operation can be written as follows:

$$y_i = [A]_{ij} \cdot x_j \quad (3.1)$$

$$A = \begin{bmatrix} a_{11} & \dots & a_{1j} \\ a_{21} & \dots & a_{2j} \\ \vdots & \ddots & \vdots \\ a_{i1} & \dots & a_{ij} \end{bmatrix}, x = \begin{bmatrix} x_1 \\ x_2 \\ \vdots \\ x_j \end{bmatrix}, y = \begin{bmatrix} y_1 \\ y_2 \\ \vdots \\ y_i \end{bmatrix}$$

The task of tomography reconstruction becomes to recover the unknown object vector x from its projections y . In practice, this problem is complicated by the fact that the matrix A is non-square, sparse and rank-deficient and thus does not have an inverse, making the

solution of $A^{-1}y$ unobtainable. It is also worth noting that the idealized version of the tomography problem assumes the entire continuum of projections $p_\varphi(r)$ is available as opposed to discrete set of projections and rays.

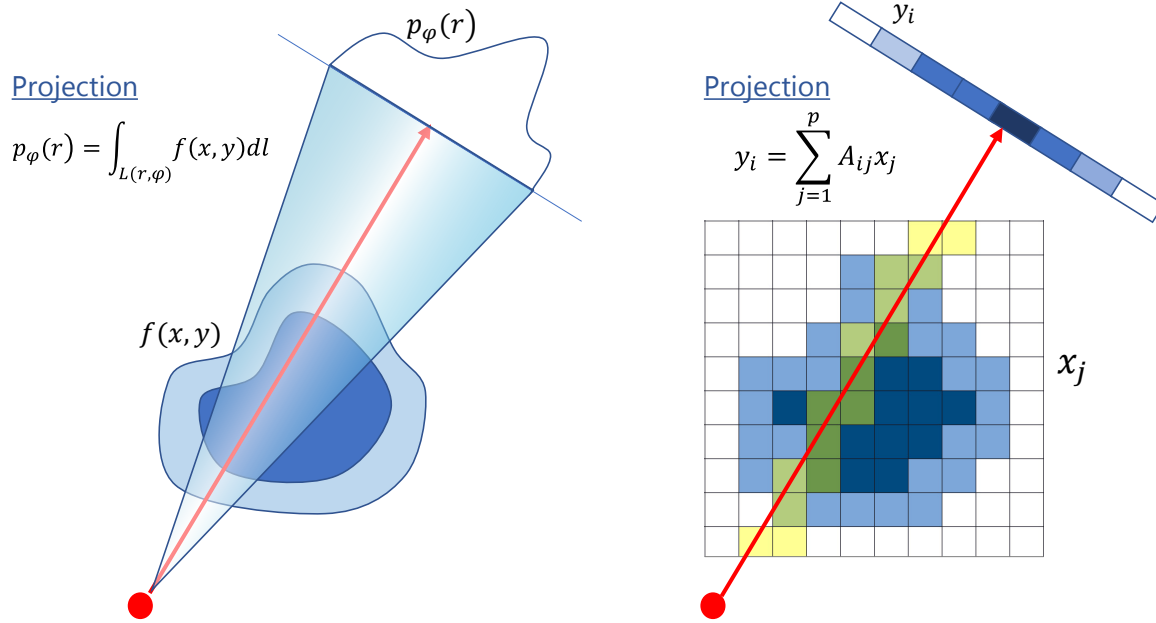


Figure 3.1 Analytical vs discrete model.

For simplicity, a 2D object that can be described by a density function $f(x,y)$ is assumed. In reality, the object's representative function is unknown. **Figure 3.1** illustrates the projection model for analytical and discrete case. The basis of reconstruction is the analytical solution to the inverse problem called Radon transform, which maps a 2D object domain function $f(x,y)$ to the 1D line integrals through the object, called projections $p_\varphi(r)$. The goal of image reconstruction is to recover the function from its projections, obtained from a finite number of angular viewpoints. It is a common practice to use an operation called 'backprojection' to resolve the objects unknown density function. For every incident

beam at a certain angle, the projection is ‘smeared’ into an object domain, therefore resulting in summation of the intensities in every pixel.

$$f_b(x, y) = \int p_\varphi(r = x \cos \varphi + \sin \varphi) d\varphi \quad (3.2)$$

The central slice theorem (**Figure 3.2**) ensures the basis for this mathematical operation between the Radon transform and the 2D Fourier transform $F(k_x, k_y)$, (where k_x, k_y are spatial frequencies corresponding to x, y), and $f(x, y)$ can be recovered from $F(k_x, k_y)$ by an inverse 2D Fourier transform. The central slice theorem states that the 1D Fourier transform of projection $p_\varphi(r)$ (Radon transform of (x, y)) equals the slice at angle φ through the 2D Fourier transform of $f(x, y)$.

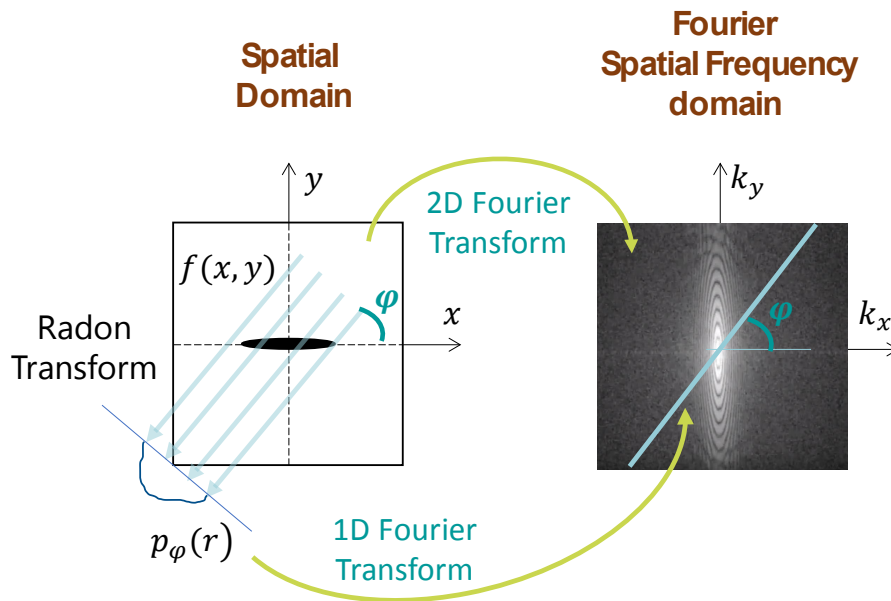


Figure 3.2 Central Slice theorem

Unfortunately, the direct backprojection is only an approximate inverse for Radon transform and leads to the overly smooth and blurry images. Moreover, inverse Radon transform is defined in continuous domain and is not practical for discrete solution. Commercial codes implement a feasible solution to this problem by applying the filtering operation in the Fourier domain, called filtered backprojection(FBP).⁴⁵ .

$$f(x, y) \rightarrow \text{Project: } P_\varphi(r) \rightarrow \text{Filters: } \hat{p}_\varphi(r) \rightarrow \text{Backproject: } f(x, y)$$

$$\hat{p}_\varphi(r) = F^{-1}\{F(p_\varphi)|s|\} \quad (3.3)$$

$$f(x, y) = \int \hat{p}_\varphi(x \cos \varphi + y \sin \varphi) d\varphi \quad (3.4)$$

Where φ – acquisition angle, $P_\varphi(r)$ -projection, \hat{p}_φ - filtered projection, F- Fourier transform

The Fourier domain is characterized by having low sampling frequencies densely packed at the origin and high frequencies at a larger distance away from the origin. This results in the higher frequencies having less weight when being backprojected into the image domain. By applying a ramp filter (**Figure 3.3**), measurements with high spatial frequencies can be provided with more weight and the sharp contouring edge of the object's contour can be retrieved.

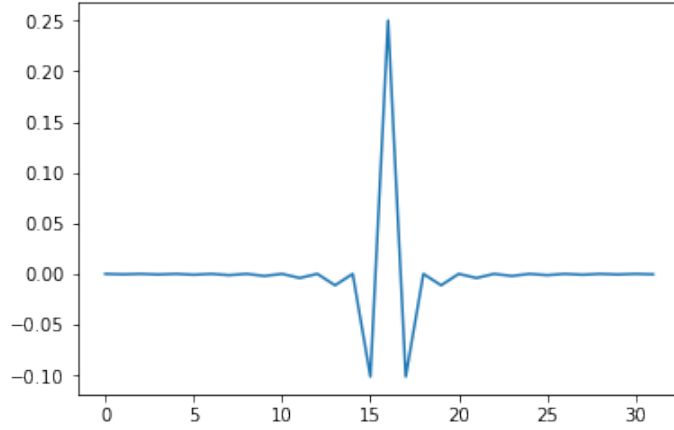


Figure 3.3 Ramp filter in discretized image space domain

Since the image space in CT reconstruction is discrete, the ramp function is sampled according to Nyquist theory,⁴⁶ without loss of information:

$$ramp(n) = \begin{cases} \frac{1}{4}, n = 0 \\ 0, n \text{ even} \\ -\frac{1}{(n\pi)^2}, n \text{ odd.} \end{cases} \quad (3.5)$$

Fourier transforms of projections are convolved with the filtering kernel : $q_\phi(n) = p_\phi(n) * ramp(n)$ and consequently, are backprojected into the object space domain to recover the object function.

Another important consideration for FBP reconstruction is an angular sampling frequency. The number of projections acquired over the range can be a significant factor in forming aliasing artifacts (Figure 3.3) in reconstructed image volume.

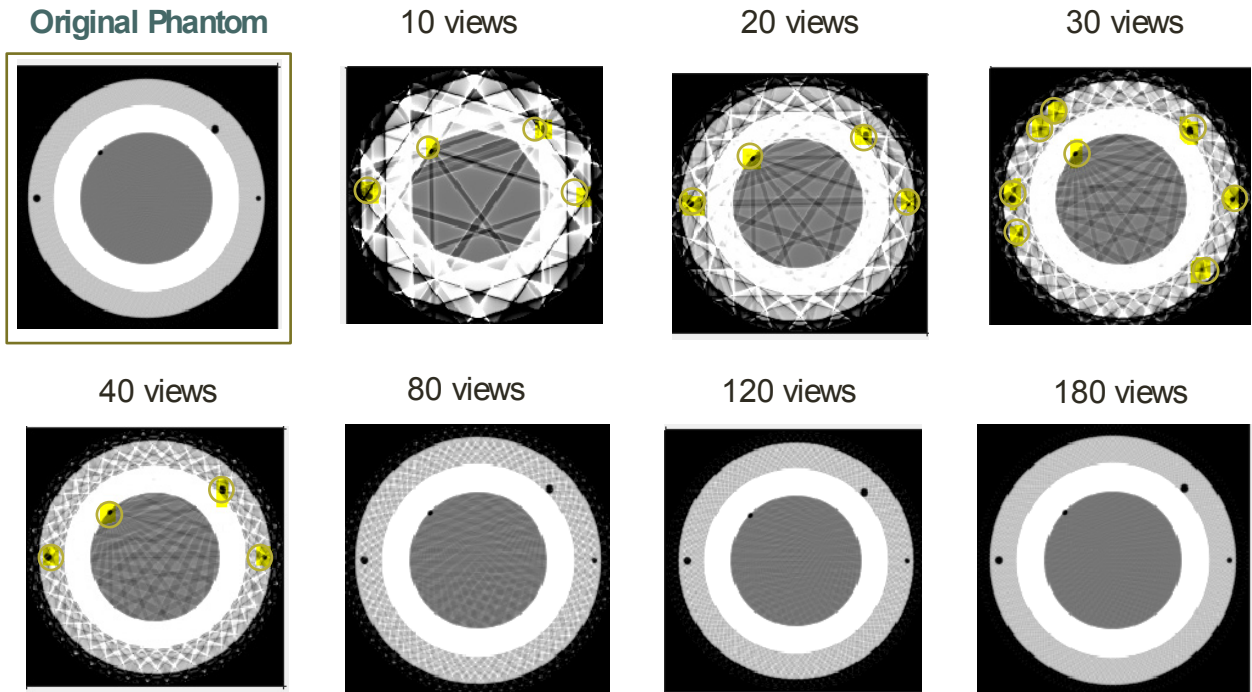


Figure 3.3 Illustration of the effects of angular undersampling on image quality for FBP reconstruction.

The detailed description of Figure 3.3 and observed artifacts is provided in **Appendix A**.

3.2 Physical Model

Solution methods which have a potential of incorporating a more realistic physical model of the computed tomography have received a lot of development over the past decades. Among the most attractive features, which cannot be achieved with analytical FBP method is the algorithm's ability to account for polyenergetic nature of the beam, object's energy-dependent attenuation, finite shape and size of the X-ray source focal spot and scattered radiation. Iterative reconstruction methods have an important advantage of being extremely flexible in specifying more accurate projection system models, material attenuation and X-ray energy spectrum models, allowing for explicit modeling of the projection system.

The ideal system model, described in eq.3.1 does not contain any noise in its data. Stochastic tomographic methods of reconstruction, based on the Bayesian approach can help account for noise in the projections. The concept of their solution is to maximize *a posteriori* probability of estimating the object density x from the observed projections y :

$$p(x|y) = \frac{p_{prior}(x)p(y|x)}{p(m)} = \frac{p_{prior}(x)p_D(y - Ax)}{p(m)} \quad (3.6)$$

In order to model a true representation of projection system, noise is modeled by variance matrix D . The solution is sought in the least squares sense, such that the solution is non-negative and the following cost function is minimized

$$\Psi(x) = \frac{1}{2}(y - Ax)^T D (y - Ax) + \beta R(x) \quad (3.7)$$

Weighted least squares term is the maximum likelihood estimation of solution and regularization term $R(x)$ reflects *a priori* knowledge of solution properties. Damping parameter β is usually found by trial and error. It should be noted that optimization problem is constrained as the solution cannot assume negative values. The diagonal noise matrix can be defined as:

$$D = w_i = \frac{(Y_i - r_i)^2}{Y_i} \quad (3.8)$$

where r_i is scatter background (infinitely dense object).

Using identity matrix ($D = I$) leads to a maximum likelihood solution given that the observations contain Gaussian noise. Term $R(x)$ is a regularization term that is necessary

to attract solution to a known average or to preferred properties. Without regularization solution often becomes oscillatory and approximates noise more than actual data. Commonly used regularization was provided by Tikhonov: $R(x) = \|x\|^2/2$ is useful when the solution is “normally” zero corresponding to no object present. Another example of regularization terms is the family of smoothing priors $R(x) = \sum_i \sum_{k \in N(x_i)} \varphi(x_i - x_k)$ with $\varphi(x) = x^2/2$. Edge-preserving priors such as Hyperbola prior $\varphi(x) = d^2 (\sqrt{1 + (x/d)^2} - 1)$ and Lange prior $\varphi(x) = d^2 (|x/d| - \log(1 + |x/d|))$ are used to exclude sharp boundaries from overall smoothing.

The difficulty arises from the fact that for practical problems matrix A is so large that even sparse matrix storage does not fit in the modern computer memory. Also, somewhat counter-intuitively, due to extremely large size of the system matrix, it turns out that building the matrix leads to less optimal performance. Solution to a large system given in Eq. (3.8) is typically sought using iterative methods. Therefore, methods of this type only require numerical implementation of projection of trial solution and back-projection of weighed errors.

3.3 Solution Methods

3.3.1 FDK (Feldkamp, Davis and Kress) Algorithm

Variation of the FBP algorithm, called Feldkamp or FDK algorithm, is commonly used in application for cone-beam 3D tomography. In the Feldkamp algorithm the convolution step is applied to one-dimensional rows of the flat panel detector and the backprojection step is carried out in the three-dimensional object space. Although this solution is

approximate, especially for the slices away from the center of the beam, it is favored by industrial implementations due to its computational efficiency and ability to be executed on highly parallel vector processors available in modern computer hardware.

3.3.2 Penalized Weighted Least Square Method (PWLS)

Penalized weighted least-squares (PWLS) method⁴⁰ uses radiographs to add weight to observations that contain less noise in the registration system. It incorporates knowledge of the physical model in the solution.

As an X-ray beam goes through the object's space domain at a certain angle, the corresponding measurement of X-ray damping is registered by a linear detector array in the form of greyscale values. The signal intensity attenuated by scattering and absorption can be described by Beer Law, which relates incoming intensity level to the photon intensity damped by the object with x attenuation. The realistic physical projection can be described by Eq 3.7:

$$Y_i = \int I_i(\varepsilon) e^{-\int \mu(x,y,z,\varepsilon) dl} d\varepsilon \quad (3.9)$$

Assuming Poisson statistics for the radiograph observations $Y_i \sim \text{Poisson}\{b_i e^{-[Ax]_i} + r_i\}$, Elbarki and Fessler⁴⁰ give the log-likelihood expression for transmission tomography:

$$L(x) = \sum_{i=1}^N \{Y_i \log(b_i e^{-[Ax]_i} + r_i) - (b_i e^{-[Ax]_i} + r_i)\}, \quad (3.10)$$

where $b_i + r_i$ -blank detector response (no object), r_i - is scatter background (infinitely dense object).

$$-L(x) = \sum_{i=1}^N g_i([Ax]_i) \quad (3.11)$$

The negative log-likelihood can be otherwise written tin the following form:

where

$$g_i(l) = -Y_i \log(b_i e^{-l} + r_i) + (b_i e^{-l} + r_i) \quad (3.12)$$

After applying a second-order Taylor expansion to $g(l)$ and assuming the projection values are non-negative after the background scatter is subtracted from them, the line integral can

$$\hat{l}_i = \log\left(\frac{b_i}{Y_i - r_i}\right) \quad (3.13)$$

be estimated with:

$$g_i(l) \approx (Y_i - Y_i \log Y_i) + \frac{\omega_i}{2} (l - \hat{l}_i) \quad (3.14)$$

By substituting the line integral approximation, the function becomes:

Where ω – weighting factor.

The resulting PWLS cost function is:

$$\phi(x) = \sum_{i=1}^N \frac{\omega_i}{2} ((Ax)_i - \hat{l}_i)^2 + \beta R(x) \quad (3.15)$$

$$\hat{x}_j = \left[\hat{x}_j - \frac{M \sum_{i \in S} a_{ij} \omega_i ([A\hat{x}]_i - \hat{l}_i) + \beta \left. \frac{\partial S}{\partial x_j} \right|_{x=x_{old}}}{\sum_i \frac{a_{ij}^2 \omega_i}{\alpha_{ij}} + \beta \left. \frac{\partial^2 S}{\partial x_j^2} \right|_{x=x_{old}}} \right] \quad (3.16)$$

The iterative solution to the optimization problem is:

3.3.3 Least Squares Method (LSQR)

LSQR is an unconstrained least-squares optimization method available in the Python-Numpy package and based on Golub-Kahan bi-diagonalization.⁴⁷ Although it may produce negative solutions, typically only a few small negative terms appear, and rescaling produces a visibly good solution.

3.3.4 Tomosynthesis Solution Method

The proposed TS method was carried out using the following procedure. First, three consecutive scans of an object were acquired at three different working distances. The detailed scan acquisition procedure is provided in Chapter 4. Thereafter the projections datasets were calibrated, transformed, merged and reconstructed together to form a single image volume. The methods described above (FBP, LSQR, PWLS) were used for the solution of TS problem.

Due to the tremendous computational resources required for this work, it was chosen to acquire scans at only three different working distances. Although in real applications, a far greater number of scans at smaller distance increments would be desirable to prevent large gaps in data, the three scans used in this study were meant to serve as a proof-of-concept.

Immediately after acquisition, the scans require 3D calibration step to obtain geometry parameters specific to each scan. They include the distances of X-ray CT components in relation to each other, the highly accurate location of the axis of object's rotation, its offset from the beam center and tilt (if any), described by the 3D vector orientation. Additionally, each image volume is described by its voxel size and resolution, which consequently define the way geometry of the incident X-ray beam will be projected into the detector elements. The final step of backprojection procedure is entirely described by the geometry of the scan configuration and needs to be interpolated from the detector pixel readings into the grid of the image volume. All the geometric parameters of the scan acquisition are described by the system matrix $[A]$, which is different for every scan.

Therefore, after the three scans at different distances are obtained, the following system of equations is considered:

$$\begin{aligned} y_1 &= A_1 x \\ y_2 &= A_2 x \\ y_3 &= A_3 x \end{aligned} \tag{3.17}$$

where y_1, y_2, y_3 – three projections datasets, acquired from three scans at different distances, and A_1, A_2, A_3 – system matrices which describe the geometries of the scan configurations, x – the object's attenuation map that is assumed the same for all the scans.

After the datasets have been transformed from perspective to orthogonal space and projected into the image volume, it is possible to combine information from all three scans to seek for a single solution of the object's attenuation $[x]$. This operation is implemented in a different way depending on the reconstruction method chosen for the solution.

In the case of FBP algorithm, each equation from the system of equations provided in (eq 3.16) is solved individually following the common procedures, then a ramp filter is being applied specific to dataset geometry and at the step of backprojection the resultant x_{TS} would be an average of all three solutions. Following the above discussion of unavailable immediate solution in the form of $A^{-1}y$, the more general notation with the use of filter f is introduced: $A^T f(y)$.

$$x_{TS} = \frac{A_1^T f(y_1) + A_2^T f(y_2) + A_3^T f(y_3)}{3} \quad (3.18)$$

For iterative method, it is necessary to construct a new system matrix, incorporating all three system matrices from the scans and merge the vector projections in one by joining vectors and matrices row-wise.

$$y_{TS} = \begin{bmatrix} y_1 \\ y_2 \\ y_3 \end{bmatrix} \quad (3.19)$$

$$A_{TS} = \begin{bmatrix} A_1 \\ A_2 \\ A_3 \end{bmatrix} \quad (3.20)$$

In tomosynthesis, least square method seeks to minimize the objective function, representing the sum of squares of each component:

$$\sum_i^3 \|y_i - A_i x\|^2 = \|y_1 - A_1 x\|^2 + \|y_2 - A_2 x\|^2 + \|y_3 - A_3 x\|^2 \quad (3.21)$$

The result of optimization of eq 3.20 represents the solution for the object's density. This is anticipated to be a favored solution method, since the contributions from all three scans can be merged to find an improved image volume solution. Here, optimization is applied at the step of reconstruction itself as opposed to FBP approach, where the resultant reconstructed solutions are summed and averaged to form a final volume. The high-performance implementation of the above methods in this work is described further in **Appendix B**.

3.3.5 Solution Implementation

The tremendously computationally intensive solution methods described above were implemented using the codes developed by Dr. Yuri Nikishkov at the Advanced Materials and Structures Lab in UT Arlington. The implementation of Dr. Nikishkov's high-performance codes could accomplish reconstructions of problems with more than 100 million variables (and comparable size of projection vectors) within one minute per iteration; and typical iterative reconstruction arrived to stable solution in less than 10

iterations.⁷ The powerful computational tool allowed for implementation of the proposed TS to realistic problems, which commercial codes would struggle to successfully handle.

CHAPTER 4

EXPERIMENTAL SETUP

4. Experimental Setup

4.1 Scanner Description

A schematic of the concept of work of X-ray tomography is shown in **Figure 4.1.1**. The part being scanned is exposed to X-rays, which projects the part image on the X-ray detector. The machine repeats this process several times at specified angles that span 360° (it could span less than 360° in the case of a partial scan). Those scans are stored as high-resolution image files on the computer. After all the projections are completed, the reconstruction process takes place.

It uses one of the several reconstruction algorithms available to deduce a 3D solid or surface, from all the projection data obtained from the X-ray scans acquired earlier (2D scans). Feldkamp-Davis-Kress (FDK) filtered back-projection reconstruction algorithm²⁰ is one of the most widely used reconstruction algorithms nowadays for its relative speed. These scans usually have a voxel size which is inversely proportion to the magnification at the time of the scan. After the reconstructed volume is created, it can be further studied for defects or damage.

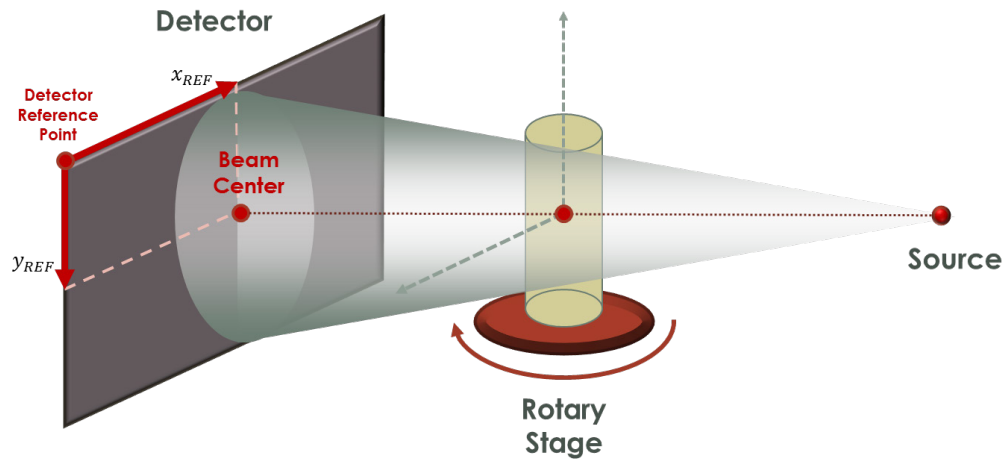


Figure 4.2.1 Schematic CT setup. The calibration procedure determines the reference point of the X-ray beam center projected into the detector.

For this work, the North Star Imaging X5000 computed tomography machine at the AMSL lab at the University of Texas at Arlington was used. This machine is fitted with an X-ray WorX, micro-focus, reflection cone X-ray tube. The machine can achieve volumetric resolutions of less than 10 μm .

4.2 Tomosynthesis Procedure

Figure 4.2.1 shows three LAT scan setups, each performed with the axis of rotation positioned at different distances with respect to the source. As the SOD increases, wider angular ranges can be accommodated. The more number of angular views acquired from the wider range scans, allow for greater detection of indications within the thickness of the part. It should be noted that this comes at the price of decreased resolution owing to the increased SOD used for these scans.

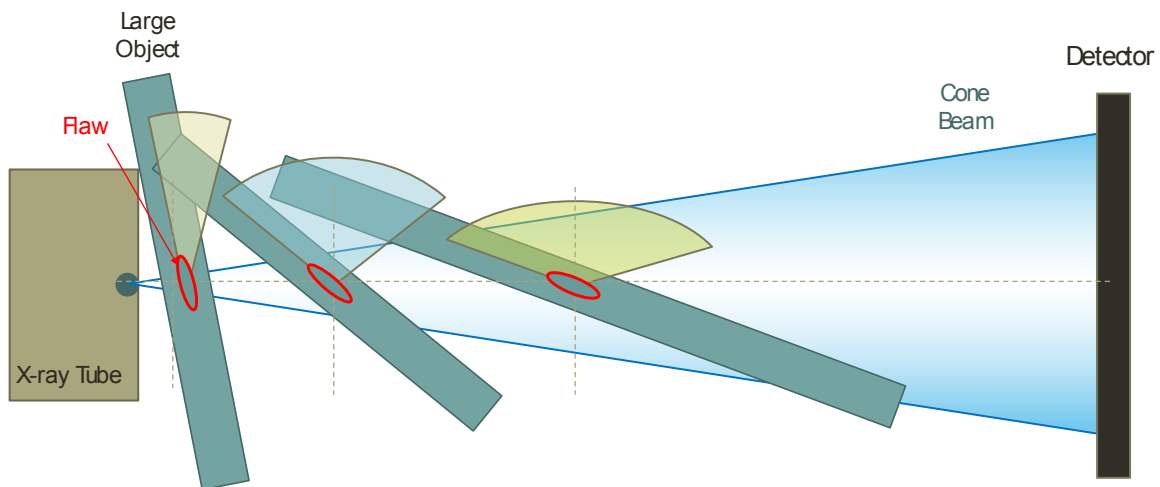


Figure 4.2.1 *Three limited angle scan setups with increasing SODs and consequently wider angular ranges.*

As proof of concept, the studies in this work were performed on relatively smaller samples. The dimensions of the flaws themselves remain fairly consistent regardless of the size of the sample. Therefore, to briefly restate one of the motivations of this work, the eventual goal is to test the feasibility of the concept toward application to scaled up composite

articles. In the event that full CT is not viable, there is no standard technique yet determined to be optimal for larger objects. One obvious option would be LAT. There have been clinical applications achieving improved quality scans by implementing rotation and translation of the source. Although the depth resolution in those medical setups are inadequate for purposes of inspecting composites, the basic concept remains an interesting option worth exploring.

Using a stationary cone-beam CT, we employed the concept of combining angular rotation and gradual translation away from the source. Since the dimensions of the object dictate the angular rotation practically achievable, there could be a SOD at which even a full 360° CT may be viable. However, using such a large SOD would severely affect the resolution of the scan. This reduction of resolution could result in loss of information regarding defects in critical areas of the inspected object. Thus, to retain high-resolution scan data as well as maximize the available angular range, several scans were chosen to be acquired at incremental distances from the source. Ideally, smaller increments in the SODs of the acquired scans would more accurately simulate the smooth translation of the tube as in the case of TS.

The various corresponding angular ranges obtained from those scans would attempt to mimic the rotation of the source. In practice, however, the computational power required to process such vast datasets limits the total number of increments. Due to this practical limitation, in this work, a total of three SODs were chosen. After all the scans are

completed, the projections of three angular range are merged together and reconstructed as the 3D image volume using FDK algorithm.

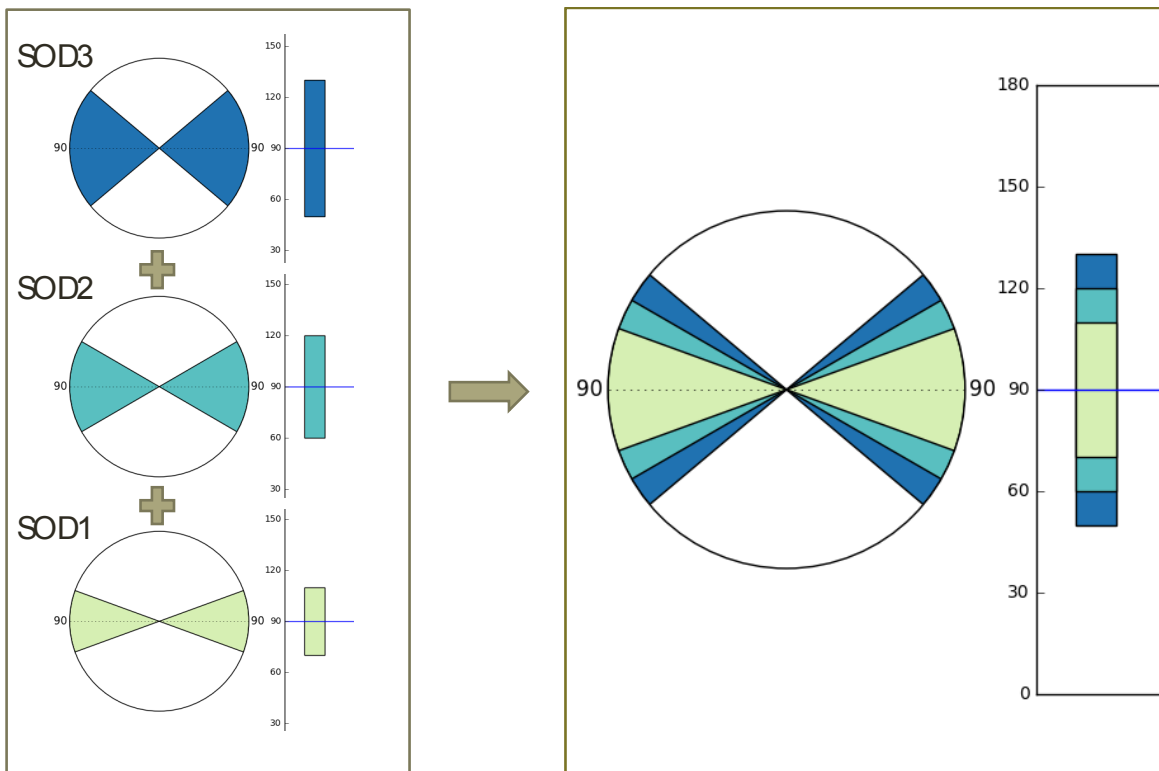


Figure 4.2.2 Scheme showing the merging of three sets of projections from different limited angle scans for further 3D reconstruction.

In **Figure 4.2.2**, a scheme is shown wherein three separate datasets were acquired at different SOD/angular ranges. These datasets were subsequently combined to reconstruct image volume. Based on initial results obtained using this protocol, it was observed that the resolution of the final summed image volume was not improved, as was originally intended. This was on account of the large number of low-resolution projections present from the wider angular range scans dominating the solution. Additionally, processing the

large datasets was computationally expensive. In order to overcome these limitations, another approach as shown in **Figure 4.2.3** was attempted.

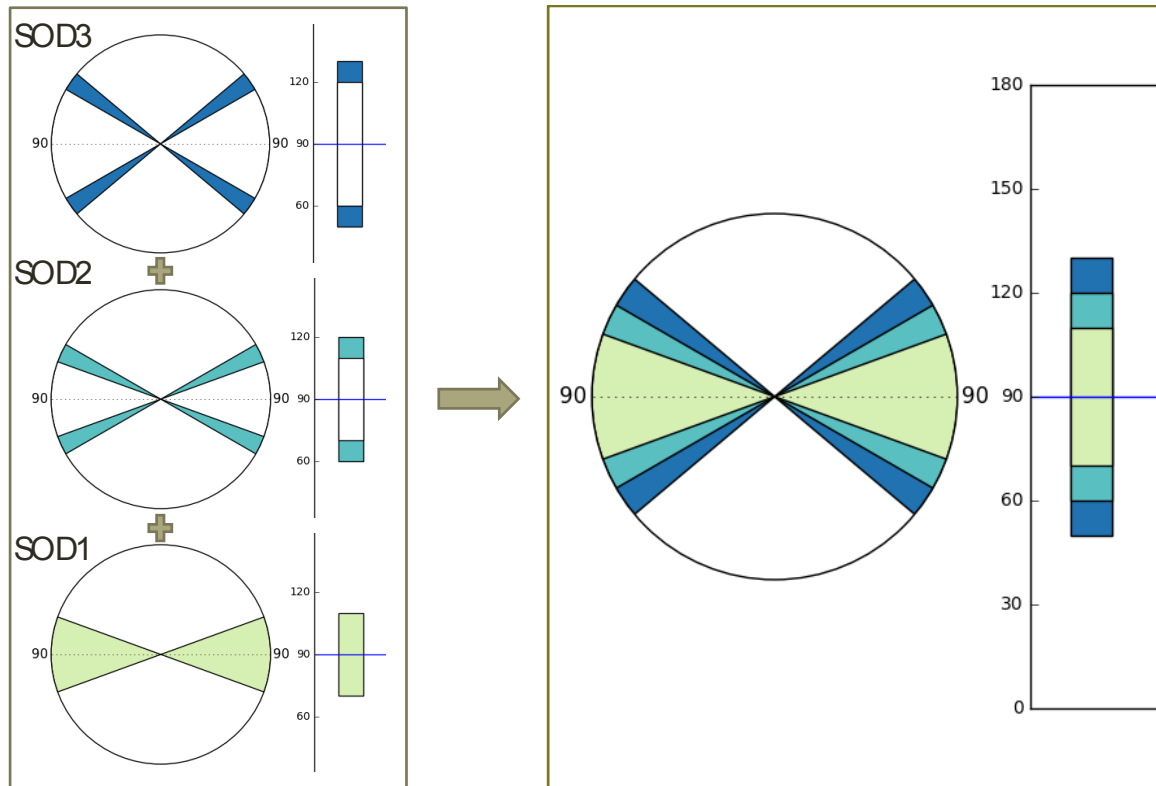


Figure 4.2.3 Scheme showing the merging of a limited angle scan with projections of the entire dataset from the high-resolution, smaller SOD scan along with complementary angular ranges of the wider angle scans.

As mentioned previously, the overall quality of the reconstruction was observed to be governed by the projections from the scans with larger SOD (where the resolution is the lowest). Therefore, the new scheme completely utilized the high-resolution scans acquired from smaller SOD while disregarding the lower resolution projections obtained from the two other higher SOD scans. This data, when used in conjunction with the higher angular

range data acquired from the larger SOD scans, should provide a less noisy, higher resolution reconstruction with the benefits of the increased depth perception offered by the latter two scans. This hypothesis proved to be right on several examples, but to have more affirmative statement further study needs to be conducted.

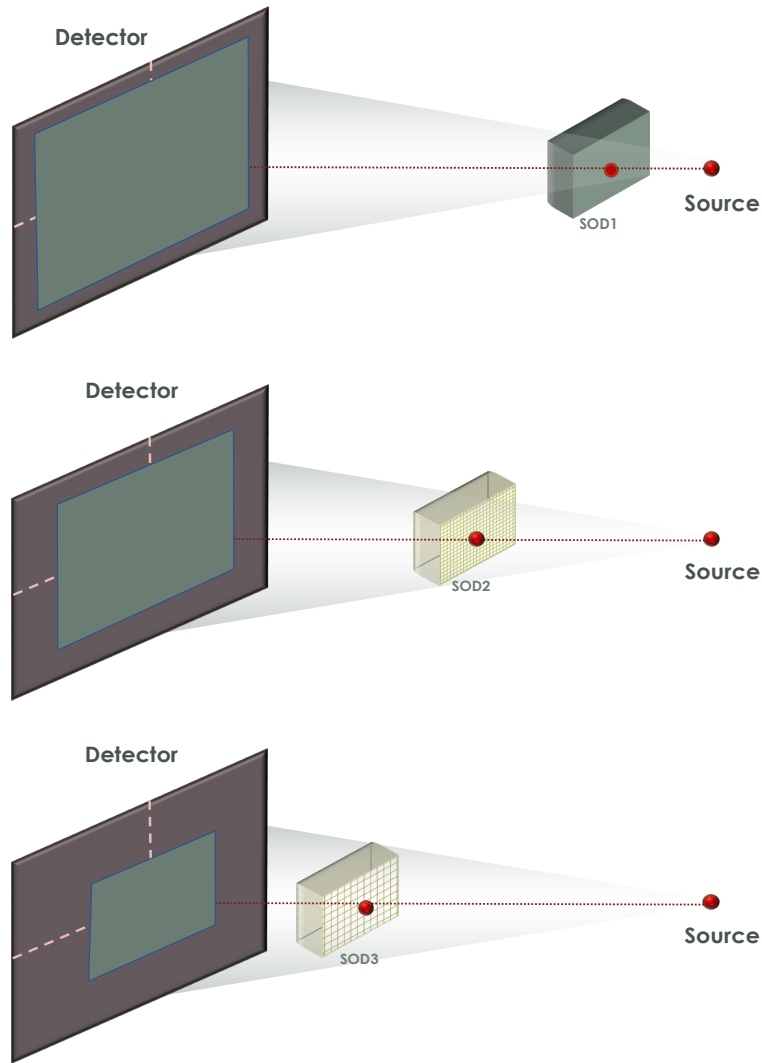


Figure 4.2.4 Schematic illustration of three scans performed at SOD1, SOD2, SOD3 and the geometric magnification obtained at those SOD values.

The geometric magnification dictates the scan resolution, which is the highest in the scan closest to the source. The schematic sketches in **Figure 4.2.4** illustrate the placement of the object with respect to detector and source as well as the influence of SOD on image magnification. The closer the part is to the detector, lower is the magnification and therefore only fewer details can be retrieved. A series of scans were performed at three SOD (200,300, 400 mm away from the source) with the same SDD (1000 mm). For sake of brevity, SODs in ascending order of distance will be referred to as SOD1, SOD2, and SOD3 respectively from time to time. This is demonstrated in the slices obtained from the respective scans shown in **Figure 4.2.5**. The scans are later scaled up to the resolution in the plane of 200 mm, where they are summed together and reconstructed. As it can be observed, the resolution of the scan decreases as the SOD increases, i.e. as the object is moved farther away from the source.

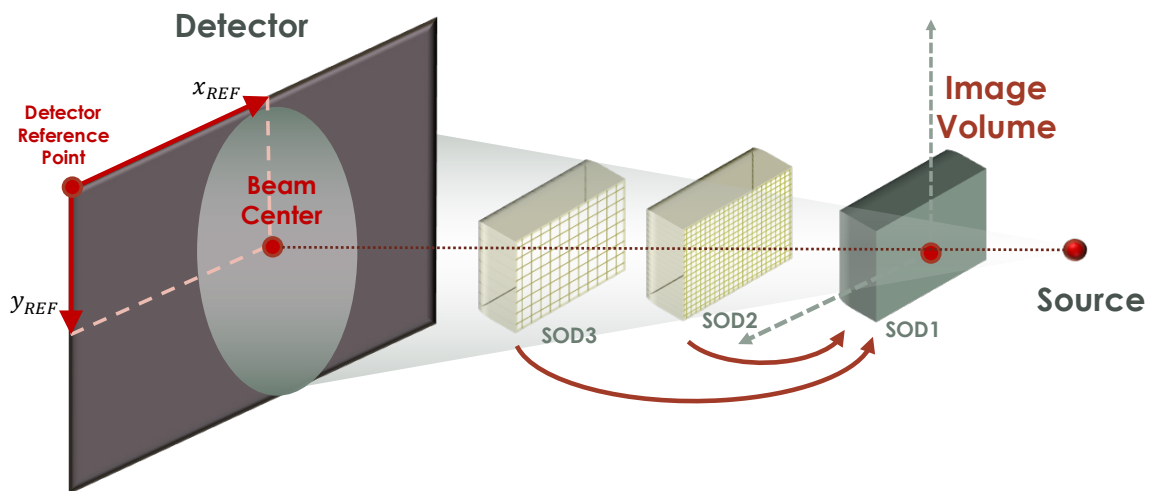


Figure 4.2.5 Projection datasets at SOD2, SOD3 and SOD1, are summed together after perspective transformation and backprojected to form an image volume.

Table 4.1 provides representative data on how the three datasets are acquired at SOD1, SOD2 and SOD3. Once the datasets are being transformed from perspective projection into the orthogonal space they can be summed together as one volume. The first scan acquired at SOD 200 mm, i.e. SOD1 is the closest to the source and has the highest resolution. Its voxel size is 0.048 mm. The optimal voxel size can be calculated by dividing the detector pixel size, which is a manufacturer's parameter and in the case of the detector used in this work is 127 μm , by the magnification ratio. Because it is essential for this problem to be able to get a highest resolution of the resultant image volume it is chosen to assign the resolution and the voxel size of the dataset at SOD1 to all three volumes. The dimensions of the image volume are described by its minimum and maximum limits in X, Y, Z directions, and its center, which remain the same for all three datasets. Resolution, defined as a number of pixels per unit length, is obtained by dividing the side length of the image volume by the voxel size.

The idea of this work is to sum the contributions of all three projection datasets together and backproject them into the chosen image volume to achieve the highest resolution possible. In order to do so, the projections should have the same resolution and the center of their volumes, from the results of the calibration step should be mapped into the volume at SOD1. It could be noted that by matching the resolution of scans at lower geometric magnification with higher one will result in pixelated images. Nevertheless, they might contain information from the wider angular range, which could not be obtained at a closer distance.

Table 4.1 Example of projection dataset parameters when mapped into the image volume

SOD 200 mm

		X	Y	Z
VOXEL	mm	0.048	0.048	0.048
MIN	mm	-1.94	-6.80	4.04
MAX	mm	18.70	8.08	13.16
CENTER	mm	8.38	0.64	8.60
RESOLUTION	pixel/mm	430	310	190

SOD 300 mm

Original Parameters

VOXEL	mm	0.108	0.108	0.108
CENTER	mm	8.38	0.64	8.60
RESOLUTION	pixel/mm	191	138	84

Converted Parameters

$(200/300)^2 * 0.108 = 0.048$

VOXEL	mm	0.048	0.048	0.048
CENTER	mm	8.38	0.64	8.60
RESOLUTION	pixel/mm	430	310	190

SOD 400 mm

Original Parameters

VOXEL	mm	0.192	0.192	0.192
CENTER	mm	8.38	0.64	8.60
RESOLUTION	pixel/mm	108	78	48

Converted Parameters

$(200/400)^2 * 0.192 = 0.048$

VOXEL	mm	0.048	0.048	0.048
CENTER	mm	8.38	0.64	8.60
RESOLUTION	pixel/mm	430	310	190

Each scan was described by the distances between the axis of rotation, X-ray source and detector, the consequent resolution of the scan and its sharpness. All this information was transformed from perspective to orthogonal space and projected into the image volume with highest resolution. The effective voxel size of the closest scan was set to be the same for all three scans. The distances were converted to the ones used for the closest scan to facilitate the backprojection operation of all three projection sets into the same image volume. The fact that the scanned object was not shifted and had the same starting angular position for all three scans made it possible to add all projections together and reconstruct a merged dataset as if they were all acquired in one instance. **Figure 4.2.6** illustrates the reduction of resolution with increasing SOD.

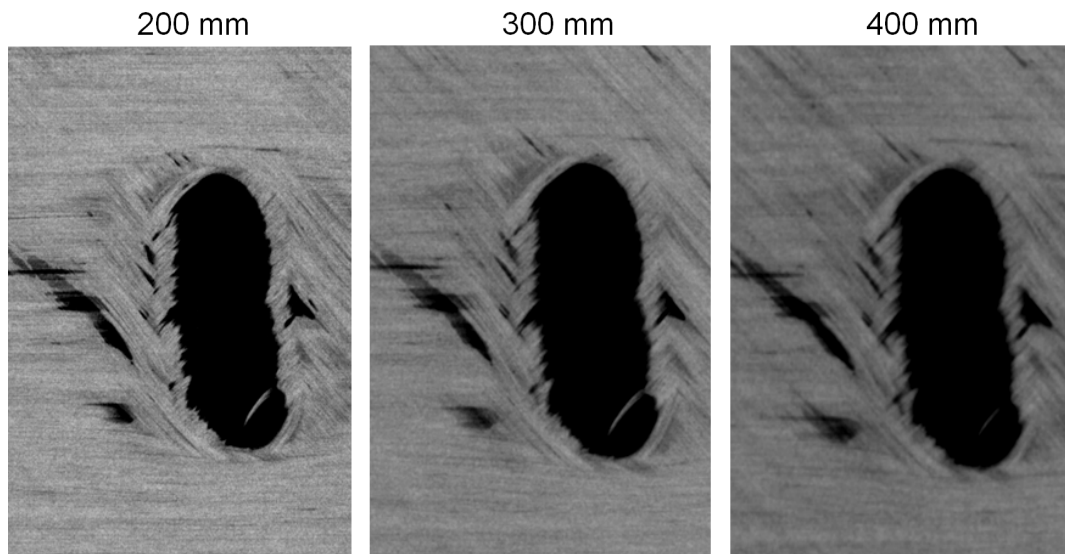


Figure 4.2.6 In-plane slices of the void obtained from reconstructed volumes scanned at SOD of 200, 300, and 400 mm respectively.

X-ray source generates a cone-shaped beam, which illuminates the object on the rotary stage and projects the image into the digital detector. The position of the rotary stage is a critical parameter of the scan that needs to be known with high precision for the success of the reconstruction. The North Star recommends performing a 3D calibration which determines the true geometry of where all components of the system were located during the scan acquisition. In particular, this procedure finds the beam center, which refers to the projection of the beam source into the detector. The beam center does not coincide with the physical center of the detector and is required to be determined for each scan, because it depends on many factors, including the beam energy, beam take-off angle from the source and the alignment of the source and detector. As a result of 3D calibration, the axis of the stage rotation is defined by a spatial vector with an offset from the original readings during scan setup.

The projection of the beam center is described by coordinates from the top left corner of the detector. In this work the developed algorithm realizes it in the following way. In order to locate the beam center on the detector, the imaginary line between the source and the center of the rotary stage gets extended till it intercepts with the detector at a point. It was observed that the vertical misalignment of the source relative to the center of the detector results in a large scatter among the resulting source-to-detector distance as well as the vertical reference coordinate of the beam center, output by the calibration procedure.

Table 4.2 Example of the original distances, set by operator, and calibrated distances.

<i>Original Distances, mm</i>			<i>Distances after 3D Calibration, mm</i>			
Source to Object Distance	Object to Detector Distance	Source to Detector Distance	Source to Object Distance	Object to Detector Distance	Source to Detector Distance	Zoom
100	800	900	90.5	811.0	901.5	x9.96
150	750	900	148.0	756.9	904.9	x6.11
200	700	900	198.8	712.7	911.5	x4.58
300	600	900	298.4	613.0	911.4	x3.05

Table 4.2 lists the distances readings from the system components before the scan and after the calibration procedure. Data for the table was obtained from a set of scans of the void in a Glass/Epoxy composite structure, at four different distances away from the source. All scans were acquired at the same Source-To Detector Distance (SDD) set up by the operator as 900 mm. The large discrepancy in the location of the object and its axis of rotation resulted in variance of the calibrated source-to-detector distance, which varied for all the four cases from 901.5 to 911.4 mm and in reality remained constant for all four scans. Figure 4.2.7 illustrates the issue arising when calibrating for scans at different magnification. The resultant SDD forces Y-shift in the beam center which needs to be adjusted before merging projection datasets.

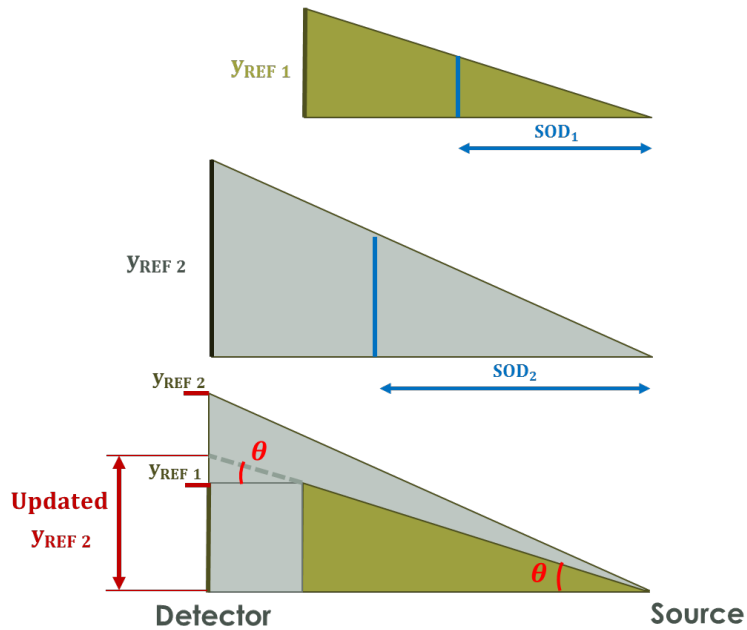


Figure 4.2.7 Calibration results from scans at different magnification need to be adjusted before summed altogether.

Although this effect does not play a role in the process of 3D reconstruction, the tomosynthesis method implemented in this work proved to be extremely sensitive to this change. The merged projection datasets, collected at different source-to-object distances, resulted in doubling artifact in the reconstructed image volume (**Figure 4.2.8**). That occurred due to the fact that the beam center was projected to a different detector plane and its vertical component was shifting upward with the increase of the source-to detector distance.

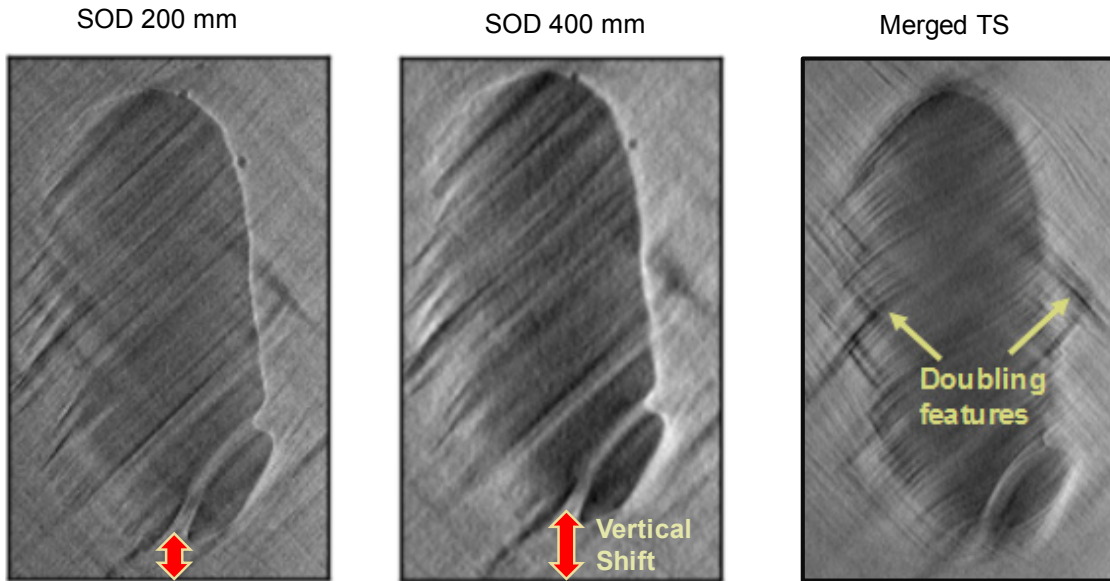


Figure 4.2.8 Unaccounted for vertical shift in calibration report, resulted in doubling artifacts in merged reconstructed tomosynthesis volume.

4.3 Acquisition technique

4.3.1 Influence of Scan Acquisition Parameters

The most common composite structural elements in aerospace applications are large-sized planar objects.¹⁷ The CT inspection of these parts is complicated due to two main problems: the risk of collision with X-ray source at high magnification and poor penetrability in longitudinal direction.¹⁷ That makes it challenging to detect some manufacturing and in-service defects, which are typical and very dangerous for composites.

In this chapter, a flat composite object with planar defects will be explored in greater detail. The challenges of finding an appropriate scanning technique will be demonstrated

on the example of a Carbon/Epoxy panel with impact damage, characterized by multiple delaminations and matrix cracks –a very critical set of defects for any composite structure, strongly correlated to its life and performance.⁴

Panels represent a special class of high aspect ratio objects, particularly challenging for CT inspection.⁴⁸ Generally, in order to get a good quality CT scan, one needs to have a good penetration of the object at every angle of 360° range.¹⁷ In the case of panels, often the in-plane dimensions could be orders of magnitude larger than the thickness. As a result, of there is a significant disparity between the X-ray beam energy required to traverse through a greater volume of material in the length and width direction, as opposed to the thickness.¹⁷

The idea of tomography is to discretize the scanned volume into a finite number of 3D pixels (voxels) and to find how every voxel attenuates certain level of energy. Therefore, it is imperative to set a constant value of energy throughout the scan. If the energy will be varied in each angular direction the voxel will respond differently to each energy level.⁴⁹ It complicates the problem of determining its true value. Moreover, the increase of X-ray beam energy demand will up the heating of the target.⁵⁰ The consequent increase the focal spot size will affect the size of the voxel in reconstructed image volume, directly related to the scan resolution. Numerous researchers have approached the study of combining information from sets of projections, acquired using different penetration energies. This technique is commonly referred to as dual-energy scanning.⁵¹ In addition to the scanning methods, a lot of research is devoted to advancing reconstruction algorithms,⁵¹ which

could account for the different energies and merge this information into a final volume. Although not implemented in this work, it is worth recognizing the potential benefit of this technique. Meanwhile, the commercial CT systems use a constant energy for the scanning procedure.

Consequently, in practice, during the scan acquisition a fixed X-ray energy has to penetrate through very different path lengths: while it easily penetrates through the thickness, the strong attenuation along the widest dimension of the panel can cause photon starvation in respective angular directions.

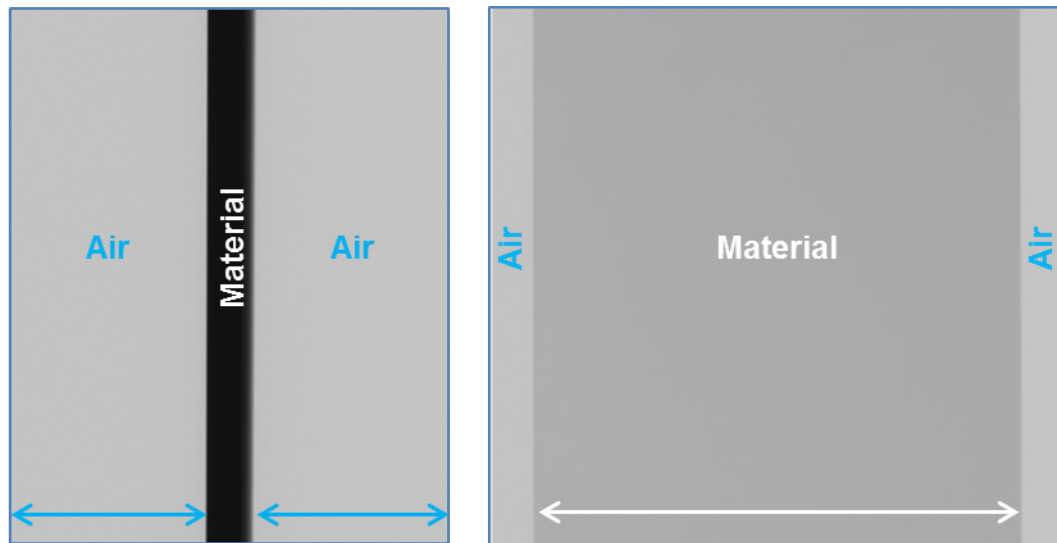


Figure 4.3.1 Examples of two X-ray radiographs of the plat acquired at the same beam energy (a) 0° side view; (b) 90° frontal view.

To further illustrate the relation of beam energy to the material density in a given direction, consider **Figure 4.3.1**, which shows two radiographs of the same planar object acquired at different angular viewpoints. Figure 4.3.1a corresponds to the side view of the panel at 0°

and Figure 4.3.1a shows the frontal view at 90°. In the figure, the darker areas represent regions of higher density. In order to compare the readings of greyscale values through the object, the linear attenuation coefficient⁴⁰ μl can be introduced. This coefficient¹⁹ is defined as follows:

$$\mu l = \ln\left(\frac{I_{air}}{I_{mat}}\right) \quad (4.6)$$

where I_{air} and I_{mat} are intensities of air and material respectively.

Comparing the two coefficients from Figure 4.3.1 it is apparent that the same object has almost 10 times higher attenuation through the width rather than through the narrow direction.

The strength of the beam, its ability to punch through the material is primarily defined by the parameter kV.¹⁶ (To avoid confusion, in the following work the term kV will be used to refer to accelerating voltage). By increasing the kV, the penetration of the object increases, while the intensity in the surrounding air reaches saturation level, which is undesirable. The final technique is usually decided for each part specifically to find a compromise between these two conflicting parameters: object penetration and air saturation. The penetrability of the object is commonly judged by the darkest grey scale intensity values present in the radiograph. This factor alone, however, does not entirely determine the quality of the scan. For instance, different combinations of kV, μA , and exposure (fps) could produce the similar greyscale intensity values, yet resultant

reconstruction quality may significantly vary and not guarantee the detection of certain features in the object.

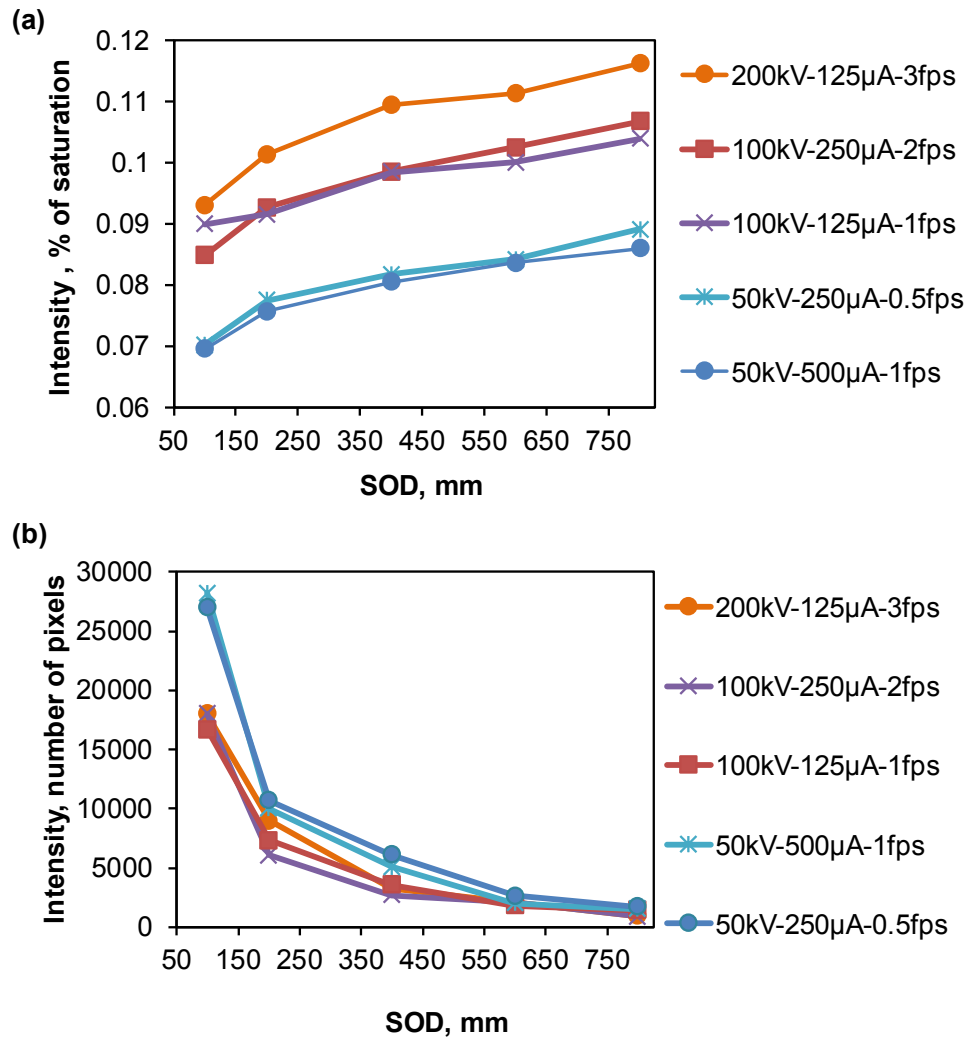


Figure 4.3.2 Dependence of greyscale intensity values through the material on the SOD and penetration power in (a) % of saturation, (b) number of pixels.

Figure 4.3.2a shows the dependence of material greyscale intensities through the widest plate dimension in the 0° direction, acquired at different SOD and penetration power

values. It can be observed that as the kV value is increased, there is a greater penetration through the material. Additionally, the intensities gradually rise as the SOD values increase, given that the source-to-detector distance remains constant. This could be explained by the scattering of the X-ray photons off the edge of the object. This is not observed in the 90° view of the radiograph. The greyscale values in the 90° view do not vary with changing SOD. The figure also demonstrates that the kV parameter is the dominant factor with regard to penetration ability of the beam.

When comparing the intensity values in terms of number of pixels versus the SOD and different penetration powers, Figure 4.3.2b, it can be seen that there is a steep decline in the flux of the beam with increased in SOD on account of the fewer photons captured by the detector. At relatively higher SODs, however, the disparity between the amounts of photons received at the detector becomes insignificant for different beam kV values. The trends seen in Figures 4.3.2a and b, suggest that these factors need to be taken into consideration when setting up the technique parameters for the scan acquisition, as it can result in different quality of reconstructed data.

The scan acquisition parameters explored in this section and their influence on the quality of reconstructed image volume will be further considered in consequent sections when developing the experimental technique appropriate for composite planar structures.

4.3.2 Development of Experimental Technique

For the purpose of validating the technique parameters of CT scan and tomosynthesis scans for the carbon/epoxy impact plate, it was decided to fabricate a composite specimen with a flaw of precisely known shape and location. The sample was made using IM6/8552 carbon/Epoxy prepreg material and cured at 350° F. The 16-ply part was 10 x 10 in with a $[90/0]_{4s}$ layup. Several flat defects in the form of pieces of cured epoxy were placed between some middle plies. The idea was to create such defects, so that they would resemble areas of delamination in real-life structures. The inserted pieces of epoxy were cured prior to the layup of this plate, so during the curing process to create ply-interface discontinuity. **Figure 4.3.3** shows the actual plate at the stage of layup. A relatively larger flat layer and a thicker piece of precured epoxy were placed between the plies to simulate discontinuity with density contrast representative of a manufacturing defect.



Figure 4.3.3 *Insertion of cured epoxy in the layup of the carbon/epoxy plate to produce a discontinuity defect, resembling delamination.*

The **Figure 4.3.4** shows a 2D X-ray radiograph of the cured plate. The voluminous piece of cured epoxy inserted on the lower right resulted in a small void and some matrix cracks around it. The flat piece of epoxy did not cause any internal shape deformation and is not noticeable on the image due to its close density to carbon fibers and epoxy in the plies itself.

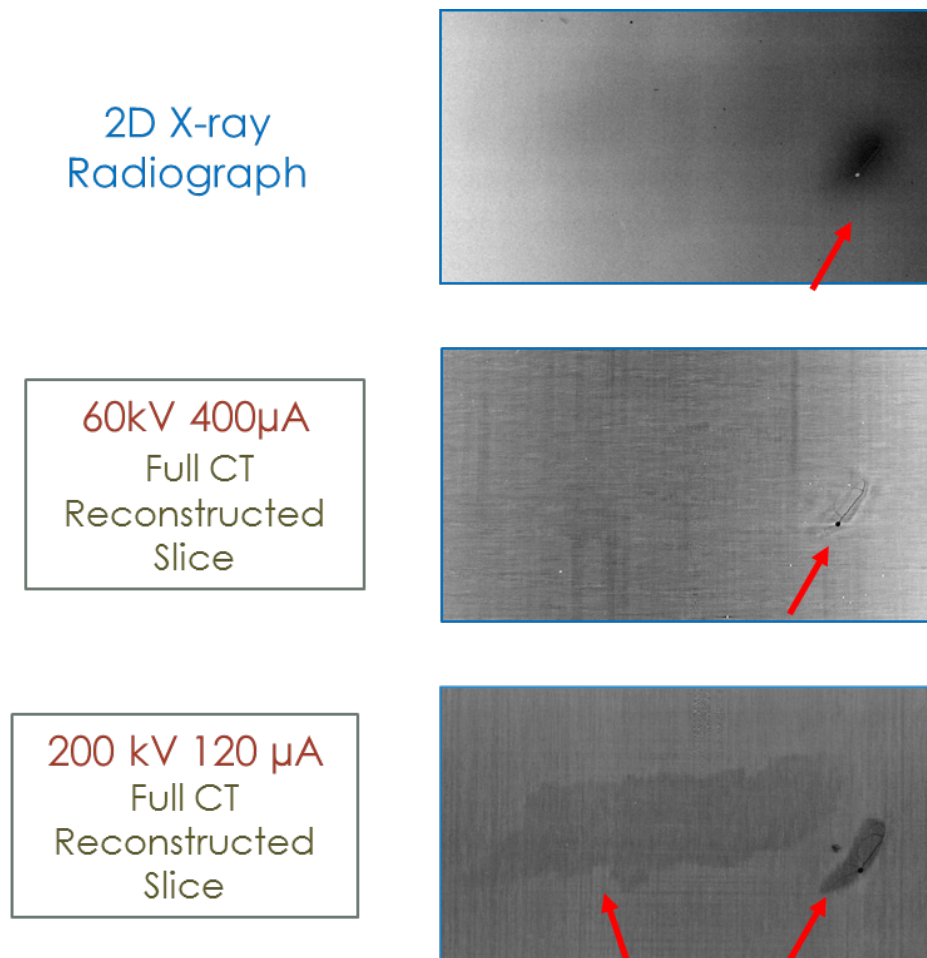


Figure 4.3.4 Comparison of 2D X-ray radiograph of the plate and two reconstructed slices acquired at different beam energy levels. The flat piece of epoxy is not visible in the 60 kV scan, however is clearly apparent when acquired at 200 kV.

When scanned at 60 kV, 400 μ A, due to the high influx of photons, one can expect to see good image contrast, making this technique suitable for scanning composites. During this particular scan setup, the typical greyscale value requirements for adequate penetration and contrast were met. However, based on the reconstructed volume, the presence of the thin layer of epoxy between the plies was not detected using these parameters. Thus, the relatively low penetration power was not apparent from the greyscale values of the 2D radiograph.

On the other hand, by using a higher kV, 200 kV in this instance, the greater penetration power ensured the clear visibility of the epoxy film within the plies. This is despite the scan having only a third of the μ A (the parameter representative of the number of photons and scan contrast) as compared to the 60 kV scan previously discussed. These results provided insight into the influence of the technique parameters, particularly kV, on the scan reconstruction quality and therefore the detectability of flat defects. The influence of kV was therefore further investigated on the Carbon/Epoxy plate specimen. Briefly, the plate specimen was subjected to an impact load prior to scanning, which resulted in the formation of matrix cracks and delaminations which were not visible on the surface.

CHAPTER 5

RESULTS

5. Results

5.1 Limited Angle Tomography (LAT)

Figure 5.1.1 illustrates the limited angle scan with the highest possible resolution, considering the size of the flaw present in the inspected structure. As evident from the sketch, when the part is placed this close to the X-ray source, the scanning angle range is obstructed by the geometry of the tube. Essentially, the closer the object gets to the tube, smaller the angle range that can be acquired. In this work, it is sought to enhance the LAT technique by acquiring a series of LAT scans at several distances away from the source. This will facilitate the advantage of scanning at a very low distance from the source but for small angle and gradually moving the object away from the source to collect wider angular range at a farther distance.

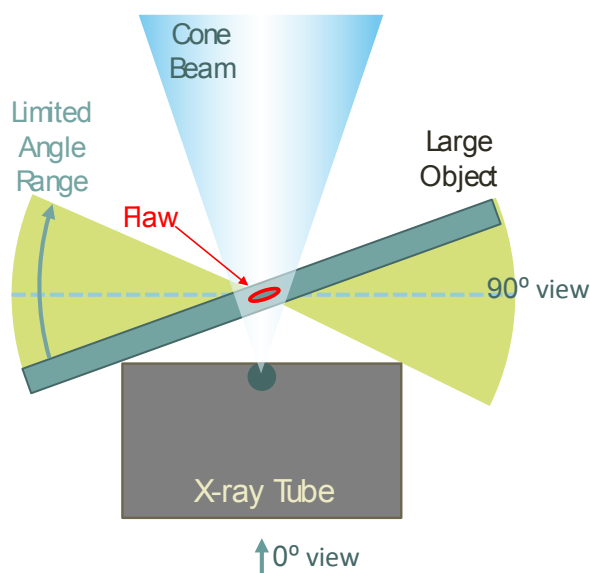


Figure 5.1.1 Limited angle tomography setup. Maximum angular range of the scan is dictated by flaw size and SOD.

The first scan parameter typically determined is the minimum possible SOD as it defines the highest resolution achievable. The appropriate choice for the value of SOD is informed by several variables, namely: the overall size of the part, the size of the inspected flaw, the obstructing geometry of the tube. The closest SOD and the corresponding angular range of the scan are determined by the geometry of the scanned object and the dimensions of the x-ray tube. **Figure 5.1.2** shows a schematic of the LAT setup and the geometric relationship between SOD and angular range α .

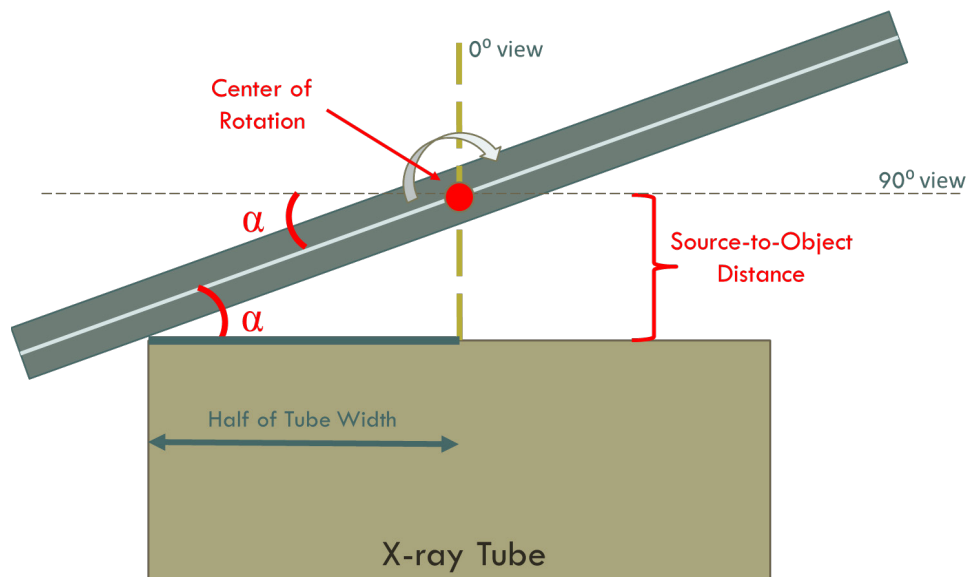


Figure 5.1.2 Limited angle tomography setup showing geometric relationship between SOD and angular range α .

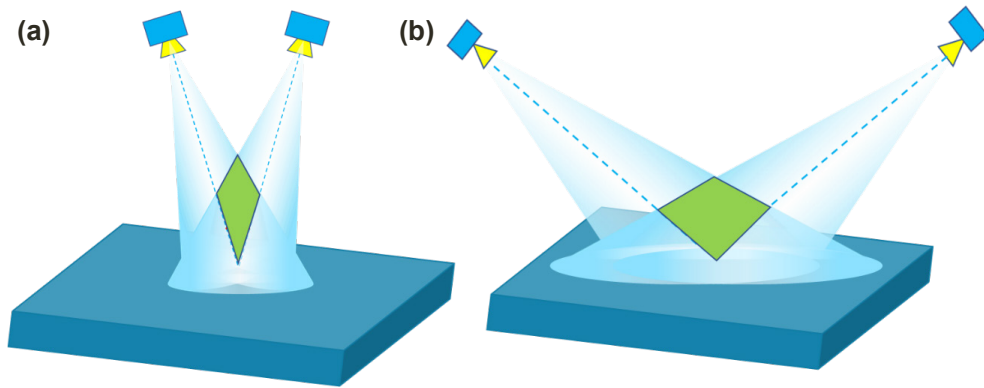


Figure 5.1.3 Formation of depth artifact dependent on the tilt angle

Detection and measurements of certain singularities present in the object of inspection can be quite challenging in LAT scans as opposed to full CT. Nevertheless, certain image artifacts can help indicate their presence and relative 3D location. For instance, the appearance of streaking artifacts can indicate the existence of singularities such as high density inclusions or areas of low density such as resin pockets and voids. These streaking lines appear tangential to the boundary of the flaws. **Figure 5.1.3** illustrates the how the smaller acquisition angle (Figure 5.1.3a) causes the through-depth artifacts to appear more elongated in the reconstructed volume than the larger tilt angle (Figure 5.1.3b). This phenomenon can lead to overprediction of the depth measurement of the inspected features.

An attempt was made to further investigate the shape deterioration and the streaking artifacts occurring in LAT scans as a function of acquisition angle. A 3D volume phantom of 201x201x201 pixel size with a central dense area of 60x80x80 pixels was created to

serve as a model to simulate an inclusion in a real volume and demonstrate the effect of decreasing LAT angle on its appearance in the reconstructed slice. The model assumed a cone beam angle of 30° , SOD and SDD of 700 mm and 900 mm respectively. FDK algorithm was used for image reconstruction. The acquisition angle was in the plane perpendicular to the cone beam. This comparative study can be seen in **Figure 5.1.4**.

The figure shows the through-depth slice of volumes reconstructed from different LAT angular ranges. The reproduced shapes in Figure 5.1.4 begin to rapidly deteriorate as the scan angles decrease due to the limited angular coverage causing gaps in the collected projection dataset. Given how well defined the bounding surfaces on the top and bottom of the simulated inclusion are, we get fair indication of its accurate location within the object, even without having access to the original phantom image for reference. However, the width of the reconstruction become almost indecipherable at angles below LAT 100° , especially in the absence of prior knowledge of the shape. Comparing the LAT to the original image, it can be assumed that the inclusion inscribed within the shape bounded by the streaking lines.

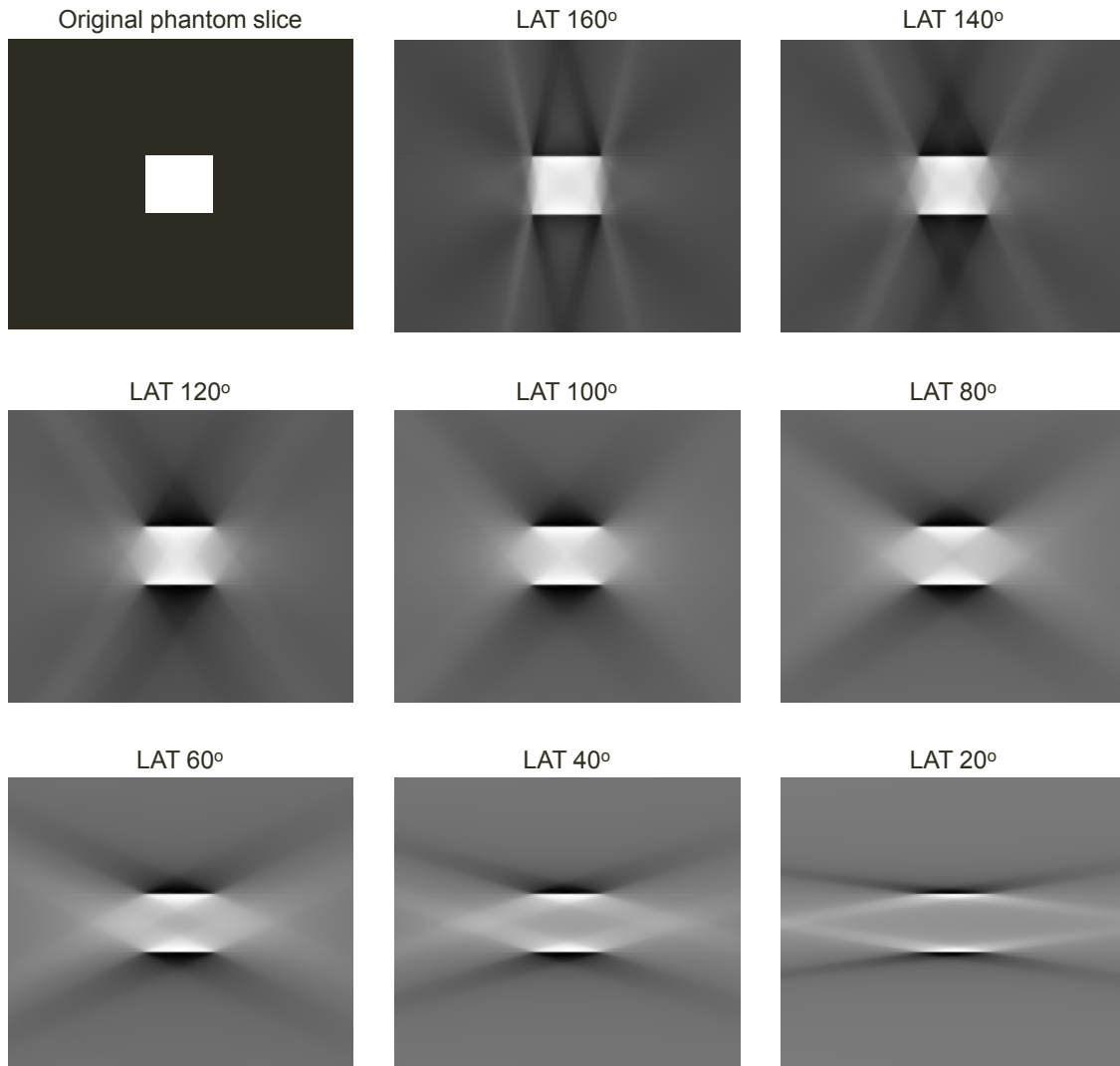


Figure 5.1.4 Comparison of the original phantom slice and the shape deterioration and depth artifact creation with decreasing LAT scan angles.

The regions of overlap between the white streaks give a misleading impression regarding the density of those regions. Since the greyscale intensities indicate relative density (in this case whiter meaning denser; darker suggests lighter), those regions give a false illusion of actual density at that location. As an extreme example, the LAT 20°, the region of the inclusion appears completely washed out, with the greyscale intensity included in that

region appearing similar to that of air, thus providing no real indication of the inclusion's presence. Correspondingly, the angular ranges from 140° to 40° , all show the appearance of a dark shadowy regions above and below the simulated inclusion. This could cause the masking of information that could be present in the object, at those locations. **Appendix C** shows an example of how the combination of defects' positioning and acquisition angular range can produce misleading artifacts in image reconstruction volume.

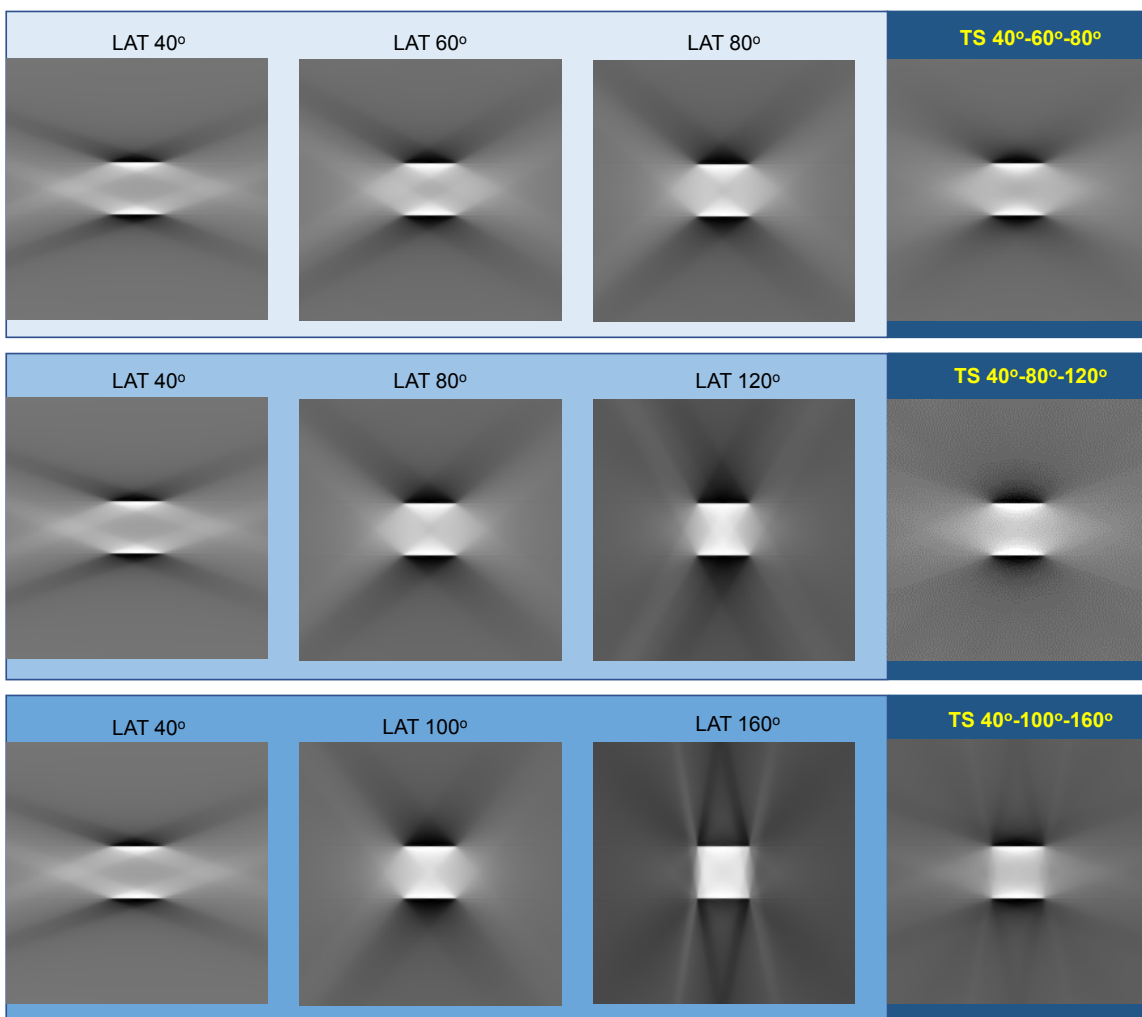


Figure 5.1.5 Simulation of TS concept on phantom image volume

Using the original phantom described above, the application of the concept of TS is now illustrated in **Figure 5.1.5**. Three cases are demonstrated in the figure, namely TS 40°-60°-80°, 40°-80°-120°, and 40°-100°-160°. TS was simulated by combining three sets of projections at different angular ranges that were subsequently reconstructed to form an image volume, a slice of which is demonstrated in the figure. It can be observed that the characteristic streaks of LAT remain are greatly diminished when merged to form the TS slice.

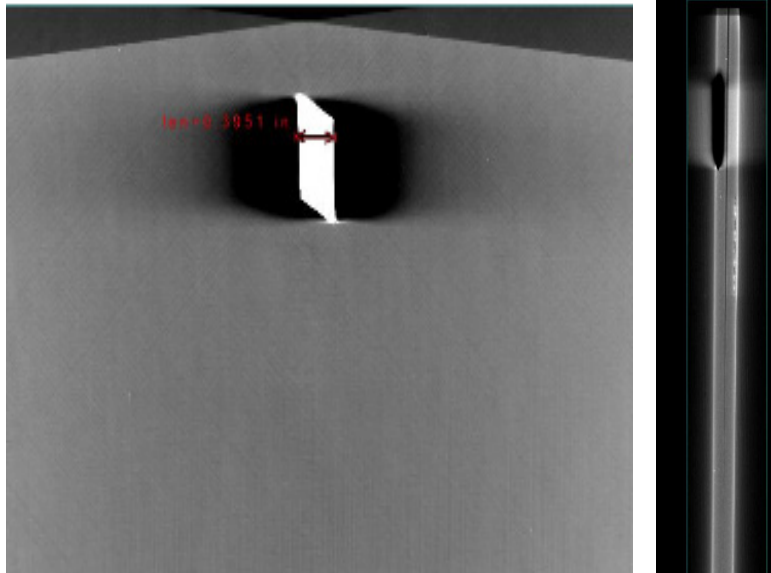


Figure 5.1.6 *Representative reconstructed slice showing shadow artifacts produced around the metal inclusion in composite plate.*

There is another instance where shadowing (as seen previously in case of the LAT scans of the phantom) can cause challenges for defect detection. This often occurs in the case of assemblies where both metals and composites are present, due to the difference in respective densities, a similar shadowing effect can occur in the angular ranges of poor penetrability. **Figure 5.1.6** shows an example of such a case where the presence of metal

within the composite creates a shadow artifact making it impossible to inspect the immediate region around it. Those regions tend to be the critical areas of the composites since they endure damage during assembly and experience fatigue, especially in the case of fastened joints and need a thorough inspection.

5.2 Impact Damage in Laminated Composite

5.2.1 Case Study 1: Impact Damage in 12-Ply Carbon/Epoxy Plate

Thin 12-ply $[0^\circ/90^\circ]_{3S}$ Carbon/Epoxy plate (thickness of 0.08 inch (2mm)) displayed in **Figure 5.2.1** was subjected to impact load. There is a visible surface crack at the location of impact on the plate (seen within the region marked by the red circle in the figure). The plate size of $\sim 5 \times 6$ inch makes it difficult to achieve high magnification in the full-range scan. Given the limited scan angle possible in this case, this study was used to explore the application of limited-angle tomography algorithms to detect the small internal details of this high-aspect ratio structure.

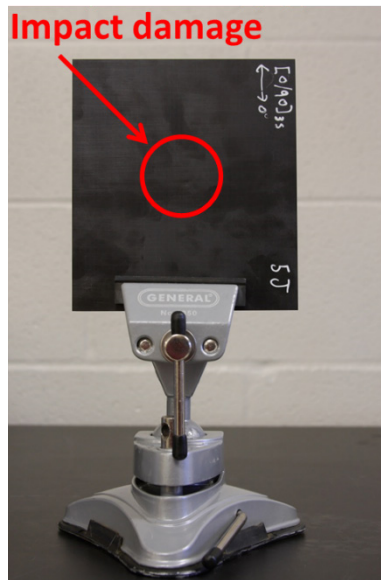


Figure 5.2.1 The thin 12-ply $[0^\circ/90^\circ]_{3S}$ Carbon/Epoxy plate specimen with location of impact marked with red circle

Again all LAT results were compared with full 360° scan reconstruction. The parameters of the full and LAT scans are provided in Table 5.1. The full scan demonstrates the

damage that occurred in the part due to impact: through-the-thickness matrix cracks and delaminations between the plies.

Table 5.1. Scan Parameters for Carbon/Epoxy Plate.

12-Ply Carbon/Epoxy Plate	Full scan 360° range	LAT Scan 90° range
Tube voltage, kV	40	40
Target current, μA	600	600
Speed, frame/sec	0.7	0.5
Magnification	13.38x	19.84x
Voxel resolution	0.37×10^{-3} inch (9.5 μm)	0.25×10^{-3} inch (6.4 μm)
Step, degrees	0.25	0.25
Number of projections	1440	360

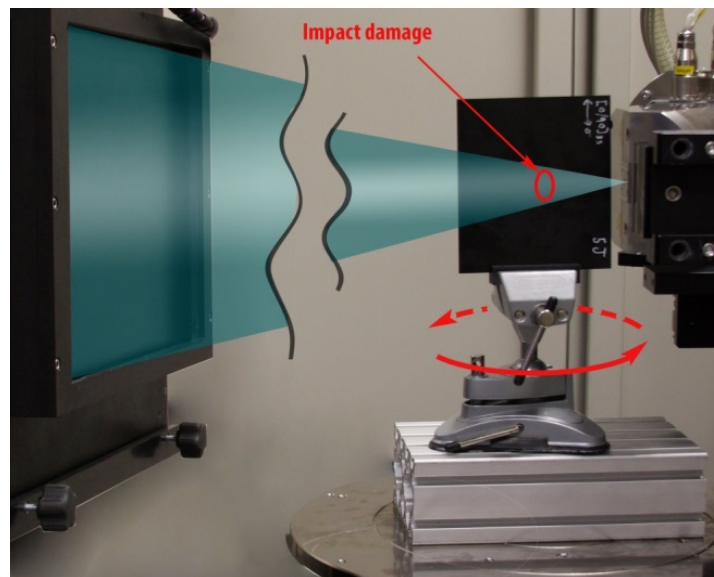


Figure 5.2.2. Area of interest in the center part of the plate.

Large plate dimensions lead to lower magnification of the impacted area scan, which results in decreased level of detail. An angular range α (see **Figure 5.2.2**) for the LAT

scan that is smaller than 180° enables closer placement of the plate to the X-ray source. Using LAT reconstruction it is possible to increase geometric magnification while maintaining the quality of reconstruction.

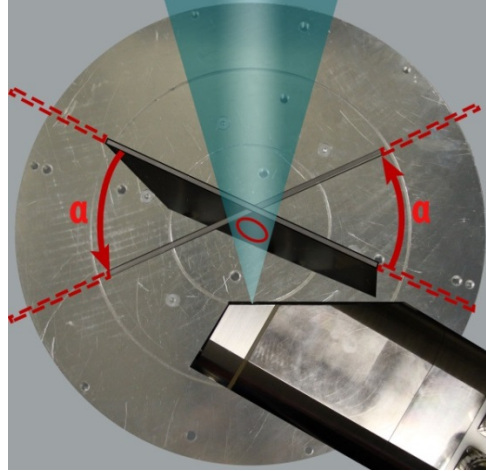


Figure 5.2.3 Specimen rotation in the angular range α was examined.

Figure 5.2.4 shows reconstructed 3D volume of the scanned area with impact damage. It was observed that once the angular range becomes less than 180° , ply delaminations and 90-degree matrix cracks become undetectable. The more the angular range decreases the more difficult it is to interpret the geometric dimensions. For example, the 3D volume reconstructed from the 160° angular range does not show 90-degree matrix cracks and delaminations while the zero-degree cracks are consistent with the full-range scan. At the 60° angular range distortions in the 90-degree direction become prevalent; zero-degree matrix cracks are still visible but identification of their through-the-thickness location is difficult.

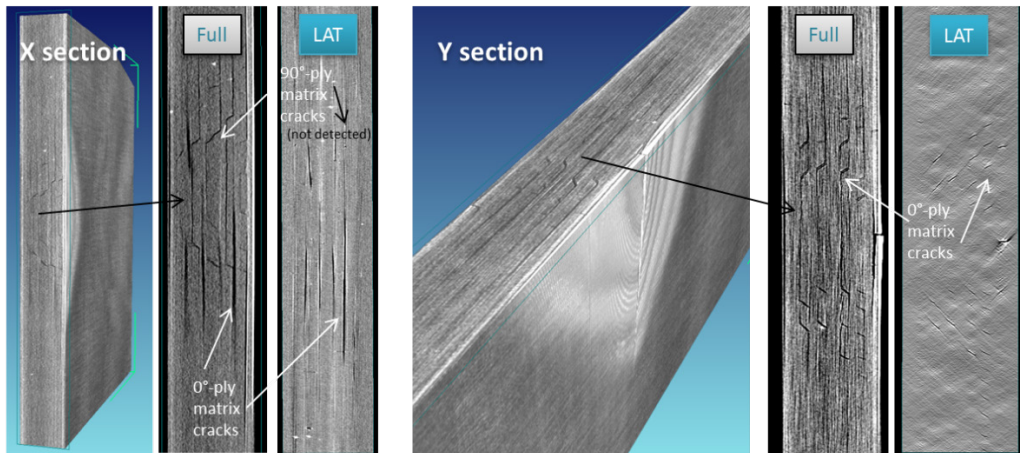


Figure 5.2.4 X/Y-section views for the full and LAT scans of the plate with impact damage.

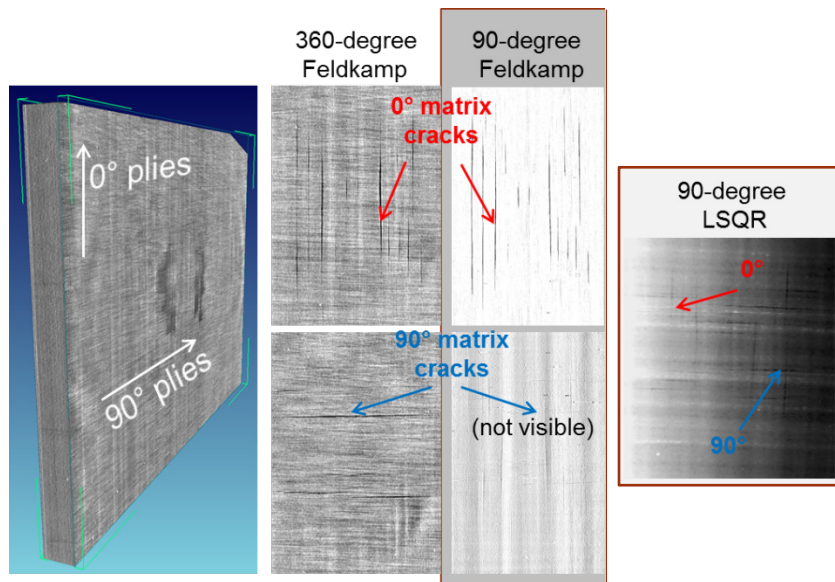


Figure 5.2.5 Reconstructed 3D volume and through-the-thickness section views of 12-Ply Carbon/Epoxy plate using full-range and LAT scans.

Based on these observations it was decided to perform an actual 90° LAT scan. The plate was positioned as shown in **Figure 5.2.5**. Geometric magnification of the new LAT scan was 19.8X, which was 1.46 times higher than the full 360° scan and the 3D reconstruction of the specimen had pixel resolution of approximately 0.25×10^{-3} inch. The radiographs of the LAT scan contained significantly more noise, as compared with the full scan. The noise pattern consisted primarily of contrasting vertical and horizontal lines. Comparison of the full-range and 90° LAT scans by LSQR (damping of 1.0) algorithm summarized as follows:

Zero-matrix cracks are identified by all LAT reconstructions. 90-degree matrix crack are not detectable by Feldkamp algorithm but detectable by LSQR algorithm. Solution by LSQR has more contrast artifacts making 90-degree cracks harder to identify. Contrasting vertical artifacts are observed in LAT scans. We conclude that this case presents a challenge for 90° LAT scan; however, stochastic algorithms demonstrate improved solution quality as compared with the solution by analytical methods.

5.2.2 Case Study 2: Impact Damage in 24 ply IM7/PMT-F3GHT Carbon/Epoxy Plate

The IM7/PMT-F3GHT Carbon/Epoxy plate of 24 plies with $[45^\circ/90^\circ/-45^\circ/0^\circ]_{3s}$ layup was subjected to a localized impact load prior to scanning (**Figure 5.2.6**). The detailed parameters of scanning technique are provided in **Table 5.2**.

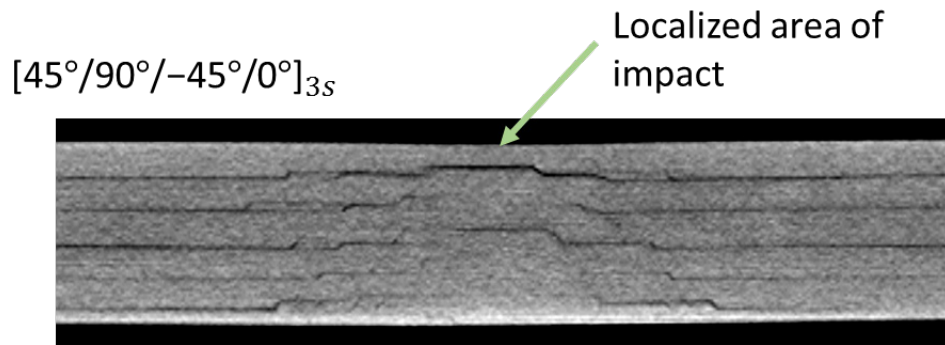


Figure 5.2.6 Impact plate subjected to localized impact load

Table 5.2. Scan Parameters for IM7/PMT-F3GHT Carbon/Epoxy plate

IM7/PMT-F3GHT Carbon/Epoxy plate	Full scan SOD 150 mm	Full scan SOD 250 mm	Full scan SOD 350 mm
Tube voltage, kV	200	200	200
Target current, μA	125	125	125
Speed, frame/sec	3	3	3
Magnification	5.71x	3.45x	2.47x
Voxel resolution	22.2 μm	36.8 μm	51.5 μm
Step, degrees	0.25	0.25	0.25

The dimensions of the plate were appropriate to allow a high-resolution CT with 360° scan range. The full CT was assumed to be the truest representation of the sample and used as the benchmark for further comparison of the LAT scans implementing different reconstruction algorithms. According to the information obtained from the full CT, cracks and delaminations were observed clearly in every ply although as mentioned previously, no external damage was visible on the plate surface. The plate sample used in this work was assumed to be of infinite dimensions (although this was not truly the case) in order to simulate the technique toward real-life large aerospace flat parts.

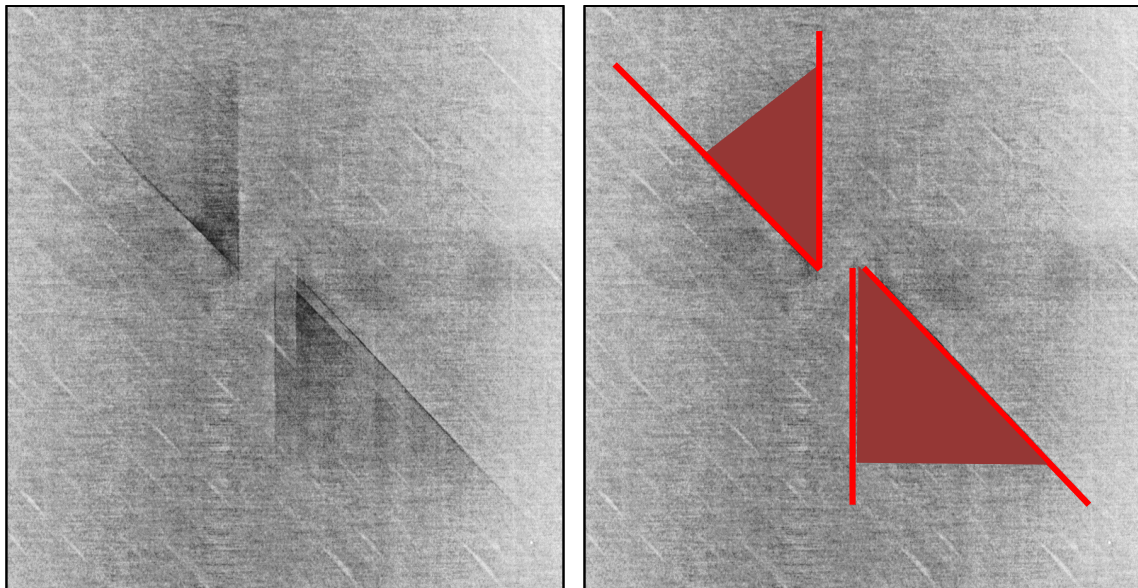


Figure 5.2.7 Example of delamination with a specimen as seen in a CT scan.

Figure 5.2.7, provides an example of delamination within a specimen at the interface between -45° and 0° plies, as it appears in a CT scan. It can be visualized as darker triangular shapes surrounded by matrix cracks. The presence of delaminations are critical

to observe since they play a significant role in determining load carrying capacity of the plate.

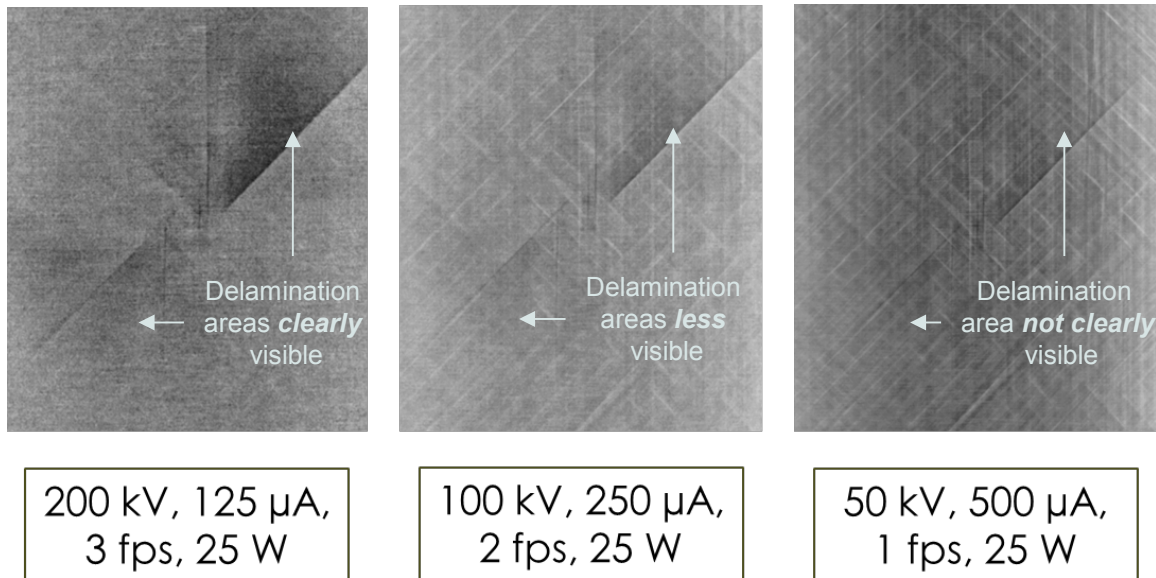


Figure 5.2.8 *In-plane slices of reconstructed volumes acquired at different accelerating voltage and current values (total power and focal point size were kept constant).*

Three scans of the impact plate were performed at different kV values while maintaining a constant overall power (25 W). The choice of power is vendor-recommended parameter to ensure smallest size of the focal spot. The current and exposure were suitably matched in order to achieve 25 W power. **Figure 5.2.8** illustrates the same slices of the reconstructed volumes acquired at the three different scan settings as previously described. It can be observed from the figure that the reduction of kV, led to almost complete disappearance of the darker triangular regions. While the delamination planes were very pronounced in the 200 kV scans, they become absent in the lower kV scan. The cracks remained visible in all three scans. Although the 50 kV, 500 μ A, and longer exposure scan significantly improved the contrast of the plies making it possible to distinguish the layup and ply orientation in

high detail, the vital information regarding delamination was completely missed in the reconstructed volume. Thus, given the improved visibility of the delamination (which is the most critical defect that needs to be detected) at higher kV, guided the choice to use 200 kV for all the subsequent scans of the actual impact plate test specimen that appear in later in this chapter.

Laminated composites represent a significant class of flat, high aspect ratio objects that are very common in aerospace applications. For such panels, blades, wings, flexbeams etc. the acquisition angle range is usually curtailed (less than 100°) due to the virtually infinite in-plane dimensions. In some instances, the high-aspect ratio of the plate structure causes poor through-length photon penetration forcing a limited angle scan even if full 360° angular coverage was possible. These restrictions make limited angle scans an unintentional consequence for plate-like structures. It is therefore imperative to effectively reconstruct such scan data to accurately detect the presence of defects that could compromise structural integrity.

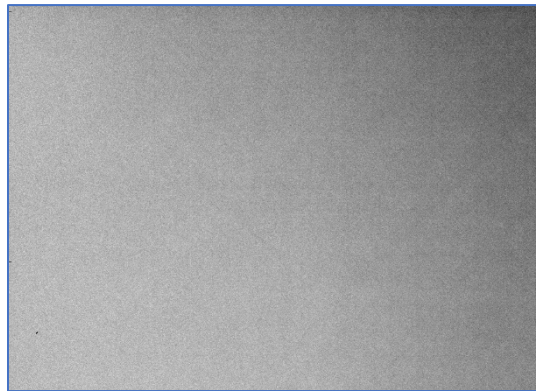


Figure 5.2.9 2D radiograph of plate specimen

In the particular sample studied here, the impact damage was not visible from the surface. However, material testing indicated diminished strength of the part after being subjected to impact load. A 2D X-ray does not provide sufficient information regarding the nature and location of the internal defects. In reality, the damage present within the plate may be so severe that the cracks and delaminations may propagate into a 3D interconnected network in every ply through the thickness. Such a scenario would be virtually undetectable in a 2D

X-ray radiograph. Even if the 2D radiograph could indicate the presence of some of the defects, the limited information it provides may severely underestimate the true extent of damage. In situations where the scan does not cover the entire field of view and superficial damage is neither visually apparent nor discernable from 2D radiograph, multiple localized scans need to be performed to cover the area. **Figure 5.2.9** shows a representative 2D radiograph of the plate scanned for this study. No discernable information regarding presence of defect such as cracks, delaminations etc. is available from the radiograph.

Figure 5.2.10 compares LAT scans at different angle ranges of one particular slice (named Slice 85), all reconstructed using FDK. The starting position of the scan was perpendicular to the thickness of the plate. Therefore, the X-rays had to traverse the longest direction of the plate. In this case, the LAT 180° presents as close to a true representation of defect presence within the plate as a full 360° CT scan. We can observe from the 180° scan, darker triangular regions that represent the delamination areas and cracks at 0° and 45° plies. As angular range decreases below 180° and if no projections are acquired through the length axis of the part, the absence of corresponding projections within the dataset causes an immediate drop off in sensitivity to defect detectability. Significant deterioration of reconstructed image volume is apparent with a reduction of angle range by just 20° as seen when comparing LAT 160° to LAT 180° . Also, none of the images are able to distinctly see the 0° ply corresponding to the true slice shown in below LAT 180° . Below LAT 180° , the delaminations are no longer visible in the LAT images. However, the LAT images are all able to detect cracks, although to varying extents.

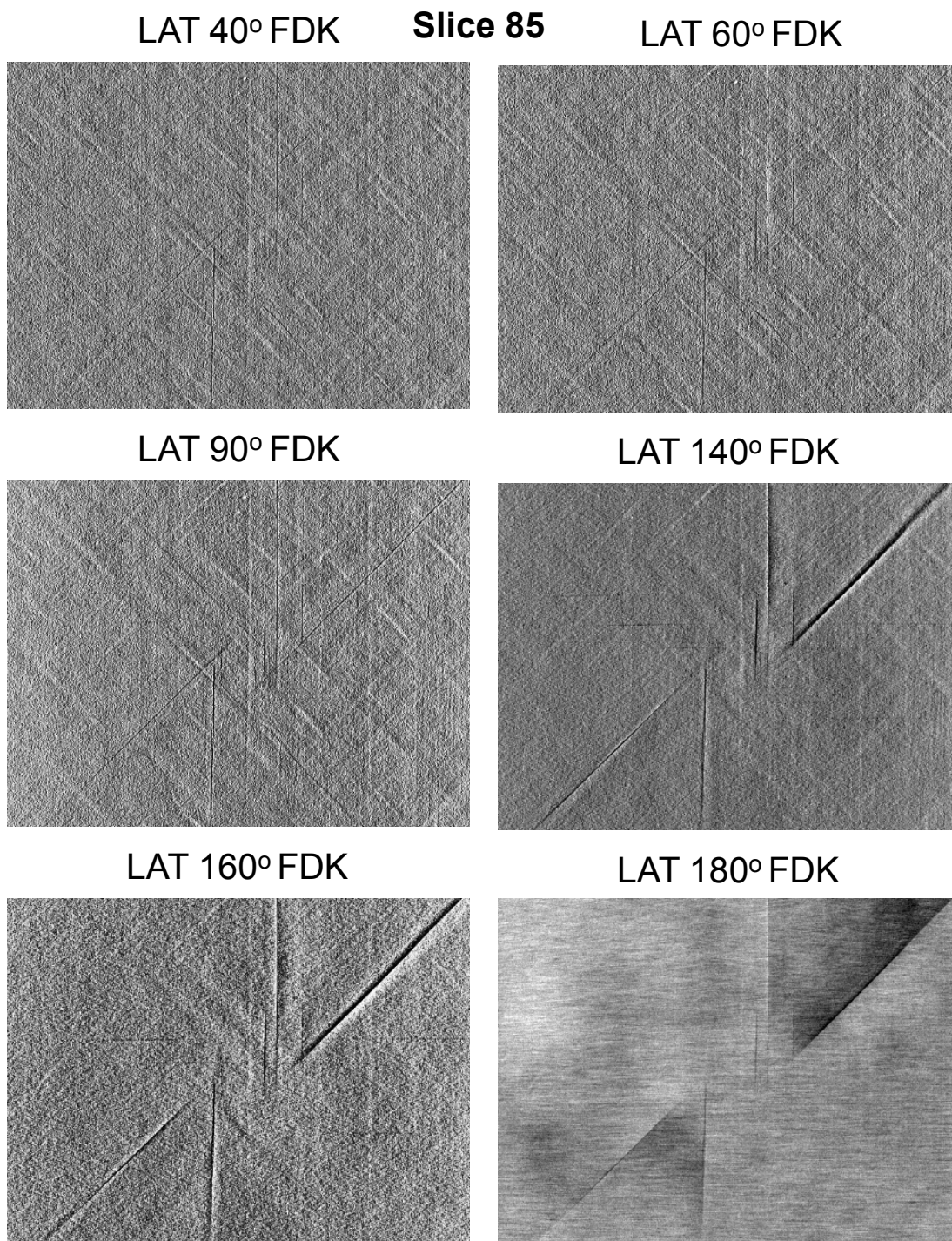


Figure 5.2.10 LAT scans at different angle ranges of Slice 85.

Consider another slice, Slice 90 from the same plate sample as shown in **Figure 5.2.11**. Using LAT 180° as the reference image, it can be observed that the darker delamination regions are completely absent in the smaller angle LAT images. Once again, 0o ply is not visible in the LAT images below 180° . The most striking feature about the LAT 180° image of the slice, is the appearance of horizontal lines representing 90° matrix cracks. None of the other LAT images pick up the presence defect. Interestingly, the $\pm 45^\circ$ cracks become more pronounced and appear thicker in the LAT 160° and 140° yet are barely distinguishable in LAT scans below 100° .

It is important to note that this is not necessarily reflective of the true nature of the defect and could be a by-product of overlaps from adjacent slices. Another peculiar observation is the presence of several horizontal lines of the 90° matrix cracks that appear in the LAT images with different levels of clarity as the angle range decreases. Based on the LAT 180° , it is evident that these cracks are not truly present in that particular slice but features inherited from adjacent slices that do contain those cracks.

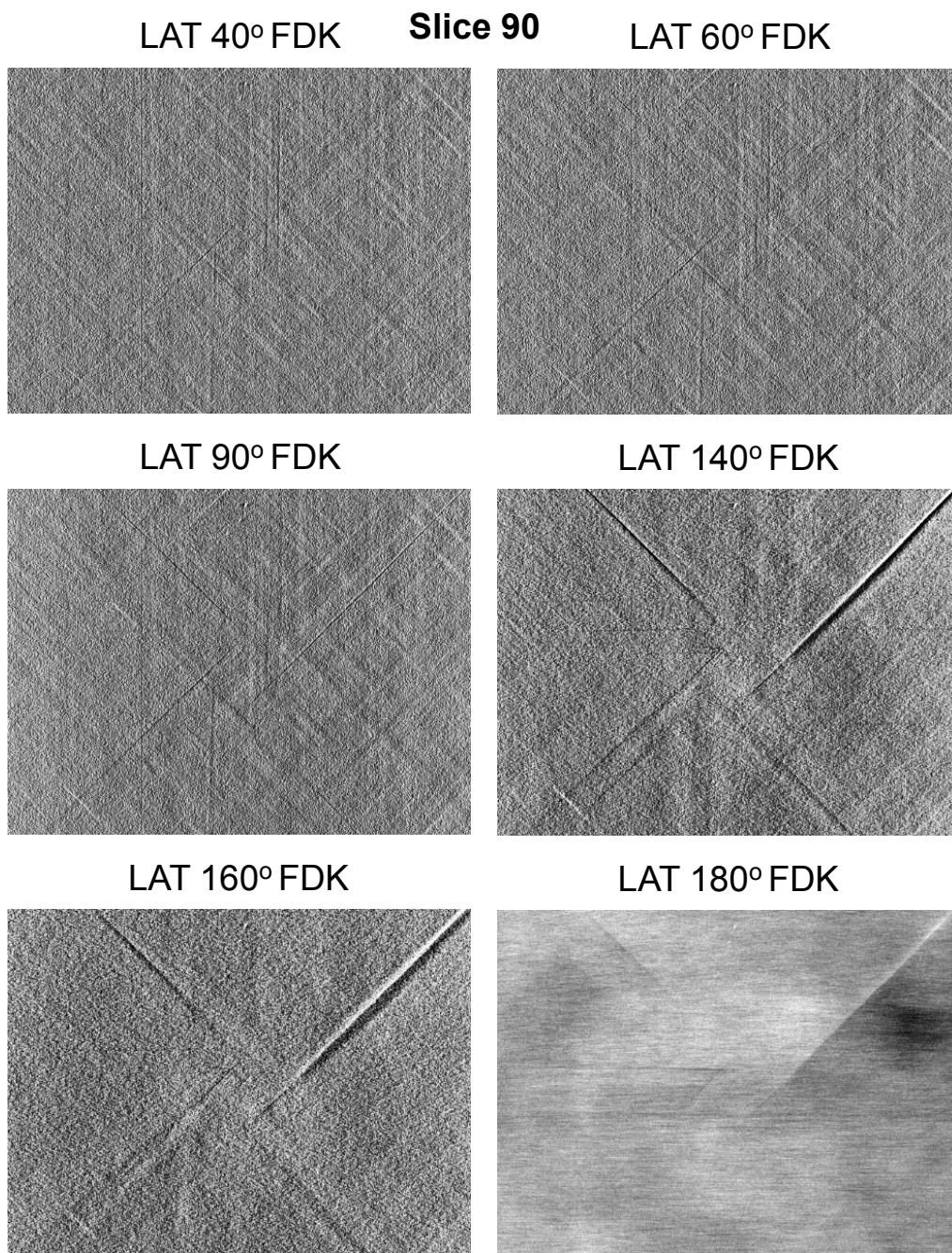


Figure 5.2.11 LAT scans at different angle ranges of Slice 90

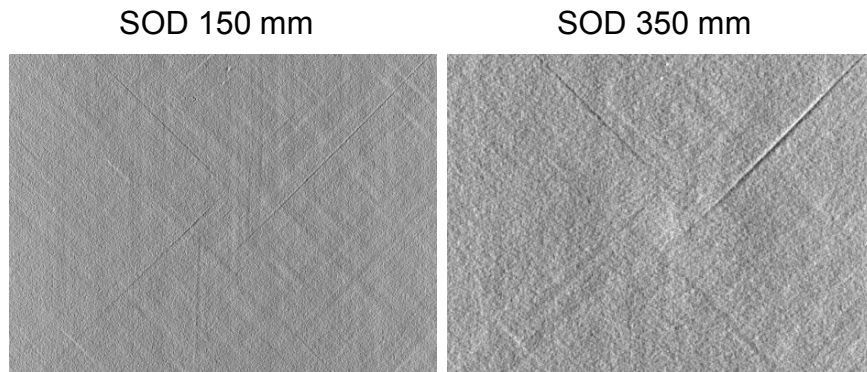


Figure 5.2.12 Comparison of LAT 90° slices acquired at SOD 150 mm and 350 mm.

In the case of planar objects like plates, depending on their dimensions, the angle drop can be very abrupt. Thus, in practice angles below 100° is usually close to the upper limit of what is achievable for such high aspect ratio parts. The concept of TS being explored here, will require the synthesis of information collected at various different distances to maximize resolution and depth perception. **Figure 5.2.12** shows two LAT 90° image slices acquired at SOD 150 mm and 350 mm respectively. With larger SOD, a clearly noisier, more pixelated, low-resolution scan is produced. In this image volume, the 45° crack appears much wider than the representative ‘true’ LAT 180° seen in the previous figure. Although it makes the crack detection easier, it could also potentially lead to obscuring defects present in regions adjoining the crack. At closer SOD, a much sharper image is produced with higher-resolution and fewer artifacts. The texture of which ply is being observed is more apparent in the SOD 150 mm image slice, although due to superimposition from adjacent slices, it is difficult to predict with absolute certainty.

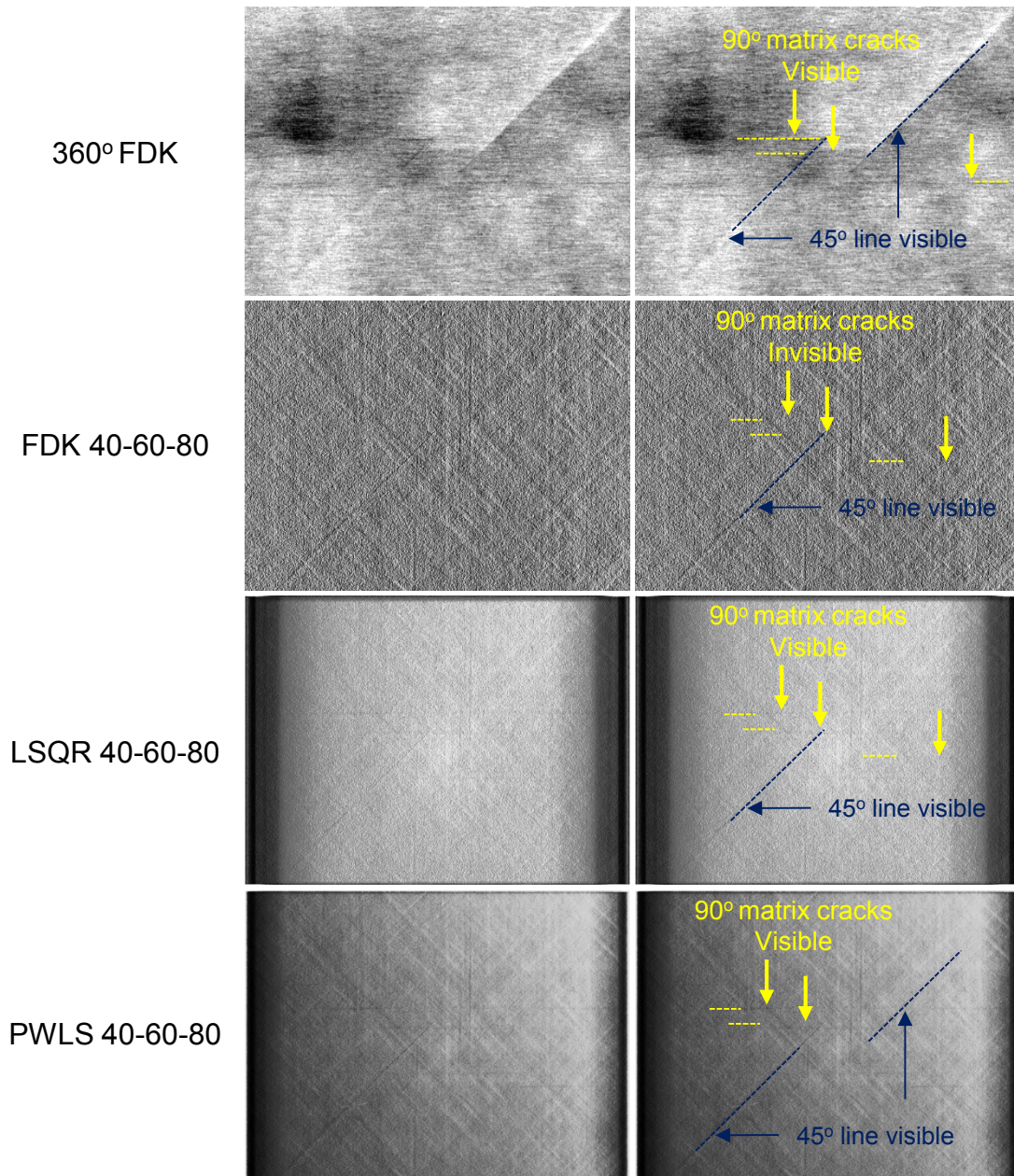


Figure 5.2.13 Comparison of FDK, LSQR and PWLS reconstruction solution methods. Dashed lines are provided on the images on the right, to guide the reader.

Given the previously mentioned motivation to achieve flaw detection with scan angle ranges below 100° due to practical constraints, TS was performed using three different SODs and three corresponding angle ranges 40° , 60° , and 80° . Effective reconstruction

techniques are vital for the successful adoption of medical CT to composite analysis. Three different methods as previously described were considered for reconstruction of the image volume - FDK and two iterative methods, namely LSQR and PWLS. **Figure 5.2.13** shows the comparison of LAT 40° - 60° - 80° reconstructed with the three solution methods. A reference 'true' image is provided in the form of a full 360° CT (reconstructed using FDK). The horizontal lines indicating cracks were quite clearly apparent in the iterative method images.

They were most prominent when reconstructed using PWLS method. The FDK did not show them at all. Based on the true 360° CT, only the horizontal lines should have appeared in the image, but in our case the horizontal lines appears along with imprint of the vertical as well as 45° lines. The appearance of the 'fat' 45° line seen in the TS slice, most likely is a feature inherited from the lower resolution wider angular range scan. A few horizontal lines also appear in the iterative method solutions that do not actually exist in the full CT. As previously mentioned, these are likely features inherited from adjoining slices. In the iterative methods, although flaw detection appears relatively better, it can be observed that there is loss of data at the edges of the image in the form of dark vertical bands. These edge artifacts could potentially obscure important flaw data present in those regions.

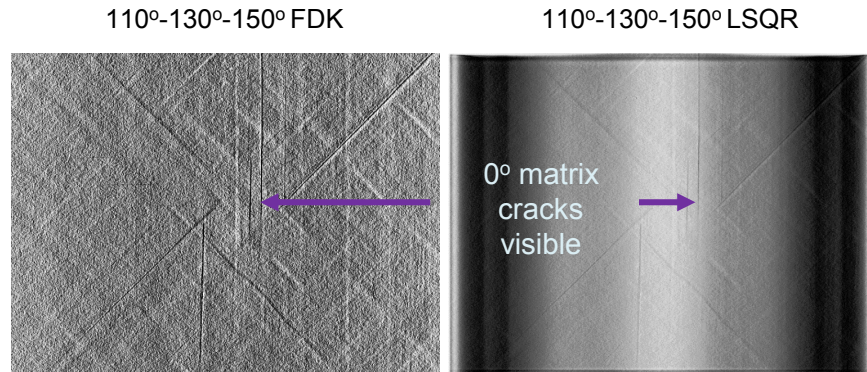


Figure 5.2.14 Comparison of FDK and LSQR solution methods applied to wide angle range (110° - 130° - 150°) TS scans.

Finally, an interesting effect can be seen in **Figure 5.2.14**. Consider the wide angle scans (110° - 130° - 150°) reconstructed by FDK and LSQR methods. The edge artifacts of ROI for the wider angular range appear more pronounced for the iterative solution method. The edges appear to have darker vertical bands at the edges, while the central region appears to be relatively whiter. This may provide misleading indications regarding the density of material in the region. In actuality, this is a result of a glitch in the solution method.

This is a well-known tomography problem: reconstruction of region-of-interest (ROI) volumes. This problem arises when an inner part of a larger object is reconstructed such that the radiographs include projections of material that is not part of a solution. This problem presents significant challenge to stochastic reconstruction methods as it prevents them from efficient use of cost functions. In addition to the artifacts, the wider angle range used in these scans is impractical in most cases. Nevertheless, this could be worthy of further exploration. The overall quality of the LSQR reconstructed volume appears smoother than the rather textured, sharp FDK reconstruction. Although 0° cracks are clearly visible in

these scans, no horizontal 90° cracks were visible. These cracks were previously detected in the 40°-60°-80 reconstruction which contained information from several overlapped slices. So an extension of angular ranges does not necessarily provide an improved detection of flaws as compared to the narrower angle range.

5.3 Void Defect in Glass/Epoxy Composite

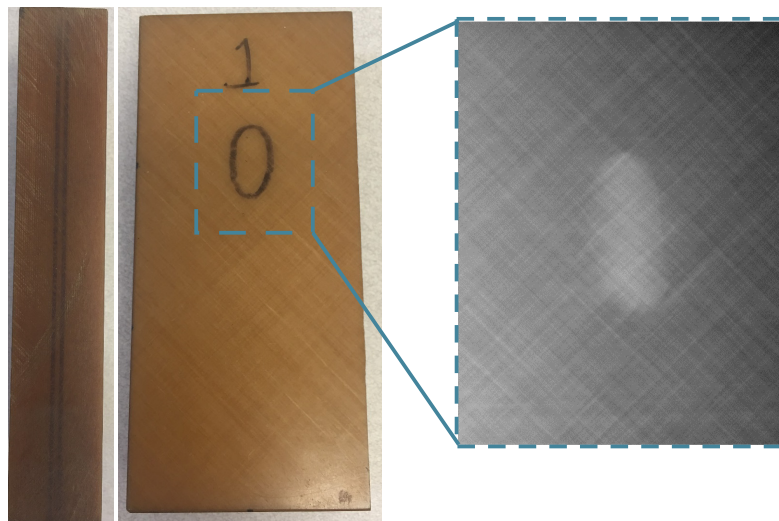


Figure 5.3.1 Image of the Glass/Epoxy composite structure with a 2D X-ray radiograph of the demarcated region.

For the study, a 68 ply S2/8552 Glass/Epoxy laminated composite with $[(\pm 45)_2/0_4]_4/45/-45]_s$ layup was considered. **Figure 5.3.1** shows the 2D radiograph of the Glass/Epoxy composite material with a seeded void inside. In this case, the detection of the defect is straightforward. The presence of a void inside the part is readily apparent. However, this one view alone does not provide adequate information regarding the location of the defect within the thickness of the object. Further, it would be impossible to know if multiple

defects were in fact being overlapped in what appears to be a single defect in the image. Additionally, localized defects like waviness and cracks, associated with the presence of voids, cannot be detected based on this radiograph.

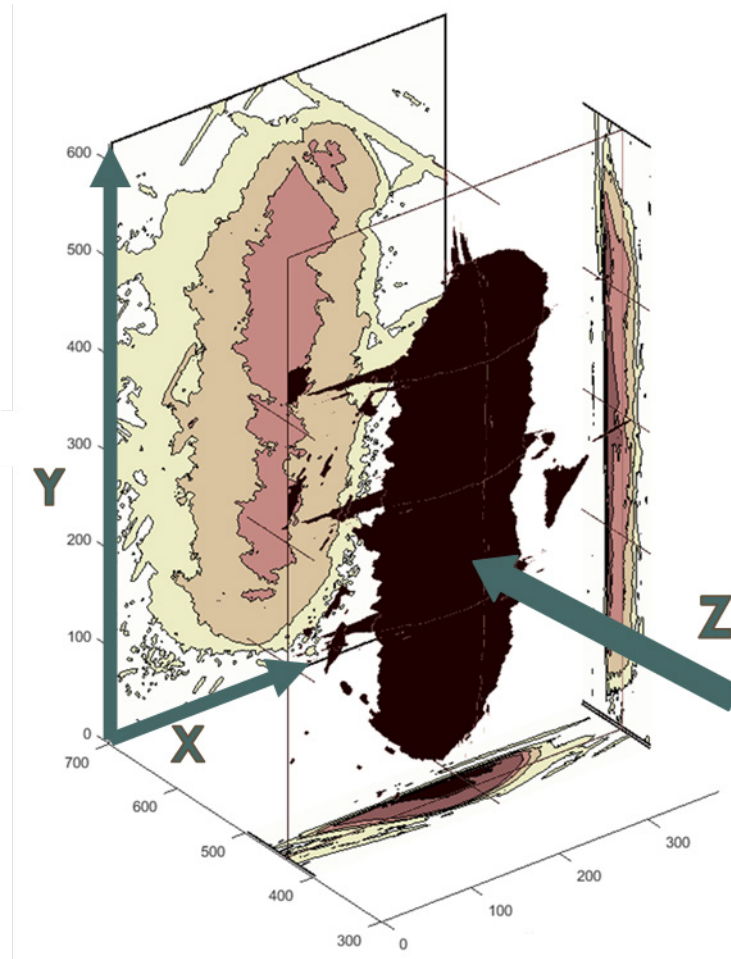


Figure 5.3.2 Schematic volumetric representation of a void inside the object with respective projections onto the X, Y, Z planes in the form of contour plots.

Figure 5.3.2 was obtained by processing the slices of full CT reconstructed volume in an effort to visualize the volumetric shape of the void defect present inside the composite parts. The void is shown to be projected onto the X, Y, Z planes in the form of the contour

plots, where darker areas represent the denser regions. By overlapping the slices into a single projection on corresponding planes, different dimensions of the void at different depths are clearly visualized.

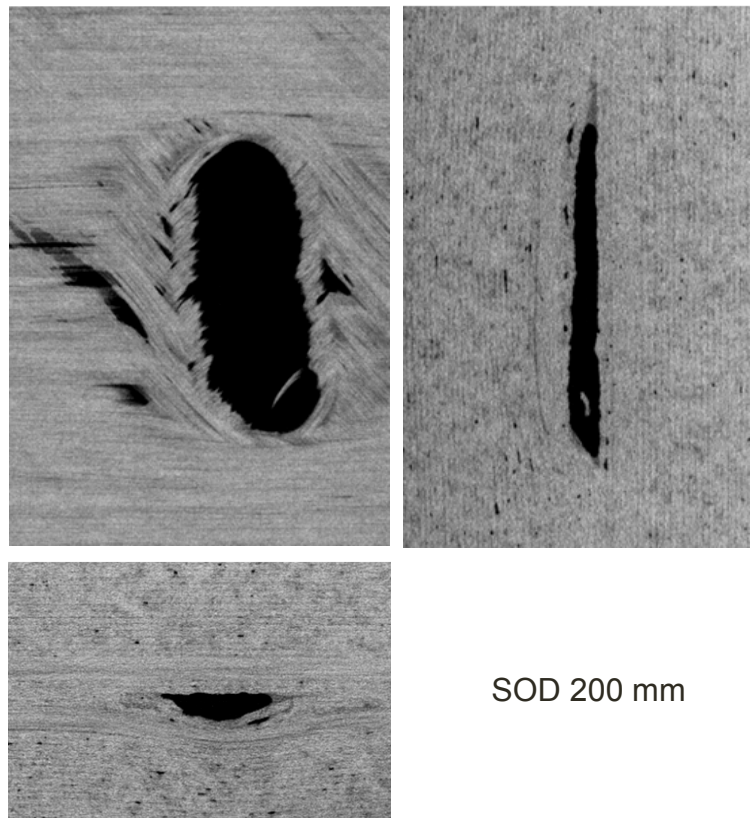


Figure 5.3.3 Example of X, Y, Z 2D X-ray slices obtained from full CT of the Glass/Epoxy composite with a seeded void.

Now, the result of full-angle CT scan, performed on the part is shown in **Figure 5.3.3**. The full CT shows a much more accurate representation of the real internal structure of the part with a higher level of detail captured. In particular, slice Z reveals that there are several more voids and in-plane waviness around the large void. olume slices in X and Y direction

show the thickness of the void, some resin rich area as well as the matrix crack framing the void. It is worth noting, due to the different densities of the glass fibers and epoxy, it is easy to distinguish the individual plies and their orientation. This makes it possible to unambiguously pinpoint the location of a defect with respect to a particular ply. Given that this particular part has not been in service or tested previously, the detection of matrix crack is an interesting finding. It suggests that crack formation occurred during the fabrication process of the part. To conclude, it is evident that a host of additional information can be acquired using the full CT, which was clearly inaccessible in the 2D radiograph from Figure 5.3.1 seen previously.

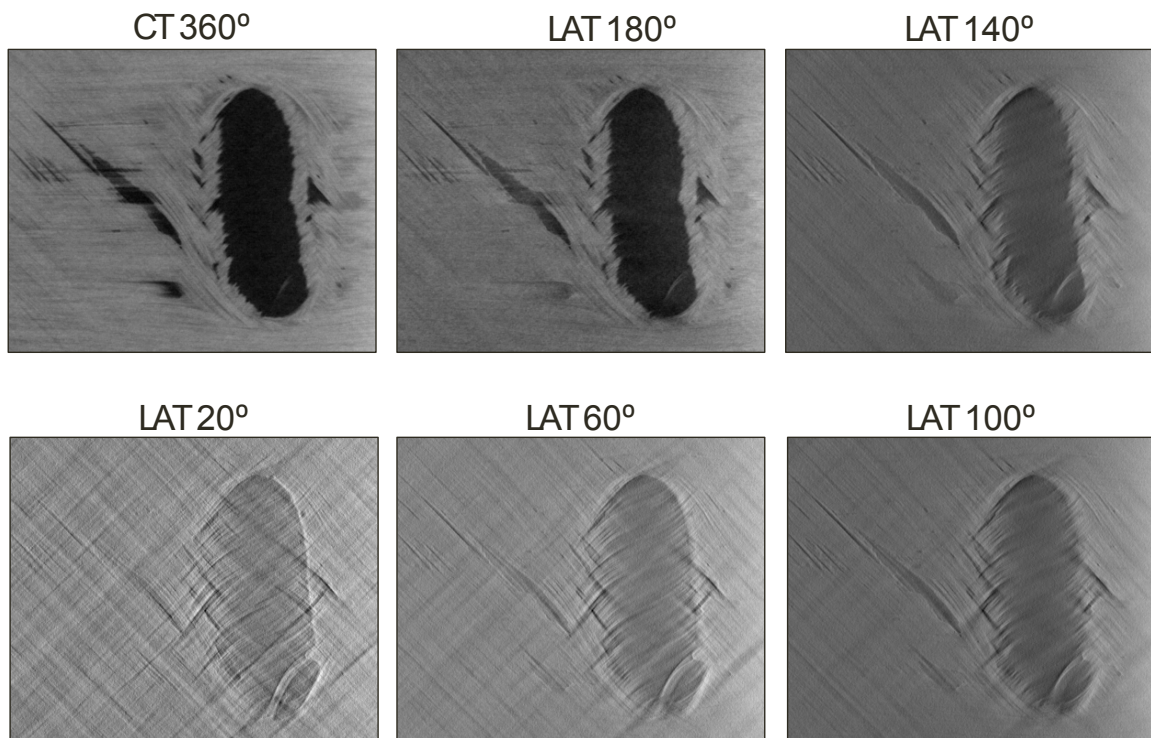


Figure 5.3.4 Representative in-plane slices of the void as LAT angular range decreases from 180° to 20°.

After the full-angle 360° CT was performed, an attempt was made to simulate LAT in the event that a full angle range scan was not possible (**Figure 5.3.4**). This recreation was achieved simply pulling projections out of the dataset acquired during the previously shown 360° CT (Figure 5.3.3). This study helped provide insight regarding how the LAT may affect the appearance of a given defect in the reconstructed volume. The fact that the defect in this case, i.e. the void, possesses some volume, meaning it is not completely flat, makes it detectable even at the smaller angular ranges. Although visually, the reconstruction quality of the LAT at small angles may appear to be unsatisfactory, it is clearly a big improvement compared to the single 2D radiograph. In these slices, the imprint of the contour of the void can be seen very well. With the decrease of scan angle, the depth (seen as the darker area) becomes less pronounced. Additionally, some features present in adjacent slices get superimposed, giving the impression they are all located at the same depth.

It can be observed more clearly later that in all LAT scans, the shape of the inner void in the through-the-thickness direction is distorted, leaving an imprint of its shadow in the neighboring slices. This is an image artifact, since in real part the void does not actually exist in that respective ply. The artifacts appear to different degrees in the volume from top and bottom primarily because of the shape of the void. As this particular void in consideration happens to be more elongated on the bottom, it tends to leave a longer trail of artifacts in the lower slices. If one considers two arbitrary slices at some similar distance above and below the void. The existence of the void may not be evident in the top slice,

while artifacts related to the void would still continue to appear in the bottom slice. **Figure 5.3.5** shows a comparison of the 2D radiograph to in-plane slices at LAT of 20° and 60°. Evident from this images is that the increased angular range allows for better depth resolution of the features.

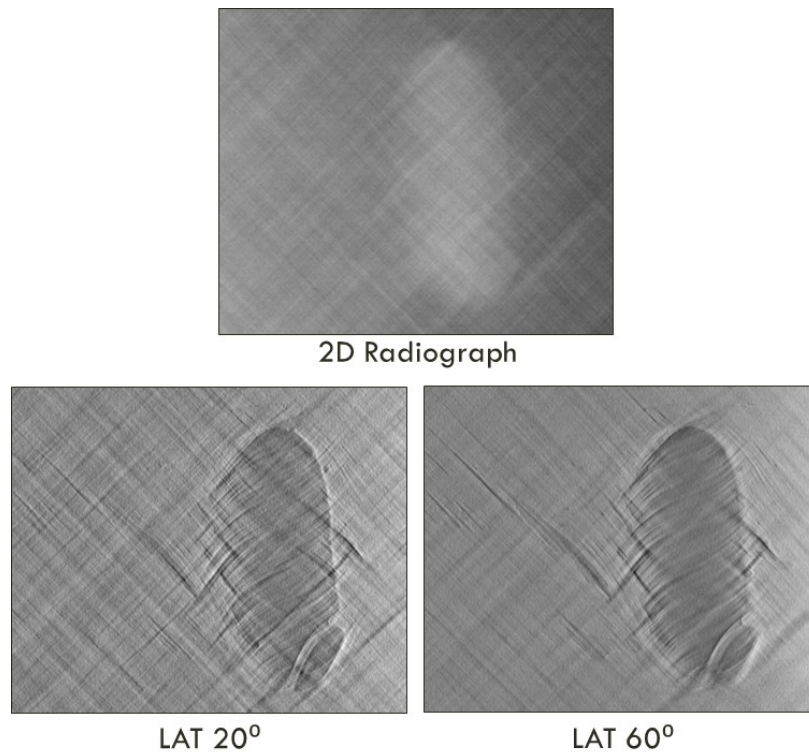


Figure 5.3.5 Comparison of 2D radiograph to the respective in-plane slice of the void as LAT angular range increases.

The Y slices in **Figure 5.3.6** demonstrate the very rapid deterioration in shape with the decrease of angular range. The nature of superimposition of the cone beam gives rise to particular artifacts in the volume. Consider the streaking lines seen in the LAT reconstructions in Figure 5.3.6. It can be observed, that the lines are tangential to the void

in two direction, forming the kite shaped artifact of certain size in the cross-sectional view. The angle of interception between these tangential lines is related to the scanning angular range and the angle of incoming cone beam.

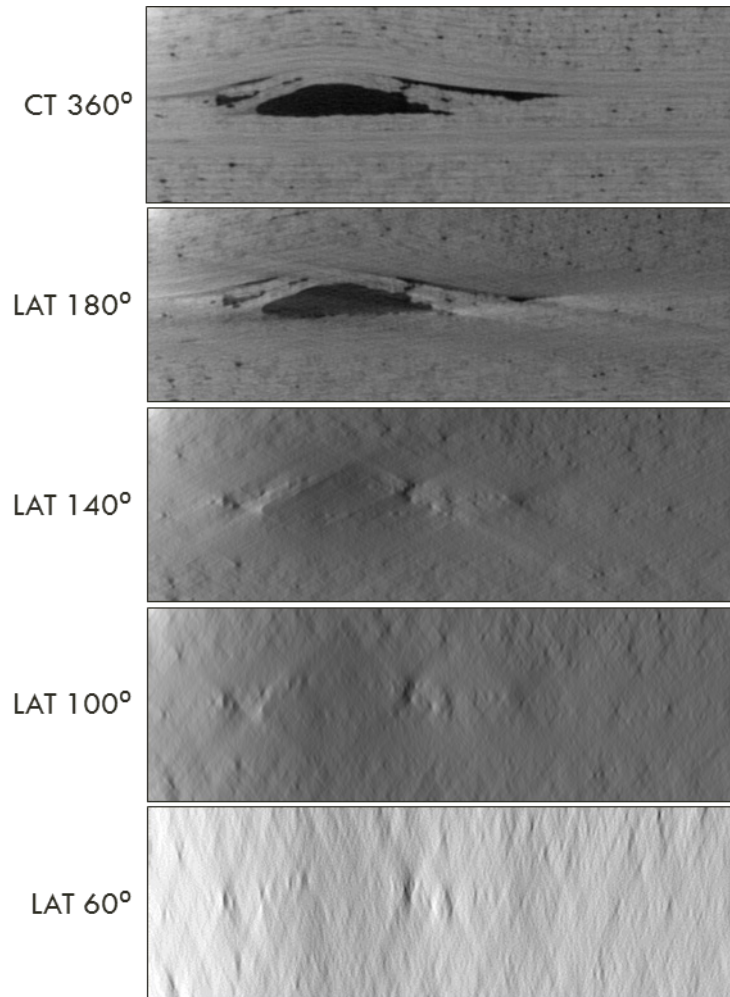


Figure 5.3.6 Shape deterioration through the thickness of the part with the decrease of LAT angular range.

Since both of those values are known, the shape of the kite artifact can be predicted beforehand. Unfortunately, with the decreased depth perception of smaller LAT scans, the

greyscale range of the overall reconstruction volume is reduced, which causes the now kite shaped void to be barely noticeable. If the operator is already aware about the presence of some indication, gained from the frontal projection, intensifying the contrast of that slice could help recognize the kite shape in the Y slice.

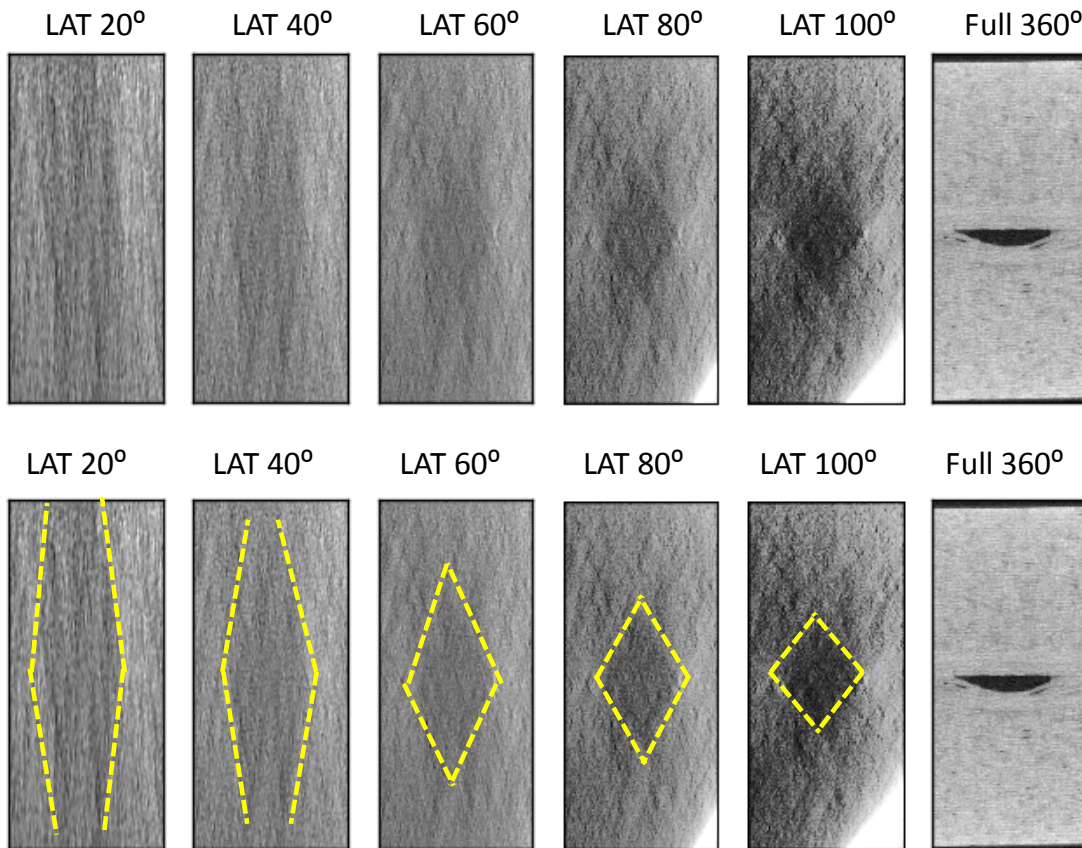


Figure 5.3.7 Example of shape deterioration in real scans (through-thickness direction) with decreasing LAT scan angles.

Figure 5.3.7 shows the shape deterioration in a real LAT scans of a composite with a void. Although in the previously studied phantom, the shape of the inclusion was still apparent in some of the LAT scans, seen in Figure 5.3.7 illustrate the complexity of making

judgements in real-life scenarios. Nevertheless, it is possible to apply the knowledge gained from the idealized phantoms to estimate the distorted shape of the void in the LAT scans, based on the known angle of scan acquisition due to the previously described phenomenon. Although the exact shape of the void is indistinct, the higher LAT angle scans show the presence of a kite-shaped shadowy region in the center of the image slice. Based on the centroid of this shape, it can allow for approximate determination of the in-depth location of the void. An example of such an analysis is provided in **Figure 5.3.8**. Two representative slices from LAT scans at 60° and 100° are shown with overlaid blue lines approximating the width of the defect, measured from the in-plane slice. Once the width is relatively accurately determined, lines bounding the shadowy region may be constructed to inscribe the shadowy region given the hypothesis that the angle included between the intersecting bounding lines of the kite are a function of the LAT acquisition angular range. By considering two extreme angular ranges where the shadow artifacts are clearly visible, it could be possible to determine along with an error estimate, the dimensions of the void in the through-thickness direction. This determination would still be highly susceptible to operator judgement and is worthy of further study to ascertain its validity and applicability. Especially considering the unfeasibility of full CT and when LAT is the only technique available, any determination of defect dimensions and location with some degree of certainty would be of great value.

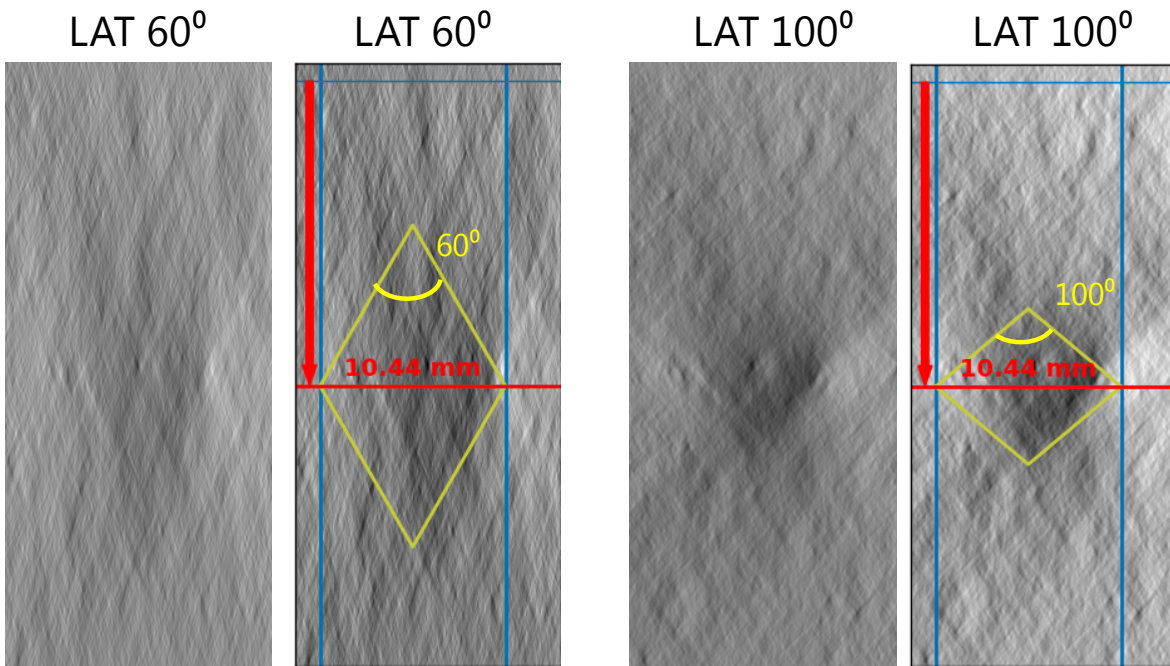


Figure 5.3.8 Proposed method for depth and width determination of void in the through-thickness direction in LAT 60° and LAT 100°.

5.4 Comparison of LAT and TS for Void Analysis

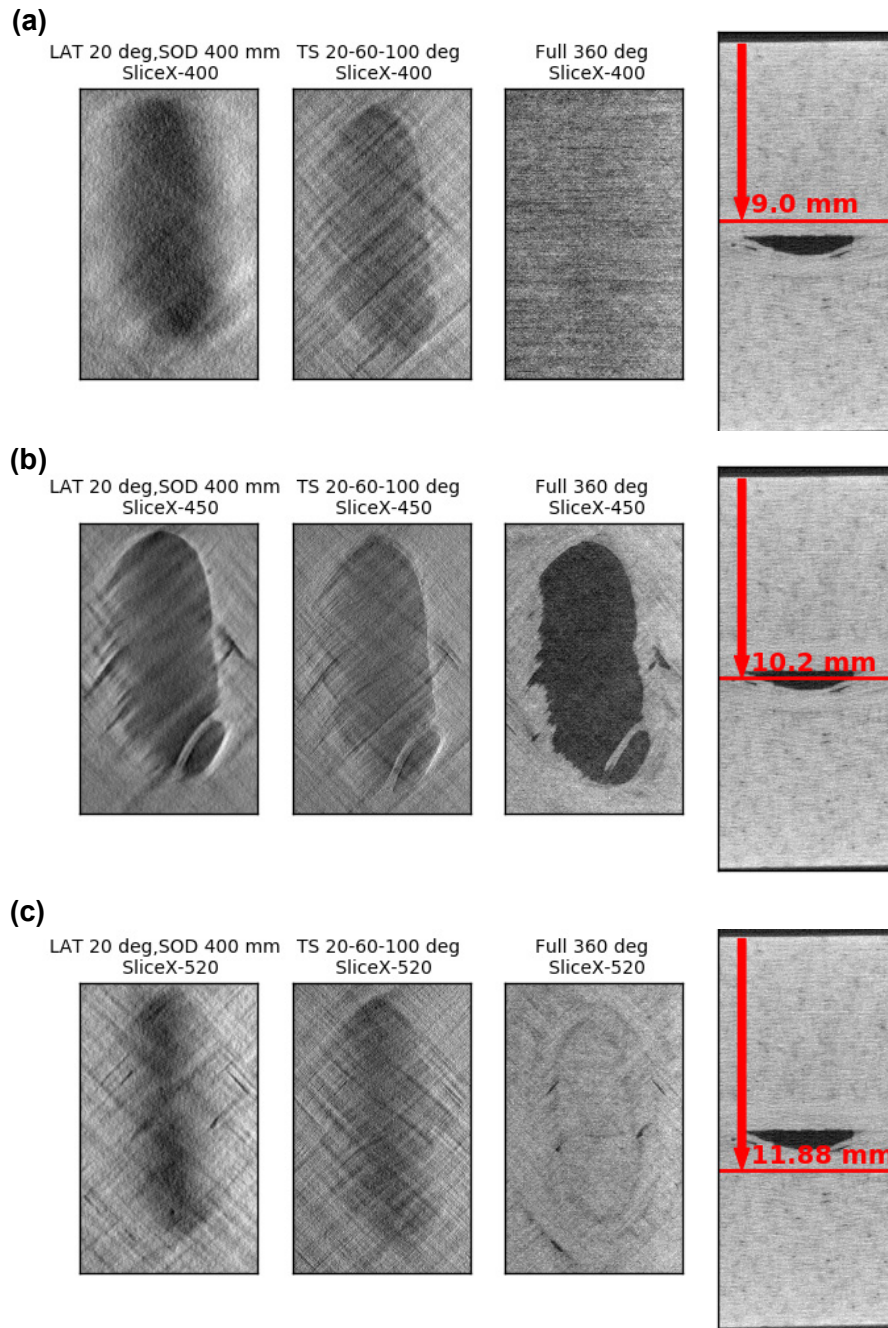


Figure 5.4.1 Comparison of in-plane slices at three different depths within the thickness obtained from LAT of 20°, 60°, and 100° scans.

A wider angular range would allow to better resolve features through the depth. Consider **Figure 5.4.1** which shows a series of in-plane slices through the sample of three volumes, reconstructed from a limited projections set of 20° , 60° and 100° ranges. The in-plane slices are displayed at three locations through the thickness of the sample. Figure 5.4.1 shows XZ slice with three in-depth locations chosen in the following manner: two of them show slices above (a) and below (c) the void (and in reality contain only material) and a slice that goes directly through the void (b).

The cross-section views are compared to a reference in-plane slice in the full 360° volume. XZ slice on the right of each image marks the corresponding slice location through the thickness. The red arrow stretches from the edge of the object, denoting how deep from the surface the slice is. Since the resolution of the scan is known, it is possible to measure the real distance. This information is vital for composites. Since the ply thickness and layup are known, it is possible to determine which ply is affected by the defect. Based on this knowledge, the danger of the defect can be predicted.

The distortion length of the void through the depth is different depending on the angle range of the LAT. In the LAT scans using wider angular range like 100° LAT, the observed shadow artifact from the volume disappears earlier than the LAT 20° . For example, at slice 9.7 mm depth, we see considerable reduction in the manifestation of the void (in LAT 100°) within the slice as compared to the respective slice in LAT 20° , where the shape of the void still remains apparent. The contrast of greyscale values in the image offer an indication of the depth of the scans. The clearly darker area of the void seen in LAT 100° is very distinct as compared to the surrounding material. Meanwhile, in the LAT 20° , the

difference in contrast between the void region and its surroundings is significantly diminished. It can be observed that even at smaller angular ranges, the contour of the void is quite well defined. This is because the shape information is inherited from the frontal projection view (essentially a single radiograph) which indicates the presence of the void as well as provides its in-plane dimensions. Thus, the in-plane parameters of the void do not get affected by the limited nature of the scan.

Figure 5.4.2 shows a comparison between LAT and TS for a 160° angle range. In this particular example, the goal for the TS was to enhance the scan obtained at the farther distance with the high-resolution information gathered from closer SODs. Additionally, for the slice located at 9 mm depth, it can be seen from the full 360° CT that no void is present. The LAT does not show a presence of void. However, the TS shows indications of the presence of a void.

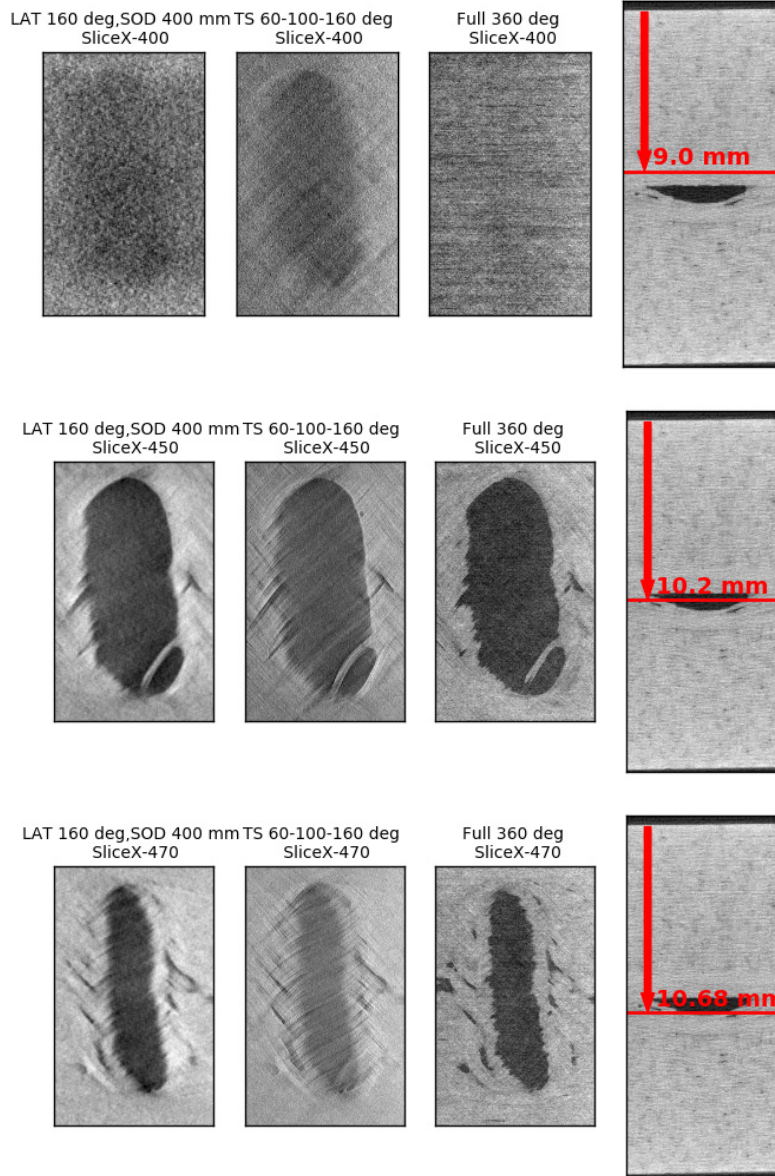


Figure 5.4.2 Comparison of in-plane slices at three different depths within the thickness obtained from LAT and TS for 160° range and full 360° CT scans.

In the LAT of slice at 10.2 mm depth, the image contrast is higher, clearly distinguishing the void. The details in the image appear slightly blurry and washed out, especially when compared to the sharp (although relatively lower contrast) well defined void boundary seen

in the case of TS. It is important to keep in mind, however, that all the features seen in the TS image are not necessarily real and could be image artifacts produced due to superimpositions of features from adjoining slices. The slice at 10.68 mm is essentially at the lowest point of the void. The shape of the void produced by LAT and TS closely resembles the one from the 360° full scan. It will be seen later that this is on account of the relatively large angle range employed for the scan. The previously observed trends with respect to feature sharpness and contrast remain consistent.

Figure 5.4.3 show comparison of slices at four different depths obtained by LAT and TS at 80° angular range. There are several differences that can be observed when comparing the images seen previously in Figure 5.4.2 obtained at 160° angular range. For instance, at 9 mm depth, both LAT and TS already begin to show a vague appearance of the void, although it actually does not exist at that slice in the full scan. At 10.2 mm depth, approximately in the middle of the void's depth, the actual contour of the void is relatively well reproduced by both LAT and TS. However, small features appear in both the LAT and TS (region bounded by the orange rectangles in the figure) that are non-existent in reality, according to the full CT image. Even though there is the same contrast and sharpness differences as previously seen between the images obtained by the TS image over the LAT, it can be seen that there is no significant improvement in image quality between the two techniques in this particular case. In both cases, line artifacts (two such instances are marked by arrows on the corresponding images) appear, that are not seen in the 360° full CT. These are probably inherited from the waviness present in the adjacent plies.

Now, consider the slices at depth 10.68 mm, especially, the region shown bounded by the red dashed rectangle in the full CT. Small voids are clearly present as represented by the dark regions seen in the 360° CT image. In the LAT and TS images, these defects are almost or completely absent. Strikingly, compared to the full CT, the width of the imprint of the void continues to follow that of the maximum width of the void. The extremely misleading nature of this artifact is apparent from the three images of this particular slice. While the full CT shows a significantly smaller void width at that depth, both LAT and TS continue to propagate the original wider width from the slices above it. In contrast, previously, in Figure 5.4.2, showing the 160° scans, the width information was more accurately represented on account of the wider angular range.

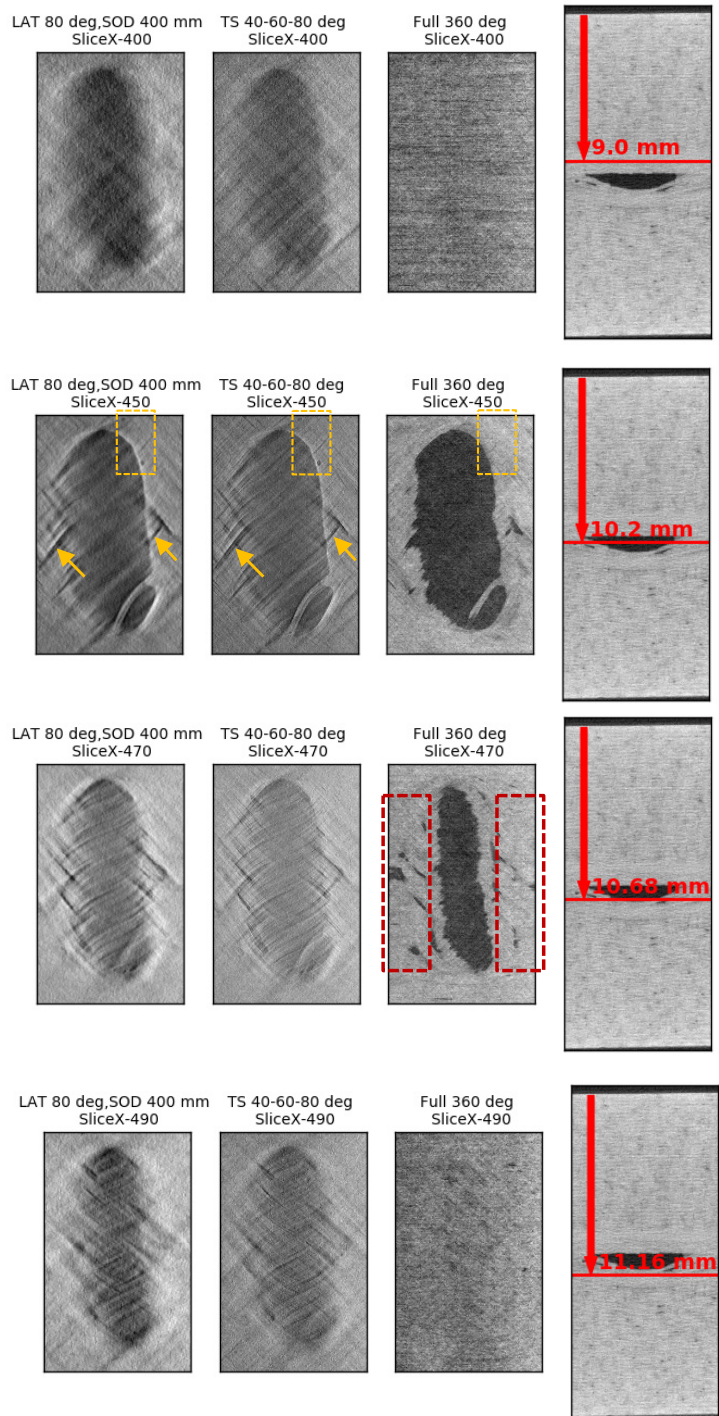


Figure 5.4.3 Comparison of in-plane slices at three different depths within the thickness obtained from LAT and TS for 80° range and full 360° CT scans.

5.5 Reconstruction of Void Using Iterative Methods

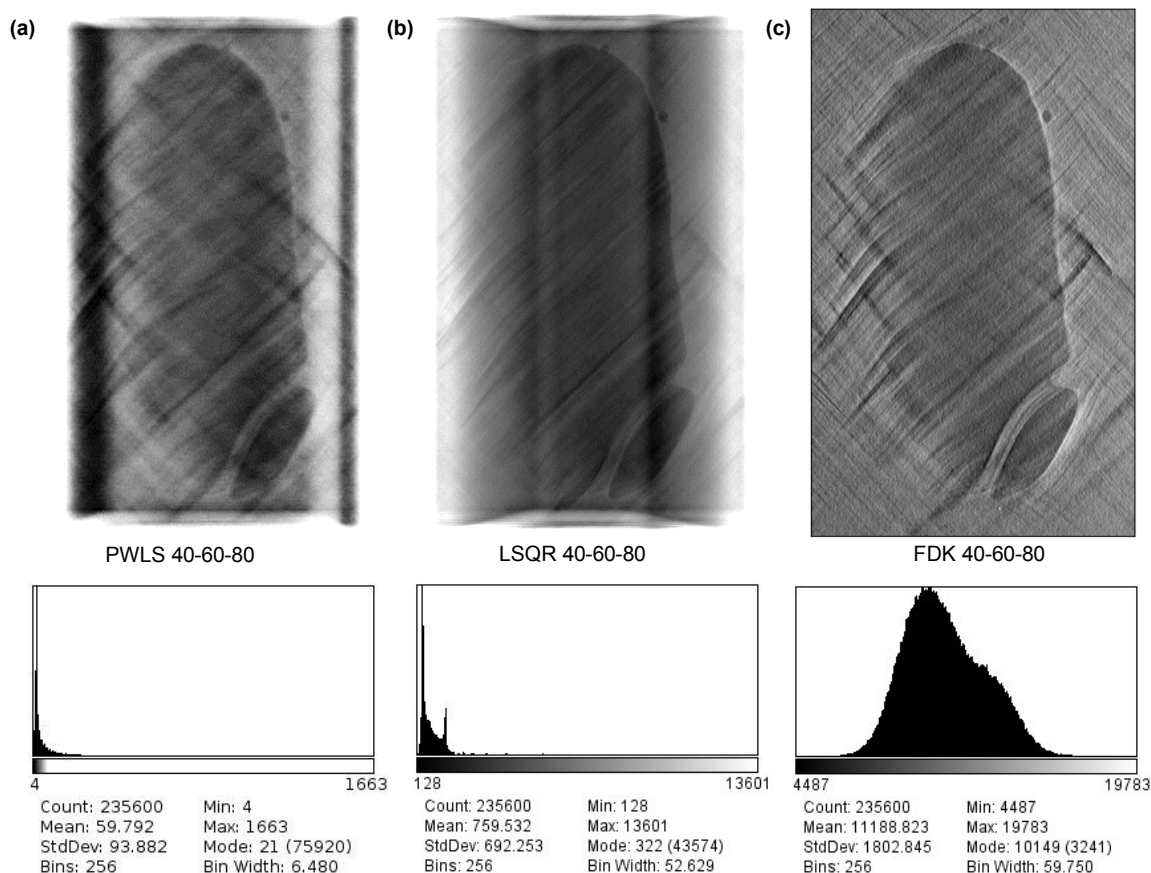


Figure 5.5.1 Comparison of algebraic (a) PWLS & (b) LSQR and analytical reconstruction methods for tomosynthesis example.

Figure 5.5.1 shows the in-plane slices from three different reconstruction methods. Figures 5.5.1a and b compare iterative PWLS and iterative LSQR methods respectively to the FDK analytical solution seen in Figures 5.5.1c. Both iterative methods appear to be superior to Fourier-based methods in terms of depth. While in FDK, the void shape in the Y-direction appears fairly distorted, the statistical methods seem to provide a better estimation of void dimensions in the through-thickness direction. Representative images showing this are not included here to avoid confusion especially since they can be non-intuitive to an untrained

eye. Both iterative methods appear to suffer severely from region of interest (ROI) problems. The reconstructed volumes have pronounced artifacts in the form of vertical columnar artifacts within the images as well as white regions at the edges that appear to frame the image complicating post-processing analysis. As noted, the regions of these artifacts have higher or even extreme intensity values. This would affect the applicability of the previously proposed technique of determining the location and size of the void using the variation in standard deviation of the image slices.

The greyscale intensity profiles of PWLS and LSQR reconstructed volumes, as seen in the corresponding histogram plots in Figure 5.5.1, are strikingly different from the histogram obtained from the FDK algorithm volume. In this particular example, it can be seen that the iterative methods produce images with extremely narrow histograms of greyscale intensity. In contrast, the FDK algorithm reconstructed slice shows a well distributed spread of greyscale intensities without any artifacts such as those seen with the iterative methods. Another ROI problem seen in the images from the iterative methods is the loss of data at the edges of the reconstructed volumes (which is feature that occurs primarily during post processing of the image to more clearly visualize the defect). In the iteratively solved images, the void has an almost translucent quality that makes it difficult to detect, especially without prior knowledge of its existence. Another clearly distinguishable feature is the relative smoothness of the iterative method-based images as compared to the FDK image, where the sharpness of the image appears to provide an illusion of texture.

The iterative methods demonstrated in this figure were performed for a total of 20 iterations. Several parameters including the choice of prior function and the value of

damping factor were explored. The Tikhonov prior was chosen as the most adequate function. The quality of reconstruction did not seem to get a significant improvement after 10 iterations. The regularization parameter remains the operator choice and determination of its range is mostly trial and error. Nevertheless, it was observed that when its value is greater than 0.5, it results in an overly smooth solution. Overall, the statistical iterative methods were still more computationally time consuming when compared to analytical solutions. The computational demands become a significant factor when attempting to study the influence of various parameters and their interplay on the final results.

5.6 Proposed Void Depth Estimation Technique

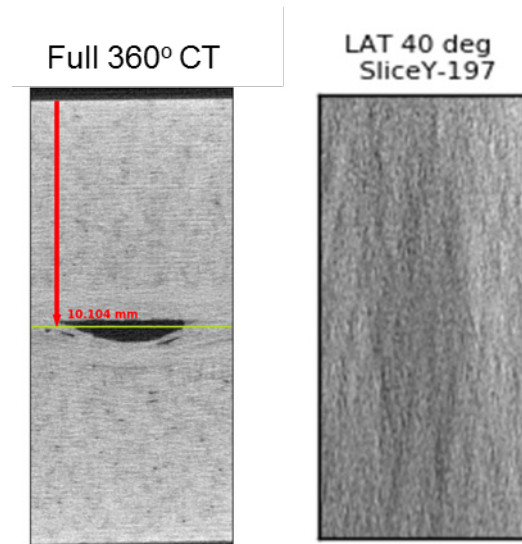


Figure 5.6.1 Comparison of Y-slice of reconstructed volumes in full 360° CT and LAT 40°

Figure 5.6.1 compares the Y slice of the reconstructed volume obtained from full CT and the LAT 40° scans. It is readily obvious that the LAT scan lacks any objective information regarding the void. Rather, the LAT 40° scan shows some smeared shadow artifact shapes that does not provide any quantifiable information regarding the defect. As seen previously, the full CT shows distinct borders on the top and bottom of the image clearly demarcating the thickness of the structure. It is significant to observe that the 40° LAT scan is missing those dark regions that bound the image due to insufficient angular coverage from those views. If it were physically possible to move the part far enough from the source while yet fitting it within the scanner, to obtain a view such that the bounding edges may be captured, their coordinates could be overlaid over the Y-slice of the lower angle LAT in order to determine the depth information regarding the void. So, given a

means to determine the edges of the part, by using the procedure described previously and seen in Figure 5.3.8, it would be possible to determine with relatively low error, the position of the defect within the thickness.

In this section, a new method of measuring the depth and the width of the void through the thickness from LAT and TS scans is proposed. As seen in Figure 5.6.1, previously, the Y-slices do not provide enough information regarding the relative 3D location of the void. The proposed method here is intended to overcome that limitation, by only working with the in-plane slices of the reconstruction that demonstrate both good contrast and high-resolution. The void in the in-plane slices does not display any shape distortion and can be clearly distinguished from the surrounding material. Using that as a criteria to establish the existence of the void within the slice. Even though for very small LAT angular ranges, the difference in the greyscale values within the contour of the shape does not appear to be strikingly different from the adjoining regions, the disparity in the standard deviation is significant enough to provide a clear indication of the void's existence. By plotting the standard deviation in greyscale values of the whole image versus the thickness (as seen in the central panels of **Figure 5.6.2**), a normalized intensity profile for the X-slice.

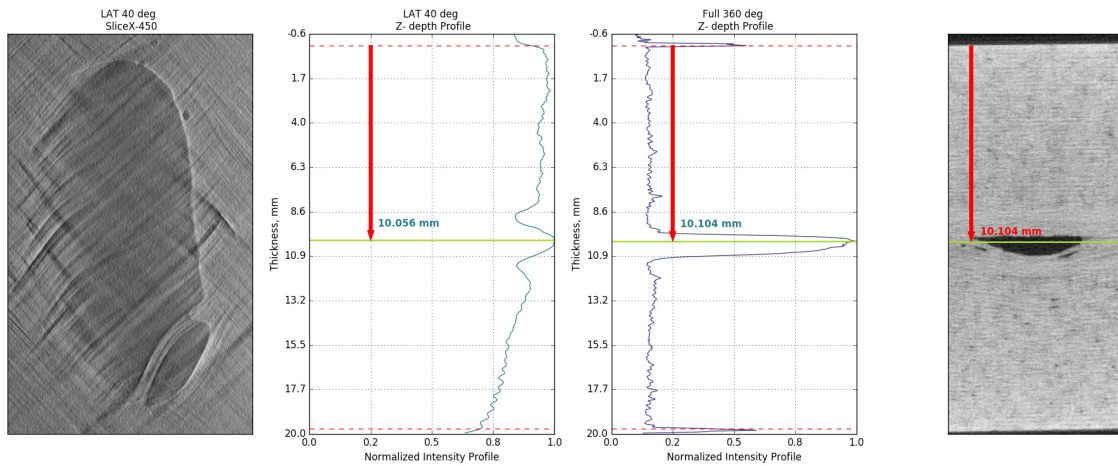


Figure 5.6.2 Demonstration of suggested method for measurement of the void in-depth location in LAT 40° reconstructed volume. Through-the-thickness intensity profile is compared for LAT 40° and full 360° scans

The same procedure is carried out for the full 360° scans. The intensity scan plotted for the full 360° scan is used here as a reference. It should be observed that the real slice of the full CT shows top and bottom edges of the structure which show two spikes in intensity at either end of the intensity plot. The Z-depth at which the peak of the prominent spike located centrally in the plot is assumed to provide the location of the void within the thickness of the structure. The full width at half maximum (FWHM) of this spike appears to agree well with the actual depth of the void seen in the full CT.

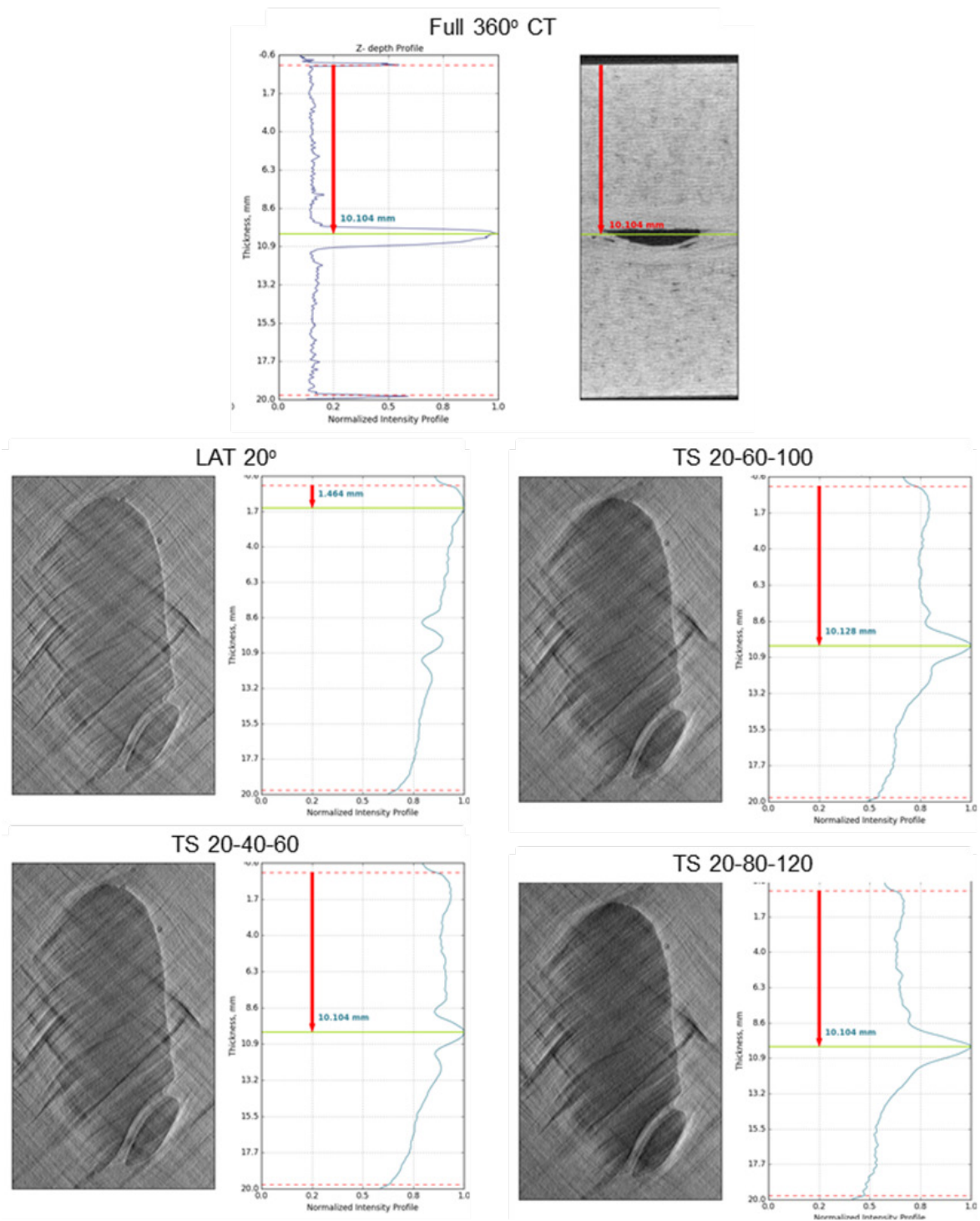


Figure 5.6.3 Comparison of depth measurements of the void for LAT 20° and different angular combinations of TS 20°

Figure 5.6.3 illustrates the comparison of depth measurements of the void for LAT 20° and different angular combinations of TS 20° using the proposed method of standard variation of the contrast in the sequence of in-plane slices. It can be observed, that the peak of intensity in all four images is in a good agreement with the reference value, obtained from the full CT. **Figure 5.6.4** shows a representation summarizing the void depth measurements made corresponding to the TS angle ranges. While thickness of the void was not measurable for LAT 20°, the results for the three TS ranges achieved through the proposed technique is in good agreement with the true value determined from the full 360° CT.

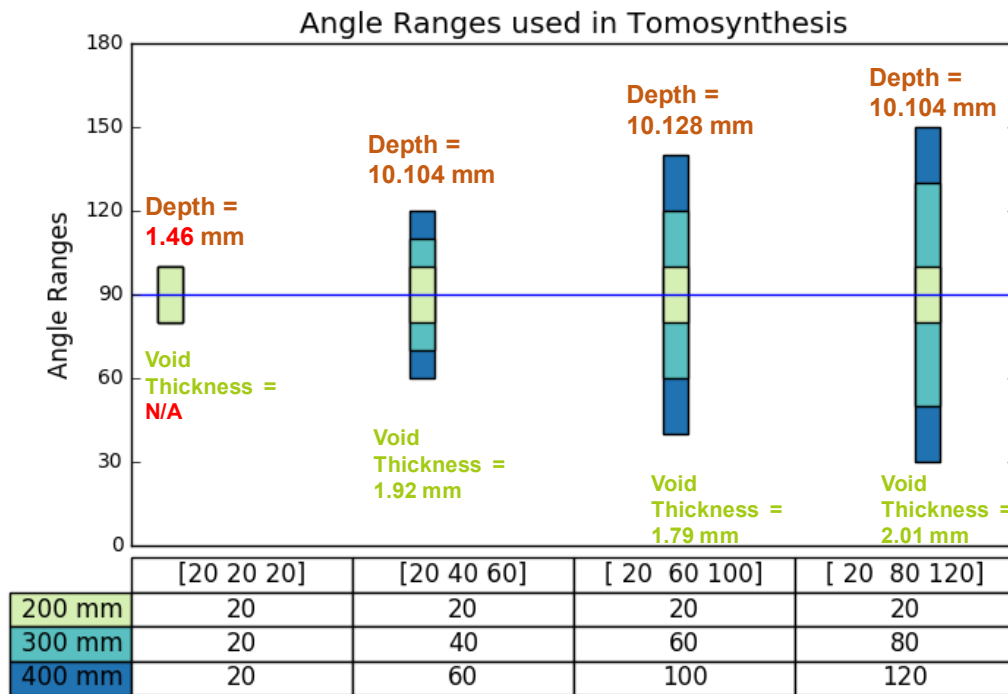


Figure 5.6.4 Measurements of the void for LAT 20° and different angular combinations of TS 20°

CHAPTER 6

CONCLUSIONS

6. Conclusions

A novel method of non-destructive inspection was proposed to address the problem of inspection of large aerospace composite structures to accurately and objectively determine defects and structural damage. Specifically, in one of the first studies of its kind, tomosynthesis (TS) was used in this work to study damage and defects in composite structures. Given the challenges in real-world problems, often studies have relied on using phantoms without adequate validation in real specimen. The work in this thesis, on the other hand, addressed real specimens involving a tremendous amount of computational effort including extremely interesting algorithms and their practical implementation. The main thrust of this work was to develop robust procedures for scan acquisition along with algorithms to reproducibly reconstruct scanned 3D image volume. The pursuit was to explore whether computed tomography-like objectivity could be achieved when detecting flaws using the newly developed enhanced LAT based scan acquisition technique. The studies were carried out on two representative composite samples containing practically significant defects namely delaminations, voids, porosity, matrix cracks, and in-plane waviness.

A few significant conclusions from this work are briefly summarized below:

- This work assesses the feasibility of TS toward composite defect analysis. Based on initial results, TS was demonstrated to be a viable technique that could provide defect information with a degree of reliability beyond that of LAT, and

significantly greater information as compared to the widely relied upon technique of 2D radiography.

- Along with the acquisition protocol, software support was developed in the form of a robust algorithm capable of working with limited projection dataset and high performance implementation of most popular image reconstruction methods, such as analytical 3D filtered backprojection (FDK) and iterative stochastic algorithms (PWLS, LSQR).
- Notably, the developed scanning protocol was implemented using a stationary cone-beam CT system. This developed technique expanded the capability of the existing industrial CT system facilitating the scan acquisition features that were previously only achievable by means of source rotation in medical systems.
- Significant improvement over limited angle tomography (LAT) was obtained using the developed TS method. Particularly, the ability to combine high resolution scan data with wider angular range datasets at different geometric magnification allowed the TS technique to achieve significantly improved defect detection capabilities.
- In this work, the hardware and software implementation was performed on realistic structures and not on simulated phantoms, keeping in mind the intended real-world application of the developed technique, i.e. inspection of composites for aerospace applications.
- In some cases, particularly flat defects in high aspect ratio objects (like delaminations in impact plate), the TS did not demonstrate significant improvement over the LAT scan.

- Several image artifacts pertinent to LAT were observed and studied over different angular ranges in order to determine the range of detectability. In some instances, image artifacts could serve to mislead an inexperienced operator by creating an illusion regarding the presence of a defect that is not present in the real structure.
- In some instances, the artifacts could in fact serve as aids in the measurement and determination of location of the defect. It was proposed that the specific kite-shaped regions occurring in each LAT scan (as a consequence of the intersection of the lines tangential to the singularities, corresponding to the acquisition angle range of the scan) could provide not only an indication of defect presence, but also approximate estimates of defect dimensions.
- A post-processing method was suggested based on an in-plane slice analysis technique by utilizing the variance in standard deviation of greyscale values achieved in the region of the void. The method was sensitive enough to decipher the variation in contrast between the void and surrounding material and predict 3D location of the void as well as its depth. The results achieved by the proposed method were in good agreement with the measurements from the full 360° scan used as a reference. In addition to the qualitative improvements to the scan resolution and depth perception produced by TS, the ability to quantify and reliably locate the location of defects makes the developed tool a potentially powerful tool for future industrial application.

7. References

1. Seon, G.; Makeev, A.; Nikishkov, Y.; Lee, E. Effects of Defects on Interlaminar Tensile Fatigue Behavior of Carbon/Epoxy Composites. *Composites Science and Technology* **2013**, *89*, 194-201.
2. Seon, G.; Nikishkov, Y.; Makeev, A. In *Structures Perspective for Strength and Fatigue Prognosis in Composites*, Proceedings of the American Helicopter Society 70th Annual Forum, **2014**.
3. Makeev, A.; Nikishkov, Y. "Fatigue Life Assessment for Composite Structure," ICAF 2011 Structural Integrity: Influence of Efficiency and Green Imperative, Komorowski, J, Ed. *Springer, New York, NY* **2011**.
4. Makeev, A.; Nikishkov, Y.; Seon, G.; Armanios, E. Effects of Defects on Interlaminar Performance of Composites. *Proceedings of the 39th European Rotorcraft Forum, Moscow, Russia* **2013**.
5. Lambert, J.; Chambers, A. R.; Sinclair, I.; Spearing, S. M. 3D Damage Characterisation and the Role of Voids in the Fatigue of Wind Turbine Blade Materials. *Composites Science and Technology* **2012**, *72*, 337-343.
6. Makeev, A.; Nikishkov, Y. Fatigue Life Assessment for Composite Structure. *ICAF 2011 Structural Integrity: Influence of Efficiency and Green Imperatives* **2011**, 119-134.
7. Nikishkov, Y.; Bostaph, E.; Makeev, A. Nondestructive Inspection of Composite Structures Based on Limited Angle X-Ray Computed Tomography. **2015**.
8. Makeev, A.; Bakis, C.; Strauch, E.; Chris, M.; Holemans, P.; Miller, G.; Spencer, D.; Patz, N. *Advanced Composite Materials Technology for Rotorcraft*. **2013**.
9. Makeev, A.; Nikishkov, Y.; Seon, G.; Armanios, E. Effects of Defects on Interlaminar Performance of Composites. **2013**.
10. Makeev, A.; Seon, G.; Nikishkov, Y.; Lee, E. Methods for Assessment of Interlaminar Tensile Strength of Composite Materials. *Journal of Composite Materials* **2014**, *49*, 783-794.

11. Seon, G.; Nikishkov, Y.; Makeev, A. Structures Perspective for Strength and Fatigue Prognosis in Composites with Manufacturing Irregularities. *Journal of the American Helicopter Society* **2015**, *60*, 1-10.
12. Nikishkov, Y.; Seon, G.; Makeev, A. Structural Analysis of Composites with Porosity Defects Based on X-Ray Computed Tomography. *Journal of Composite Materials* **2013**, *48*, 2131-2144.
13. Nikishkov, G.; Nikishkov, Y.; Makeev, A. Finite Element Mesh Generation for Composites with Ply Waviness Based on X-Ray Computed Tomography. *Advances in Engineering Software* **2013**, *58*, 35-44.
14. Nikishkov, Y.; Airoidi, L.; Makeev, A. Measurement of Voids in Composites by X-Ray Computed Tomography. *Composites Science and Technology* **2013**, *89*, 89-97.
15. Nikishkov, Y.; Makeev, A.; Cline, C.; Beasley, J.; Fay, R. Finite Element-Based Damage Tolerance Methods for Aircraft Composites. **2010**.
16. Martz, H. E.; Logan, C. M.; Schneberk, D. J.; Shull, P. J. *X-Ray Imaging: Fundamentals, Industrial Techniques and Applications*. CRC Press: **2016**.
17. Schorr, C.; Maisl, M. In *Exploitation of Geometric a Priori Knowledge for Limited Data Reconstruction in Non-Destructive Testing*, Proceedings of the Fully3D Conference, **2013**; pp 114-117.
18. Sidky, E. Y.; Kao, C.-M.; Pan, X. Accurate Image Reconstruction from Few-Views and Limited-Angle Data in Divergent-Beam CT. *Journal of X-ray Science and Technology* **2006**, *14*, 119-139.
19. Kalender, W. A. *Computed Tomography: Fundamentals, System Technology, Image Quality, Applications*. John Wiley & Sons: **2011**.
20. Hsieh, J.; Nett, B.; Yu, Z.; Sauer, K.; Thibault, J.-B.; Bouman, C. A. Recent Advances in CT Image Reconstruction. *Current Radiology Reports* **2013**, *1*, 39-51.
21. Kak, A. C.; Slaney, M. *Principles of Computerized Tomographic Imaging*. IEEE Press: **1988**.
22. Feldkamp, L. A.; Davis, L. C.; Kress, J. W. Practical Cone-Beam Algorithm. *J. Opt. Soc. Am. A* **1984**, *1*, 612-619.

23. Natterer, F. *The Mathematics of Computerized Tomography*. Society for Industrial and Applied Mathematics **1986**.
24. Gerchberg, R. W. Super-Resolution through Error Energy Reduction. *Optica Acta: International Journal of Optics* **1974**, *21*, 709-720.
25. Papoulis, A. A New Algorithm in Spectral Analysis and Band-Limited Extrapolation. *IEEE Transactions on Circuits and Systems* **1975**, *22*, 735-742.
26. Sezan, M. I.; Stark, H. Image Restoration by the Method of Convex Projections: Part 2 Applications and Numerical Results. *IEEE Trans Med Imaging* **1982**, *1*, 95-101.
27. Shepp, L. A.; Vardi, Y. Maximum Likelihood Reconstruction for Emission Tomography. *IEEE Transactions on Medical Imaging* **1982**, *1*, 113-22.
28. Quinto, E. T. Local Algorithms in Exterior Tomography. *Journal of Computational and Applied Mathematics* **2007**, *199*, 141-148.
29. Guo, Y. M.; Zeng, L. Improved Iterative Image Reconstruction Algorithm for the Exterior Problem of Computed Tomography. *Nucl Instrum Meth A* **2017**, *842*, 96-108.
30. Dong, B.; Li, J.; Shen, Z. X-Ray CT Image Reconstruction Via Wavelet Frame Based Regularization and Radon Domain Inpainting. *Journal of Scientific Computing* **2013**, *54*, 333-349.
31. Cormack, A. M. Representation of a Function by its Line Integrals, with Some Radiological Applications. *Journal of Applied Physics* **1963**, *34*, 2722-2727.
32. Helgason, S. The Radon Transform on Euclidean Spaces, Compact Two-Point Homogeneous Spaces and Grassmann Manifolds. *Acta Mathematica* **1965**, *113*, 153-180.
33. Quinto, E. T. Singular Value Decompositions and Inversion Methods for the Exterior Radon-Transform and a Spherical Transform. *Journal of Mathematical Analysis and Applications* **1983**, *95*, 437-448.
34. Quinto, E. T. Singularities of the X-Ray Transform and Limited Data Tomography in \mathbb{R}^2 and \mathbb{R}^3 . *SIAM Journal on Mathematical Analysis* **1993**, *24*, 1215-1225.
35. Quinto, E. T. Exterior and Limited-Angle Tomography in Non-Destructive Evaluation. *Inverse Problems* **1998**, *14*, 339-353.

36. Rantala, M.; Vanska, S.; Jarvenpaa, S.; Kalke, M.; Lassas, M.; Moberg, J.; Siltanen, S. Wavelet-Based Reconstruction for Limited-Angle X-Ray Tomography. *IEEE Trans Med Imaging* **2006**, *25*, 210-7.
37. Candes, E. J.; Bouman, C. A.; Romberg, J. K.; Miller, E. L. Signal Recovery from Random Projections. **2005**, *5674*, 76.
38. Jaffe, J. S. Limited Angle Reconstruction Using Stabilized Algorithms. *IEEE Transactions on Medical Imaging* **1990**, *9*, 338-344.
39. Yu, Z.; Thibault, J. B.; Bouman, C. A.; Sauer, K. D.; Hsieh, J. Fast Model-Based X-Ray Ct Reconstruction Using Spatially Nonhomogeneous ICD Optimization. *IEEE Transactions on Image Processing* **2011**, *20*, 161-75.
40. Elbakri, I. A.; Fessler, J. A. Statistical Image Reconstruction for Polyenergetic X-Ray Computed Tomography. *IEEE Transactions on Medical Imaging* **2002**, *21*, 89-99.
41. Dobbins, J. T., 3rd; McAdams, H. P. Chest Tomosynthesis: Technical Principles and Clinical Update. *European Journal of Radiology* **2009**, *72*, 244-51.
42. Sechopoulos, I. A Review of Breast Tomosynthesis. Part I. The Image Acquisition Process. *Medical physics* **2013**, *40*.
43. Skaane, P.; Bandos, A. I.; Gullien, R.; Eben, E. B.; Ekseth, U.; Haakenaasen, U.; Izadi, M.; Jebesen, I. N.; Jahr, G.; Krager, M.; Niklason, L. T.; Hofvind, S.; Gur, D. Comparison of Digital Mammography Alone and Digital Mammography Plus Tomosynthesis in a Population-Based Screening Program. *Radiology* **2013**, *267*, 47-56.
44. Rehak, M.; Haßler, U.; Hanke, R. In *Acquisition Trajectories for X-Ray Tomosynthesis Applied to Planar Samples*, 2nd International Symposium on NDT in Aerospace, **2010**; p 24.
45. Council, N. R. *Mathematics and Physics of Emerging Biomedical Imaging*. National Academies Press: **1996**.
46. Zeng, G. L. Revisit of the Ramp Filter. *IEEE transactions on nuclear science* **2015**, *62*, 131-136.
47. Paige, C. C.; Saunders, M. A. Algorithm 583: Lsqr: Sparse Linear Equations and Least Squares Problems. *ACM Transactions on Mathematical Software (TOMS)* **1982**, *8*, 195-209.

48. O'Brien, N.; Mavrogordato, M.; Boardman, R.; Sinclair, I.; Hawker, S.; Blumensath, T. Comparing Cone Beam Laminographic System Trajectories for Composite Ndt. *Case Studies in Nondestructive Testing and Evaluation* **2016**, *6*, 56-61.
49. Friel, J. Reconstructions in Limited Angle X-Ray Tomography: Characterization of Classical Reconstructions and Adapted Curvelet Sparse Regularization. PhD Thesis, Technische Universität München, **2013**.
50. Sen Sharma, K.; Jin, X.; Holzner, C.; Narayanan, S.; Liu, B.; Wang, D.; Agah, M.; Wang, L.; Yu, H.; Wang, G. Experimental Studies on Few-View Reconstruction for High-Resolution Micro-CT. *Journal of X-ray Science and Technology* **2013**, *21*, 25-42.
51. Wang, J.; Li, T.; Lu, H.; Liang, Z. Penalized Weighted Least-Squares Approach to Sinogram Noise Reduction and Image Reconstruction for Low-Dose X-Ray Computed Tomography. *IEEE Trans Med Imaging* **2006**, *25*, 1272-83.

APPENDIX A

The test image in Figure 3.3 is in the form of a 2D digital phantom, simulating three circular objects of different densities with randomly spread small voids. The idea of the study was to observe how the number of views affects the FBP tomography slice of the volume. It is well known that when the singularities are located at a large distance away from the axis of rotation, they could be missed due to angular undersampling. The small number of views demonstrates a lot of false void-like locations along with the true ones. The latter are marked by the yellow circles in the Figure 3.3. The dark streak lines intersections appear as dark areas and give an illusion of voids presence. As the number of views increases, the ambiguity resolves. It is worth noting, that the 80 views slice, shown in the Figure 3.3 detects all four voids with a good accordance with the original image. Although the image is severely corrupted by streaking artifacts it provides the essential information about the mere presence of simulated defects. This was achieved by collecting less than a half of commonly required number of angular views. With time constraint being a usual factor in industrial environment, knowledge about the anticipated artifacts and detectability threshold can facilitate a less lengthy scan by acquiring smaller number of projections, equally distributed around the object's rotation range.

APPENDIX B

High-Performance Implementation

Most of the current literature on the iterative reconstruction demonstrates solution methods on relatively small problems, often two-dimensional, and less than one million variables in size. In three dimensions one million variables translates to a cube that has 100 points in each dimension; a resolution that is not adequate for resolving defects in real structures. Modern industrial X-ray CT systems based on Feldkamp algorithm routinely reconstruct 10 billion point volumes within an hour time. While stochastic reconstruction methods clearly require more computation, recent advances in vector processing hardware led to high-performance implementations of stochastic algorithms capable of handling realistic problems.

Projection and back-projection are by far the most time-consuming operations in the reconstruction algorithms considered. Our implementation uses two-fold parallelization of these operations: first, calculations are independent for each projection angle so that they can be split between main CPU processing cores; second, multiple CPU cores communicate with GPGPU vector processor to schedule projection / back-projection for each volume point. Modern GPGPU processors contain up to 3000 vector processing units that are able to execute identical code operating on different data in parallel. Projection and back-projection code takes advantage from GPGPU vector processing by implementing identical complex line integral calculation required for each volume point.

Note that this implementation also requires little main CPU memory due to efficient computation by vector units.

In this work we used single 2.2 GHz Intel Xeon E5-2660v2 processor and two high-end consumer graphics cards by NVIDIA: GeForce GTX TITAN Black (2880 CUDA cores) and GeForce GTX 980 (2048 CUDA cores). Due to large data transfers between the main CPU and graphics cards, using two CPU cores per graphics card was found to provide optimal performance.

APPENDIX C

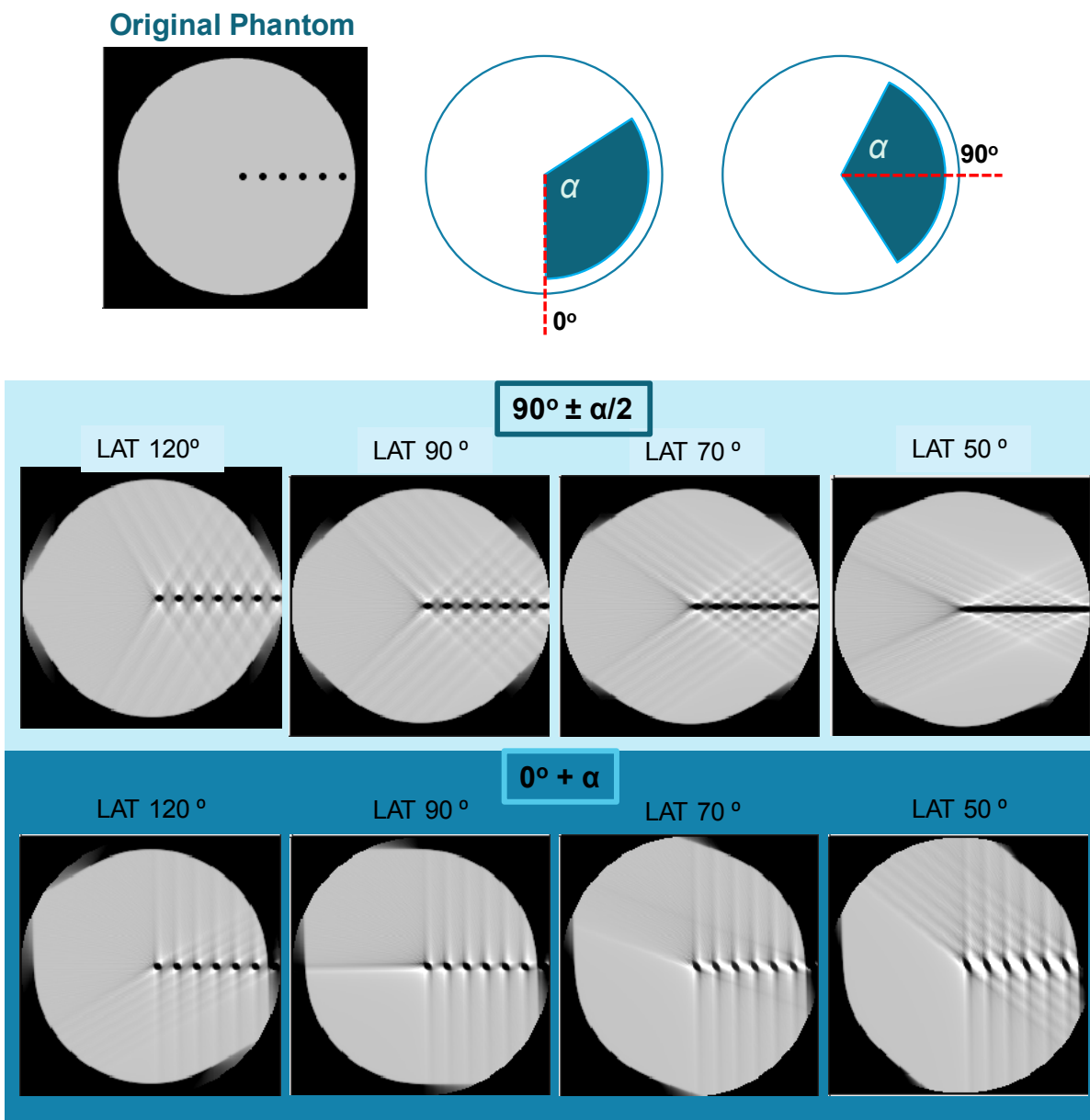


Figure C1 Shape deterioration of a sequence of voids with respect to LAT angular range.

The original digital image shown in **Figure C1** was designed to simulate voids in a circular object at a distance from the center of rotation axis. It was therefore interesting to observe the effect of limited angular coverage on the shape distortion of the sequence of voids when positioned close to each other. The reconstructions were performed with filtered backprojection algorithm for a 2D case and the fan-beam. The circular shape of the original object was preserved by constraining mask of the radius equal to the half size of the image. Two study cases were considered with different starting angle: 0° and 90° minus half the angular range.

In both groups of LAT scans the characteristic streaking lines, tangent to the singularities were present. As the angular range decreases in the first row of images, the space between the voids fills in with rhombus shaped artifacts, which eventually turn into misleading illusion of the continuous line.